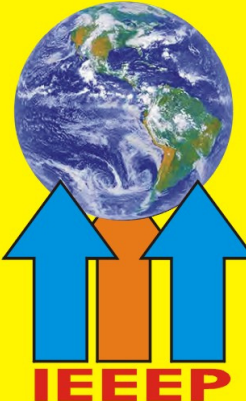


# New Horizons



Electricity Generation with Speed Breaker and Application of Smart Grid.

P.9

Simulations of Interleaving Two Switched-Inductor Hybrid DC Boost Converters For Fuel Cell Applications

P.20

Performance Analysis of 3-D DWT, 3-D DFT, 3-D DCT, 3-D DHT for Medical Image Compression

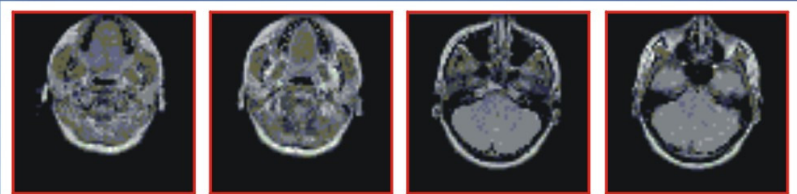
P.29

System Design for Prevention of Electricity Theft

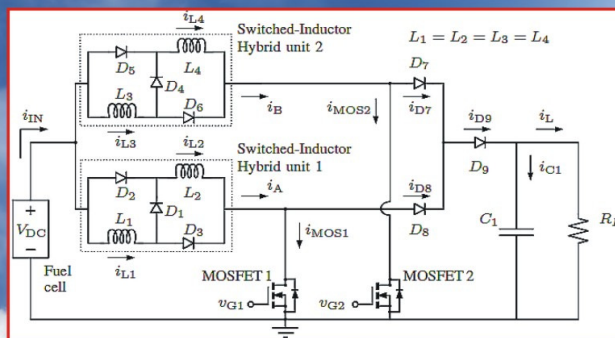
P.47

Vol:# 79-80 Upto Dec. 2013

ISSN 2226-3659



P.32



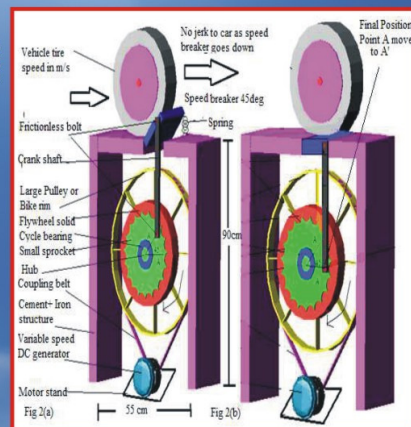
P.20



P.49



P.10



IEEEP

Journal of The Institution of  
Electrical and Electronics Engineers Pakistan

## "New Horizons"

### Journal of The Institution of Electrical & Electronics Engineers Pakistan

VOL # 79-80 Upto Dec 2013

#### Board of Publications-2011-14

*Chairman*

**Engr. Prof. Dr. T.A. Shami**

*Dean*

*Faculty of Engineering  
University of Central Punjab, Lahore.  
Email:drshami@ucp.edu.pk*

*Secretary*

**Engr. Prof. Dr. Suhail Aftab Qureshi**  
*UET Lahore.  
Email:tiger\_suhail@hotmail.com*

**Engr. Prof. Dr. Rana Abdul Jabbar**  
*CEO FESCO  
Email:ranaabbarkhan@yahoo.com*

**Engr. Dr. Khawaja Rifat Hassan**  
*Dy. Director Wapda  
Email:riffathassan1@hotmail.com*

**Engr. Prof. Dr. Muhammad Jahangir**  
*LUMS University Y-Block, DHA, Lahore  
Head of the Computer Engineering Department  
Email:jkram@lums.edu.pk*

*Chief Editor:*

**Engr. Prof. Dr. Suhail Aftab Qureshi**  
*UET Lahore  
Email:tiger\_suhail@hotmail.com*

*President*

**Engr. Tahir Basharat Cheema**

*Vice President*

**Engr. Muhammad Azeem**

*Vice President (South)*

**Engr. S. S. A. Jafri**

*Hony. Secretary General*

**Engr. Prof. Dr. Suhail Aftab Qureshi**

*Hony. Treasurer*

**Engr. Kamran Masood Khan**

*Hony. Joint Secretary*

**Engr. Syed Saleem Akhtar**

4-Lawrence Road, Lahore. Ph:(042) 36305289  
Fax: (042) 36360287 Email:info@ieeep.org.pk  
Website:www.ieeep.org.pk

**Disseminate Technical  
Knowledge**



**Conserve Electricity**

## CONTENTS

Page  
No

### Editorial

2

### 1 The Three Pillars of a Viable Power Sector!

3

By Engr. Tahir Basharat Cheema

President (Elect)

Institution of Electrical & Electronics Engineers Pakistan (IEEEP)

### 2 Queuing Theoretic Analysis of a WSN based Earthquake Monitoring System\*

5

By Engr. Sanam Memon\*, Wanod Kumar\*  
and Muhammad Asim Ali\*\*

\*Dept., of Elect. Engg, MUET Jamshoroo, Pakistan.

\*\* Dept., of Elect. Engg. Sukkur IBA, Pakistan.

### 3 Electricity Generation with Speed Breaker and Application of Smart Grid.

9

By Engr. Shakeel Ahmed

University of Lahore, Pakistan

Engr. Prof. Dr. Suhail Aftab Qureshi  
UET, Lahore Pakistan.

### 4 Hybrid Renewable Energy Source Implementation in Pakistan

16

Engr. Hamid Ali, Dr. Naeem Arbab, Engr. Qazi Waqar Ali  
University of Engineering & Technology, Peshawar Pakistan

### 5 Simulations of Interleaving Two Switched-Inductor Hybrid DC Boost Converters For Fuel Cell Applications

20

Umar T. Shami\* and Tabrez A. Shamji\*\*

\*University of Engineering & Technology, Lahore Pakistan.

\*\* University of Central Punjab, Lahore Pakistan.

### 6 Cellular Communication Using Single band Microstrip Patch Antenna Model

25

Engr. Omer Iqbal, Abid Hussain Chohan, Engr. Farhan Fareed  
Dept.of Electrical & Electronics NFC Institute of Engg & Techno:  
Training Multan, Pakistan.

### 7 Performance Analysis of 3-D DWT, 3-D DFT, 3-D DCT, 3-D DHT for Medical Image Compression

29

Zain ul Abidin, Depp.t.of Electrical Engg. UET Texila

Gulstan Raja, Dept.of Electrical Engg.UET Texila

Muhammad Haroon Yousaf, Dept.of Computer UET Texila

### 8 A Mathematical Interpretation and Simulations for the 2-D Prime/OOC coding in Long Reach OCDM Access Network

39

Abdul Latif, Deptt.of Telecom Engineering Mehran UET Jamshoro

Khuda Bux Amur, Deptt. Math Quaid-e-Azam UEST Nawabshah

Dr. Muhammad Imran Malik, Deptt.of Compuer Engg: College  
of Engineering and Technology, Bahauddin Zakariya University Multan

### 9 System Design for Prevention of Electricity Theft

44

Dr. Khawaja Riffat Hassan, Saleem Rashid (NTDCL)  
Mazhar Raza, (PAEC)

### 10 A PWM-Based Technique to Measure Phase Angle Between AC Voltage and Current

53

Umar T. Shami\* and Tabrez A. Shamji\*\*

\* University of Engineering and Technology, Lahore, Pakitan

\*\* University of Central Punjab, Lahore Pakisan

## ***Editorial***

*Once again, here is another volume of this journal that brings to you some latest research and development papers in various fields of technology. Presently, as we all know, our country is facing an ongoing power crisis. Engr. Tahir Basharat Cheema has contributed an informative article discussing the basic pillars of a Viable Power Sector and has suggested measures for strengthening the generation, fuel and customer mix for a healthy power system.*

*Engr. Prof. Dr. Suhail Qureshi has contributed an exciting paper that introduces an amazing creative approach for generating electricity from speed breakers and its connection to Smart Grid. An enormous amount of energy can be converted to thousands of electrical units by installing an electromechanical system under speed breakers on roads and the energy generated can share load of national grid. This would help cover up a little bit of energy shortage and also reduce the local electricity bills.*

*Another excellent paper explains the great idea of solar-wind hybrid power generation for charging UPS batteries in homes. This again would reduce the electric bills. Another paper describes an effective system developed for the prevention of Electricity Theft caused by direct rigging. All these measures would help tackle the ongoing power crises.*

*This volume also includes a research analysis of compression techniques of medical images for diagnoses of different diseases. This would help dealing with the huge storage needs and fast transmission requirements. Another paper explains a modern Earthquake Monitoring System.*

*Thus, a lot of latest research papers in various fields of Electrical and Electronics Engineering have been included in his volume. We are thankful to the Higher Education Commission who has awarded category-Y to our research journal, "New Horizons". Hearty CONGRATULATIONS to all our members on this up-gradation of our journal. I am happy to see that our team is working hard to improve this journal to become number-One latest research information source for the engineers in the country.*

*The Editor*

## The Three Pillars of a Viable Power Sector!

By *Engr Tahir Basharat Cheema*

President (Elect)

Institution of Electrical & Electronics Engineers Pakistan (IEEEP)

The power crises has catapulted the power sector to the forefront. Every body is talking about it's working and also advising the government as to what needs to be done. Most of the arm-chair experts talk about some missing power policy and that necessary resolve is not evident. Some of the more brave advice that alternate energy should be tapped with wind and solar swinging the fates in our favour. Though freeing ourselves from oil and gas is an important requirement, the various pre-requisites to induction of alternate energy and the needed financial depth is normally swept under the carpet. That the base load requirements and those pertaining to peaking demands are two different realms needing different solutions is also conveniently forgotten. There is thus a need to dilate upon the subject and explain the various facets of a viable power sector. **And in order to do so, we will concentrate on the generation, the fuel and the customer mix alone – incidentally, the basic parameters of any viable power sector.**

Going back to 1976, when Tarbela was commissioned and which added a hefty 3600 MW to the national tally, we see that the then hydel-thermal ration drastically changed and improved in favour of hydel to 80:20. The record tells us that the 20% thermal generation too was basically fueled by gas and thus was not burdening the customers much. Unfortunately, this trend which stabilized at 70:30 in favour of hydro-generation has since changed for the worse and the generation mix now stands at 30% only for the hydel component with 46% of the rest using RFO as the fuel against just 5.6% world average. The small usage of gas, coal and nuclear fuel does not seem to list the balance away from expensive oil.

As presently, the hydel tariff being charged by WAPDA is Rs.1.18 per unit while the same for RFO fired thermal units can be above Rs.15.00 on the average, one can imagine the negative effect the changed ratio would have on the price of electricity. However, one thing is for sure – the generation mix has to necessarily change in favour of hydel plants. On the other hand, as hydel generation depends upon the completion of long gestation projects, which too are subject to many a wrangling in the Pakistani context, we will have to come-up with some other solution in the short run and concurrently work on hydel projects in the long run. The answer lies in the improvement of the fuel mix for the thermal plants. This would be a change from the present pre-dominantly RFO usage to gas in the first instance (for about 2-3 years) and eventually the needed transfer to coal, which can be indigenously mined or of the imported variety. According to financial experts, changeover from RFO to gas for about 3000 MW of thermal generation (at Jamshoro,

Muzafargarh and KAPCO plants) would reduce the cost of generation by at least Rs.6.00 per unit with an accumulative positive effect on the yearly expenditures of PEPCO by upto Rs.75 billion. The needed volume of gas can be made available as part of a national policy. And as this is only destined to be specially made available for 2-3 years, concurrently efforts have to be made to convert all the thermal plants, both in the public and the private sectors, to coal. This can be done through PSDP funding, the public private partnership (PPP) mode or simply through garnering of the supplier's or the buyer's credit for conversion equipment (including EPC contracts). All of these ways of conversion are doable and can be taken up through a consensus of the experts.

The third of the pillars pertains to the issue of the lopsided customer mix, which the utilities have to face at the moment, having a burden of Rs.50 billion or so. As it is simply detrimental to the financial stability of the utilities, the issue is of equal importance in comparison to the negative generation and fuel mix. It is seen that at present out of the total 19.662 million customers of PEPCO, a hefty 9.3 million customers can in a way, be categorized as the life line customers. These customers use upto a maximum of 100 units per month and are being charged at very low rates in comparison to rest of the customer base.

The present tariff for the 1–50 units usage category is just Rs.1.87 per unit, while the 1–100 units usage would allow the DISCOs / KESC to bill the customers at the rate of Rs.4.36 per unit. Imagine the level of these rates in comparison to the calculated cost of service which at present is a little above Rs.10.00 per unit on the average. In other words, cross-tariff and general subsidies pay for the sustenance of the utilities and to do away with the burden of this group of customers and thus it is extremely onerous for the utilities. As the subsidies do not fully cover the gap, the loss has to be borne by the distribution companies or have to be passed on the other categories of customers in shape of enhanced tariffs. Unfortunately, this category of customers is on the increase due to heightened rural electrification and unplanned urbanization through what is known as the Kachi Abadies.

The question arises as to why should the socio-political obligations of the governments be made to burden the utilities. As such, the requirement is to bill all the customers at a uniform rate – at least for the domestic, the commercial, the industrial and the agriculture categories. Consequently, the present load suppression model of tariff formulation has to be scrapped and instead the more you use, the less you pay model has to be accepted as the rule.

On the other hand, because the less endowed customer too has to be taken care of, the group can be supported through targeted subsidies. Power stamps similar to food stamps of the yesteryears and those in vogue in the developed world and specifically the USA can also be issued. In other words, the utilities would issue regular bills to all customers including the life line category and at the time of payment, the power stamps can be redeemed at the banks. The huge data bank collected for the BISP through the poverty survey can easily be used to assist the life line customers in getting the subsidies. In this manner, both the customers and the utilities can benefit.

Through the above measures, all the three basic pillars of a healthy power system / sector can be strengthened – otherwise, we will not be able to tackle the ongoing power crises and nor would the sector be able to deliver. Infect, spoiling of the generation, the fuel and the customer mix is the reason for high power tariffs in the country. Capacity shortages is another story needing separate space to dilate upon.

\*\*\*\*\*

## Quotations

- The secret to a long life is to stay busy, get plenty of exercise, and don't drink too much. Then again don't drink too little  
Hermann Smith-Johannson, at age 103
- Anyone stops learning is old, whether at trwnety or eighty. Anyone who keeps learning stays young.  
Henry Ford
- The first forty years of life give us the text, the next thirty supply the commentary.  
Anthony Schopenhauer
- When good men die, their goodness does not perish.  
Euripides
- I am ready to meet my Maker. Whether my Maker is prepared for the ordeal of meeting me is another matter.  
Winston Churchill
- If you are afraid to die, you will not be able to live.  
James Baldwin
- Remember that the most beautiful things in the world are most useless; peacocks and lilies, for instance.  
John Ruskin
- Whatever's begun in anger ends in shame.  
Benjamin Franklin
- Constant attention by a good nurse may be just as important as a major operation by surgeon.  
Dag Hammarskjold
- Look to your health, and if you have it, praise God, and value it next to a good conscience; for health is the second blessing that we mortals are capable of; a blessing that money cannot buy.  
Izzak Walton
- One must eat to live, not live to eat.  
Molieere
- People who drink to drwon their sorrow should be told that sorrow knows how to swim.  
Ann Landers
- Character is the result of two things – mental attitude and the way we spend out time.  
Elbert Hubbard
- What's the difference between a stumbling block and stepping stone?  
The way you approach it.

**Sanam Memon\***, **Wanod Kumar\***,  
**and Muhammad Asim Ali\*\***

\*Department of Electronic Engineering, MUET Jamshoro, Pakistan

\*\*Department of Electrical Engineering, Sukkur IBA, Pakistan

### **Abstract:**

*Earthquake monitoring and detection has been in great focus for many years. A possible solution of this problem is the deployment of an efficient system that can generate the warning for the earthquake as early as possible. This kind of deployment not only helps to save human lives but also provides support in exploring many hidden facts about great disaster. In this paper, performance analysis of Wireless Sensor Network (WSN) based earthquake monitoring system is carried out using queuing theory. The WSN nodes transmit their data to a centralized node which further sends this data to main station using a wireless/wired backhaul link. This scenario is modeled using two queues; M/M/1 queue and M/D/1 queue. The performance of the system is evaluated and compared in terms of mean system delay and utilization for both queuing models. The results reveal that the system delay decreases with increase in the data rate of the communication link (server).*

**Keywords:** delay, earthquake, queuing, WSN.

### **I. Introduction**

Earthquake is a type of natural disaster. This disaster occurs due to the sudden release of stored energy in the Earth's crust that creates seismic waves [1]. On 26 December 2004, an earthquake of magnitude 9.0 caused huge loss of human lives in Indonesia and its neighboring countries. That great loss motivated scientists and researchers to discover new mechanisms for detecting and monitoring the earthquake so that people can get warning in time, and thus any serious loss can be avoided. The WSN based monitoring system is one of these paradigms considered.

A node in wireless sensor network is capable of sensing, processing, and communicating with other nodes in the range or a centralized entity (node). This helps to observe and react according to the condition in a particular environment. WSNs are application specific; hence design considerations are different for each application [2]. A node in WSN consists of a transmitter, receiver or a transceiver for detecting, measuring and transferring the data to the central node/server. Such a network called Quake-Catcher Network (QCN) is built upon the Berkeley Open Infrastructure for Network Computing (BOINC) software for volunteer computing [3]. The QCN is a large network of low-cost sensors connected to volunteer computers, in a specific region to monitor seismic events.

Recently, an increased interest has been observed to analyze the network performance using analytical or simulation tools before the actual deployment. In this regard the Queuing theory offers a promising analytical solution to evaluate the performance of such networks in terms of quality of service (QoS) parameters. Therefore, in this work,

a detailed analysis based on queuing theory for modeling WSN is carried out for analyzing the mean system delay and utilization. Single node of WSN acts as a complete QCN node and combination of number of nodes represents a network of nodes (i.e. WSN). These nodes transmit their packets to a centralized node which further communicate these packets to main office using wireless/wired backhaul link.

Following the introduction, the paper is organized as follows: Section II describes Related Work. Section III presents Studied Scenario. In section IV, mathematical model for the proposed design is discussed. The performance analysis is carried out in section V. Paper concludes in section VI.

### **II. Related Work**

In [1], a novel early warning system for earthquake based on WSN is proposed. This WSN consists of several thousands of nodes, each node consists of a single antenna and these nodes cooperate with each other to form a multiple antenna WSN known as Virtual MIMO WSN. Researchers in [2] believe that animals act abnormally before and after earthquake and their behavior is helpful in the prediction of an earthquake. On that basis, they have proposed an overall network architecture in which middleware software infrastructure, WSN, end user system, different detectors, mobile base stations and animals play major role. In [3], authors highlight the importance of location and density of low cost sensors used in QCN in order to detect and monitor the seismic activities efficiently and accurately. Researchers in [4] have replaced traditional seismic networks with a new, more efficient and inexpensive alternate named as QCN using MEMS accelerometer. In [5] authors have developed an accelerometer which provides high sensitivity and a wide measureable range, while in a traditional accelerometer, there is a tradeoff between the measureable range and sensitivity.

Authors have designed an alarm system in [6] to determine the magnitude of the longitudinal wave with the help of the accelerometer and compared it with the predetermined threshold. If that magnitude is found to exceed the threshold, then the notification for earthquake in the form of alarm is sent to the concerned alarm devices of the network. Authors in [7] have taken initiative towards design of a new wireless sensor node that is not having only minimum physical size and less power consumption but also able to perform simple processing on the acquired data in order to reduce the amount of data that is to be stored at the node. It is based on an ultra-low power System on Chip (SOC) microcontroller with a temperature sensor and a 3-axis accelerometer.

Traditionally queuing theory has been used to analyze the performance of communication networks. However, to the best of our knowledge, little work has been carried out in regards to WSN for earthquake monitoring using this theory. In [8] WSN is modeled using the open queuing network theory for path planning. The issue of path planning is solved by calculating the path delay to find out the optimal path for efficient data transmission in WSN. Authors in [9] have derived the expression for the distribution and first two moments for both steady state and transient conditions for different random variables and then investigated the output process of M/D/1 queuing system.

The issue of WSN scaling is highlighted in [10]. Authors found that network dynamics mainly depends on network operations rather than environmental changes but environment is able to put an unpredictable effect on sensor network. They also found that network indicators can't identify the problem if small portion of nodes bottlenecks the whole network.

It has been suggested in [11] that by using variable data rate with automatic rate selection not only network latency but also average power consumption can be reduced and is essential for improving scalability and minimizing network overhead. This technique when compared with other techniques provided energy consumption with 40% saving.

### III. Studied Scenario

The USB sensor/accelerometer and computing capability constitute a single WSN node. The ground motion is detected with the help of MEMS accelerometer present in WSN node. The information (seismic data) is collected by every node individually and transmitted to the centralized node in terms of data packets as shown in Figure 1. The data transmission (in form of packets) from  $M$  sensor nodes and reception at centralized node is modeled as M/M/1 and M/D/1 queues [12]. Here single server is considered which is wireless/wired backhaul link to the main station. Without

loss of generality, in this work,  $M$  WSN nodes are assumed to have the same mean packet arrival rate  $\lambda_n$  which further collectively sums to the  $M\lambda_n$ . Packet arrival rate of each node follows a Poisson distribution with mean  $\lambda_n$ . The arrived packets are further communicated to the main station by central node using a service rate. Our aim in this paper is to analyze the performance of WSN based earthquake monitoring using queuing theory in terms of average system delay and utilization.

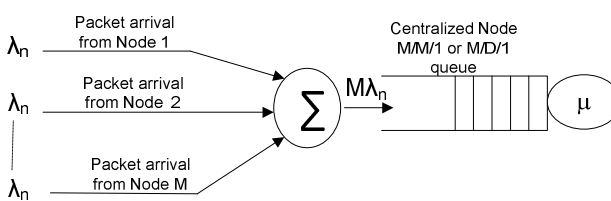


**Figure 1:** Queuing Model for the Proposed System

### IV. Analytical Modeling

In this section we present the analytical modeling of M/M/1 and M/D/1 queue.

#### a) M/M/1 Queuing Model:

In scenario considered, each node transmits the data packet with mean arrival rate  $\lambda_n$ , hence the combined arrival process becomes Poisson process with mean arrival rate  $\lambda = M\lambda_n$ . These data packets are sent to a centralized node for further communication to the main station using backhaul connection. This scenario is modeled as M/M/1 queue [12]. Central node further forwards the data packets with service rate  $\mu$  using the First-In First-Out (FIFO) priority. The complete representation of this WSN based system for earthquake monitoring using M/M/1 is shown in figure 1. Figure 2 shows the state transition diagram of M/M/1 queue represented as a birth-death model.

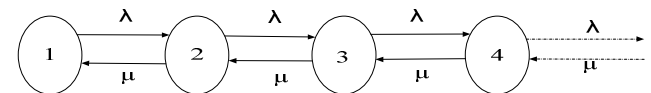


**Figure 2:** The state transition diagram for M/M/1 queue

The equilibrium probability for M/M/1 queue is

$$p_n = \rho^n (1 - \rho) \quad (1)$$

where  $\rho = \lambda / \mu$  is the traffic intensity,  $n$  is number of packets [12]. To ensure the stability of the system,  $\rho$  should be less than 1. It means that arrival rate is smaller than service rate; otherwise the number of packets will keep increasing with passage of time.

The mean number of packets in the system is

$$L = \sum_{n=0}^{\infty} n p_n \quad (2)$$

The average delay experienced by each data packet is the combination of waiting time in the queue and service time and can be calculated using Little's theorem [12] as

$$W = \frac{L}{\lambda} \quad (3)$$

The utilization of the system is given by

$$U = \frac{\lambda}{\mu} = \rho \quad (4)$$

#### a) M/D/1 Queuing Model:

In M/D/1 queuing model, the arrival process is Poisson distributed and service time of each packet is constant [9]. Service time is fixed because both the packet length and the data rate of link are deterministic.

The mean number of packets in the system

$$L = \rho + \frac{\rho^2}{2(1 - \rho)} \quad (5)$$

The mean system delay in this model is

$$W = \frac{2 - \rho}{2\mu(1 - \rho)} \quad (6)$$

## V. Performance Evaluation

All  $M$  WSN nodes send their data to a centralized node as shown in figure 1. The communication through this central node is modeled as both M/M/1 and M/D/1 queue. The real packet length (i.e. **100 Bytes**) used in [11] is considered here. The communication link used for transferring data from  $M$  WSN nodes to the main station through centralized node has data rate of 1Mbps [10]. Hence, the **1250 packets**

mean service rate turns out to be  $\frac{1250}{sec}$ . In this work, we evaluate the performance of the WSN for earthquake monitoring using average packet delay and utilization as QoS metrics for both M/M/1 and M/D/1 queuing models.

Figure 3 shows the impact of traffic intensity on the system delay. This analysis of mean system delay is necessary in order to select the values of  $\rho$  (traffic intensity), in such a way that the delay can be as minimum as possible and the warning for earthquake may be generated and processed in time. The results reveal that the average delay of the data packets increases with the increase in  $\rho$  values. In case of M/M/1 queue, the system delay is very low for  $\rho = 0.1$ . The delay starts to increase rapidly when  $\rho$  exceeds 0.2. This is because the arrival of data packets from  $M$  WSN nodes increases and a single server has fixed service capability. The maximum mean delay caused by the system to the data packets generated by source nodes is **4 ms**. In case of M/D/1 queue, the service time (provided by single server) is fixed for each WSN packet and the mean system delay is reduced compared to the M/M/1 queuing model. This is due to the uniformity of the service rate.

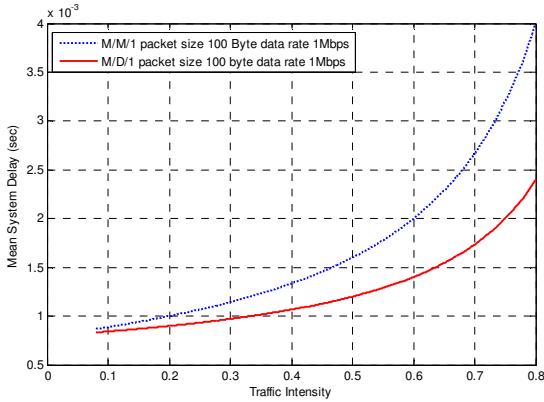


**Figure 3:** System Delay as a function of Traffic Intensity with 1 Mbps link

Now, we consider data rate of communication link to be **2 Mbps** with same packet size and data generation rate. Hence, the service rate of the system doubles and value of

the traffic intensity becomes half compared to the parameters considered for results shown in Figure 3. With this communication link, each packet is served faster. In this system setup, as shown in Figure 4, the mean delay for M/M/1 queue at  $\rho = 0.04$  is less than **0.7 ms** compared to previous setup (with link rate of 1 Mbps) where it was about **1.3ms**. Moreover, for M/D/1 queue, the mean delay is lower compared to M/M/1 queue.

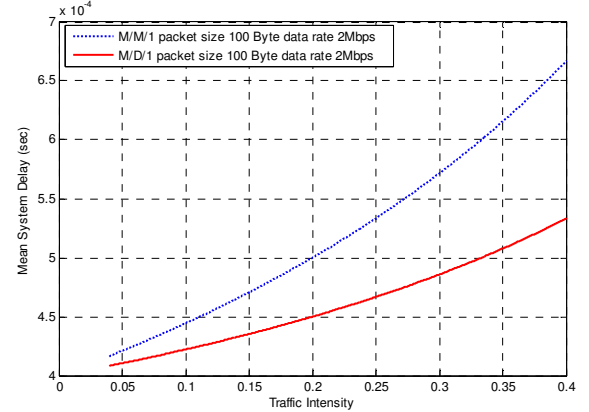


**Figure 4:** System Delay as a function of Traffic Intensity with 2 Mbps link

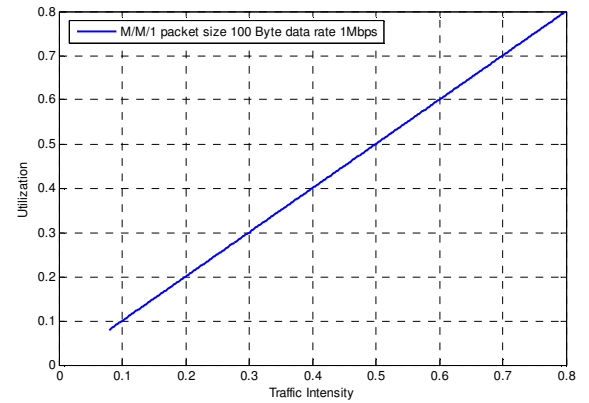


**Figure 5:** Utilization as a function of Traffic Intensity

System utilization is directly proportional to the traffic intensity values for both queuing models. The utilization is the measure of how much server is busy and is equal to  $\rho$ . It is due to the fact that  $\rho$  depends on the arrival of packets (with the mean service rate of the system is kept constant).

As arrival rate of data packets increases,  $\rho$  increases and this in turn causes utilization to increase. This effect always gives a linear curve when utilization is plotted against traffic intensity. It is shown for M/M/1 queue in Figure 5. M/D/1 queue has a linear trend as well.

## IV. Conclusion

In this paper, performance analysis of WSN based earthquake monitoring system has been carried out. For this

purpose, we have considered  $M$  WSN nodes, assuming that ground motion recorded by these nodes is presented in terms of data packets, and these data packets are transmitted to a central node. The combined arrival rate from these  $M$  nodes at centralized node becomes a multiple Poisson process with mean arrival rate  $M\lambda_n$ . The network has been modeled as M/M/1 queue and M/D/1 queue. By considering typical data rates for WSN and real packet length from literature, the performance of the system has been evaluated in terms of QoS parameters such as mean system delay and utilization. The results show that average delay of the system decreases with increase in data rate of link (server). Moreover delay is less in case of M/D/1 queue compared to M/M/1 queue. The results also show that utilization is a linear function of traffic intensity.

### Acknowledgement

The authors are thankful to Mehran University of Engineering & Technology,s Jamshoro, Pakistan, and Sukkur IBA, Pakistan, for providing necessary facilities during research.

### References:

- [1] Youssef M., Yousif A., El-Sheimy N., Noureldin A., "A Novel Earthquake Warning System based on Virtual MIMO Wireless Sensor Networks", *in Canadian Conference on Electrical and Computer Engineering*, pp 932-935, April 2007.
- [2] Chandrakant N., Poojar S., Deepa S. P., Venugopal K. R., Patnaik L.M., "Middleware service oriented Earthquake detection in advance using WSNs", *in Fourth International Conference on Advanced Computing*, pp 13-15, December 2012.
- [3] Benson K., Estrada T., Taufer M., Lawrence J., and Cochran E., "On the Powerful Use of Simulations in the Quake-Catcher Network to Efficiently Position Low cost Earthquake Sensors", *in IEEE Seventh International Conference on E-Science*, pp 77-84, December 2011.
- [4] Cochran E., Lawrence J., Christensen C., and Chung A., "A Novel Strong-Motion Seismic Network for Community Participation in Earthquake Monitoring", *in IEEE Instrumentation and Measurement Magazine*, vol. 12, no. 6, pp 8-15, December 2009.
- [5] Sawada R., Higurashi E, and Itoh T, "An Accelerometer Incorporating A micro-Laser Encoder for A Wide Measurable Range", *in IEEE/LEOS International Conference on Optical MEMS*, pp 145-146, August 2000.
- [6] Huayin Zheng, Gengchen Shi, Zeng T, Bo Li, "Wireless Earthquake Alarm design based on MEMs Accelerometer", *in International Conference on Consumer Electronics, Communication and Networks*, pp 5481-5484, April 2011.
- [7] Li J., Yao J., and Han Y., "Design of Wireless Vibration Detection Node", *in International Conference on Computing, Measurement, Control and Sensor Network*, pp 68-71, July 2012.
- [8] Qui T., Xia F., Feng L., WU G., and Jin B., "Queuing Theory based path delay analysis of wireless sensor networks", *Advances in Electrical and Computer Engineering*, vol. 11, no. 2, pp 3-8, 2011.
- [9] Charles D. P., "The Output of an M/D/1 Queue", *in journal Operations Research*, Vol 23, no. 4, pp 750, 12 November 1975.
- [10] Lanzisera S., Mehta A. M., and Pister, K. S. J., "Reducing average power in wireless sensor networks through data rate adaption", *in IEEE International Conference on Communications*, pp 480-485, June 2009.
- [11] Liu Y. H., He Y., Li M., Wang J. L., Liu K. B., Mo L. F., Dong W., Yang Z., Xi M., and Zhao J. Z., "Does Wireless Sensor Network Scale? A Measurement Study on GreenOrbs", *in IEEE INFOCOM*, pp 873-881, April 2011.
- [12] Stewart W. J., "Probability, Markov Chains, Queues, and Simulation: The Mathematical Basis of Performance Modeling", Princeton University Press, 2009.

\*\*\*\*

# Electricity Generation With Speed Breaker and Application of Smart Grid

Engr. Shakeel Ahmed

University of Lahore, Pakistan

Engr. Prof. Dr. Suhail Aftab Qureshi

UET Lahore, Pakistan

## Abstract

Future of luminous and prosperous Pakistan is not far if management fully utilizes conventional and new renewable energy resources. To eliminate the imminent load shedding of 6000MW is the extraordinary challenge for Pakistan. Some efforts of AEDB (Alternative Energy Development Board of Pakistan) can nearly fulfill energy supply demand gap in few years by using the wind, solar, biomass and road traffic potential energy.

Major emphasis of this paper is to generate electricity from the tremendous source of road traffic potential energy. Electricity generation from traffic is newest and different idea in this innovative and modern time. A huge amount of potential energy is being wasted in the form of heat and frictional losses daily at toll plazas and everywhere on the busy road. 337 KWh to 400 KWh is being wasted every day at a single busy road. This enormous amount of energy can be converted to thousands of KWh electrical units by installing speed breaker based electromechanical system under the road and can share load of national grid. About 90,000 vehicles pass on a single busy road daily so the road traffic is wasting thousands of electrical units daily as well as millions of money.

**Keywords:** Renewable Energy, Smart Grid Application, Free Energy, Speed Breaker, Distributed Generation, Electricity Generation.

**Abbreviations:** SPWM: Sinusoidal Pulse Width Modulation

ISIS: Institute for Software Integrated Systems

CCS: Command and Control System

DSP: Digital Signal Processing

ETAP: Electrical Transient Analysis Program

## I. Introduction

After studying research literature, I came to know that early designs of power generation by road traffic were not perfect. They produced very less power only about 50 to 250 watts. My design is

totally different. A single unit based on efficient crank shaft mechanism can produce 1508W average power or 24KWh units approximately in 16h of the day at Islamabad toll plaza. If parallel speed breakers are installed at the Islamabad toll plaza, sufficient energy can be stored in the battery bank by rectifying the generated AC [1]. True sine wave three phase SPWM (Sinusoidal Pulse Width Modulation) inverter is designed to convert DC into constant AC 440V and 50Hz. Three phase power transformer 440V/11KV can transmit power towards the smart micro grid as shown in the Figure [1].

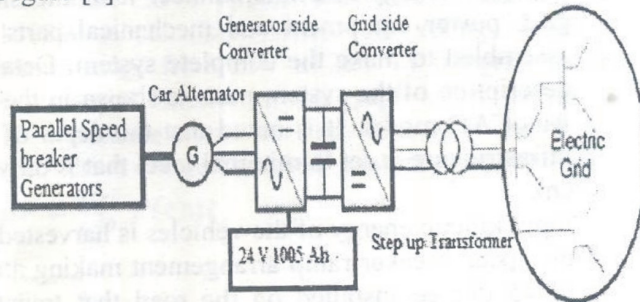


Fig-1 Schematic illustration of the system [1]

## II. Scope Of The Paper

Electricity generation from road traffic is cheapest renewable energy resource now a day that can be utilized for transmitting generated electrical power to the local smart grid. In 2012 Pakistan Electric power consumption kWh per capita was 468.91 kgcoe/annum ( $1000\text{Kgoco} = 42\text{GJ}$ ), in 2009 it was 449.32 kgcoe/annum and in 2003 it was 487.3 kgcoe/annum (Kilograms of Oil Equivalent per annum) published in World Bank fact book report 2012 [9]. It is absolutely very less when compared with the average ratings. Pakistan is the importer of energy in this regard. Renewable energy is clean and hundred percent free. Energy utilization from renewable energy resources contribute to the development and prosperity of the country. There are numerous merits of the project when we compare it with the present power situation in Pakistan [10].

Where:

- $1000 \text{ kgoe} = 42 \text{ GJ}$
- Electric power per capita [in kWh/year]  $= (1 \text{ GJ}/a=31.7 \text{ W})*(8.766)$
- Electric power per capita [in watt] = Total population electricity consumption [in MW·h/yr]  $* 114.077116 / \text{population}$
- Megawatt hours per year can be written as Watt:  $1 \text{ MW} \cdot \text{h/yr} = 1000000 \text{ Wh}/(365.25*24) \text{ h} = 114.077116 \text{ W}$

### III. Methodology

A 3D model is designed according to the laws of physics. In order to generate electricity from traffic potential energy and interconnect it to the smart grid, power equipment and mechanical parts are assembled to make the complete system. Detailed description of the system parts is shown in the 3D AutoCAD model. It is noted that the depth of the infrastructure is set to minimal level that is only 90 cm.

Input kinetic energy of the vehicles is harvested by the speed breaker ramp arrangement making angle of 45 degree installed on the road that transfers input mechanical power to the large sprocket by crankshaft attached with ramp via frictionless bolts on both ends. Rectilinear motion of the crank shaft is converted to rotational motion by large sprocket which is synchronous with the ramp rotation for 45 degree because width of the ramp and radius of the large sprocket are the same. When a tire of vehicle strikes the ramp, it pushes downward from the top side. A gear system, flywheel, special ball bearing of cycle hub and large sprocket are placed on a common hub or center axis.

Large pulley of the gear is coupled with the small pulley of alternator with a belt to increase rpm of variable speed DC generators shown in 3D view of the model. Gear ratio is 9.3 to get 1250 rpm of 24 volt 1500 Watt DC generator that also give output on 800 rpm [3]. Car alternator is used in this project to manage variable speed and give maximum output power.

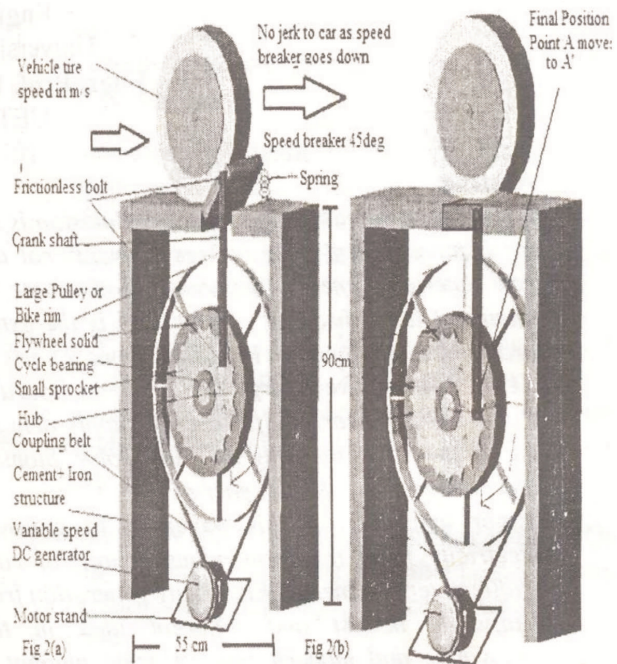


Fig-2 In 2(a) 3D Modeling and parts assembling of speed breaker shown, in 2(b) point A moves to final position A'

Due to variable speed of the AC generator fluctuating voltage and frequency will produce so we need to rectify the output. Rectifier, charge controller and voltage regulator used to charge a battery bank of 24V 1005 Ah.

A single speed breaker unit can fully charge this battery bank in only one hour if it is installed at the toll plaza of Islamabad motorway interchange. True sine wave 3 phase SPWM (Sinusoidal Pulse Width Modulation) inverter converts 24V DC to a constant 440V AC output at 50 hertz frequency, that is used for single and three phase AC loads when transmitted to smart micro grid [2]. This sufficient power can be used for multiple purposes like road lights, signals, toll booth computers, cameras, servers, fans and nearby consumers [4].

### IV. Block diagram

Complete project is initially divided to subprojects. Steps towards project completion are presented in the block diagram to get expected results. Each sub block is designed with description.

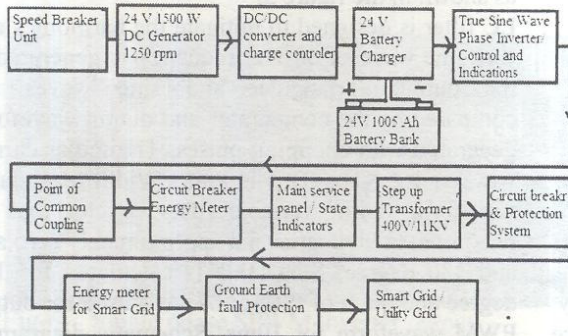


Fig-3 Block diagram of electricity generating speed breaker system and smart grid connection

## V. Input Mechanical Power Calculation

Mathematical parameters and relations are defined here for hardware designing, power, torque, force and rpm calculations.

Let a car with mass 1600kg with velocity  $u_1$  10 km/h or 2.77m/s collide with speed breaker having velocity  $u_2$  zero.

$$\text{Mass of car (Approximate)} = 1600 \text{ Kg}$$

$$\text{Mass on one wheel} = 400 \text{ Kg}$$

$$\text{Ramp angle from ground} = 45 \text{ deg}$$

$$\text{Ramp width=Large sprocket radius} = 12.7 \text{ cm}$$

$$\text{Circumference of large sprocket} = 79.8 \text{ cm}$$

$$\text{Input Force by vehicle weight} = F = mg = 400 * 9.81 = 3924 \text{ N}$$

$$\text{Acting force is horizontal component} = F * \cos \theta = 3924 \cos 45 = 2775 \text{ N}$$

$$\text{Time in which small sprocket turns to 0 degree from 45 degree} = t$$

$$\text{Car speed} = 2.77 \text{ m/s}$$

$$\text{Arc distance } 9.98 \text{ cm will be covered in } t = 1 / 2.77 * 0.0998 = 0.036 \text{ s}$$

$$\text{Work done by the vehicle force} = F * d = 2775 * 0.0998 = 276.945 \text{ J}$$

$$\text{Power theft by speed breaker from vehicle potential energy} = \text{work done / time taken} = 276.945 / 0.036 = 7693 \text{ Watts}$$

## VI. Output Power Calculation

Mechanical losses like bearing friction, belt pulley friction, windage and slip rings are about 30% approximately due to a smart design.

$$\text{Power transmitted to DC generator} = P_{in} * 0.7 = 5385 \text{ W}$$

A 5 KW generator cannot be used because it requires heavy torque to rotate and output response become highly nonlinear in only 5 seconds so we cannot utilize maximum output power due to high inertia of the rotor. Electrical losses are due to the voltage regulator circuit, rectifier, filter, 24 V batteries and inverter circuit. 50 percent electrical power lost generated by car alternator due to variable rpm or very low DC voltage below the rated rpm. So we select the 24V 1250 rpm 1500 Watt DC generator for utilizing maximum power. Maximum o/p electrical power =  $5385 * 0.5 = 2692 \text{ W}$

$$\text{Width of speed breaker} = 12.7 \text{ cm}$$

$$\text{Car time to cover this distance} = (1/2.77) * 0.127 = 46 \text{ ms}$$

In 46 ms maximum power generated at the output of alternator = 2692 Watts

Due to inertia of the flywheel DC generator stops after time 25 s approximately. Average power 1508W is calculated where the voltage level is within range from 23V to 28V by integrating the exponential function of the graph as shown up to 10 s because mean service time of a car is 10 seconds. Average electrical power of the alternator is  $P = \frac{1}{t} \int_0^t P(t) dt$

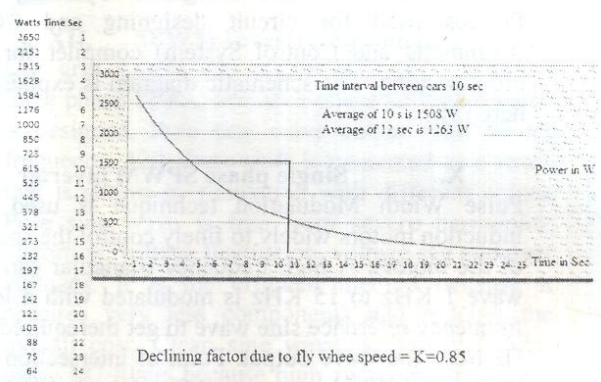


Fig-4 Output electrical power of alternator vs time due to declining factor  $K=0.85$ .

## VII. KWh Calculations

In one minute 6 cars passed on the speed breaker because mean service time of a car is 10 seconds. Average power generated in 10 seconds is 1508 W. After 10 sec next car leaves the toll booth. Same mechanism repeats and power boosts from 615W to 2692W as shown in the graph and system never stops for 16h in the busy toll plazas like Islamabad.

In one hour average energy generated and stored  
 $= 1.508 \text{ KWh}$   
In 16h energy stored  
 $= 1508 * 16$   
 $= 24.128 \text{ KWh}$   
Energy generated by 14units = 337 KWh

### VIII. Payback time calculation

From the previous result 14 units produce 337 KWh daily, 10,110 KWh in a month and 123 MWh in the year. WAPDA (Water and Power Development Authority) is selling one unit at the rate of Rs-20 for commercial loads approximately. Initial capital cost, operational and maintenance cost of a year for 14 units is Rs-1,381,000 that can be returned in only seven months and after this period monthly saving is Rs-202,200 that is the excellent result of this project.

### IX. Simulation and Programming

24V DC is usable for carrying DC loads of the system. For AC loads we need true sine wave inverter for carrying sensitive loads. Simulation of SPWM (Sinusoidal Pulse Width Modulation) inverter is designed to minimize the system cost and achieve true sine wave. Modern circuit designing and programming techniques for inverter minimize the losses and improve the inverter efficiency up to 90 percent from 60 percent. ISIS (Institute for Software Integrated Systems) or Proteus used for circuit designing and CCS (Command and Control System) compiler for C programming. The schematic diagram is explained here [2].

### X. Single phase SPWM inverter

Pulse Width Modulation technique is used in induction motors widely to finely control the speed of the motors. A high frequency triangular carrier wave 1 KHz to 15 KHz is modulated with a low frequency reference sine wave to get the required 50 Hz true sine wave output. Point of intersection of both waves decides to on or off pulses duty cycle. Sine weighted switched pulses are produced that are used for operating 2 MOSFET of N-type IRFP150N that are connected with transformer. PIC 16F877A is used for generating a pure sine wave of 50.34 Hz frequency in the output of inverter from the 12V DC. LCD is integrated with the PIC to show the voltages, system status, protection alarms and temperature [2].

In this simulation title of the paper is programmed as shown in the figure 5.

LC filter is designed to mitigate the harmonics and true sine wave of 50 Hz frequency is generated at the output. Triangular and sine waves are compared by the comparator and output waveform generated with chopping pulses. Triangular carrier wave is 1.2 KHz. This is Pulse Width Modulated waveform with variable duty cycle that is maximum at 90 degree and approximately zero at 0 and 180 degree. Sine table is calculated for 180 degree and pin 9 of PIC16F877A is used for output PWM waveform for 10ms. Schematic diagram is shown in the figure 5.

For generating negative half cycle of output waveform this sine table is repeated for next 10ms. At this stage first MOSFET remains off and second MOSFET is on with defined duty cycles. When the first MOSFET is on for 10ms with defined on and off duty cycle second MOSFET remains off. Power transformer of 3 primary input and 2 secondary is selected to step up the voltage to 220V AC.

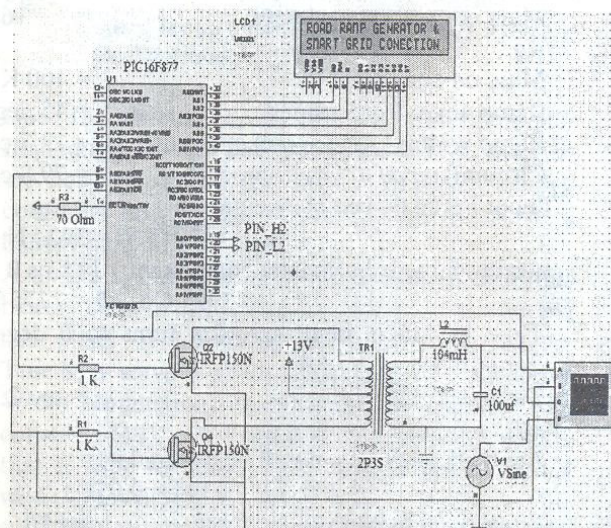


Fig-5 Single phase true sine wave SPWM inverter schematic

SPWM and true sine wave is shown in figure 6. Pure sine wave inverters produce very clean waveform that is free from harmonics. Sensitive electronic equipment can be safely run with this high quality pure sine wave inverter like fax machines, digital computer, electronic modules and SMPS [2].

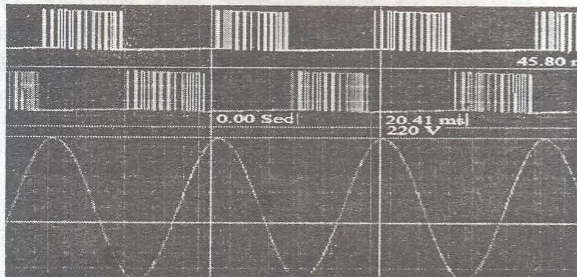


Fig-6 Single phase SPWM inverter output

## XI. Simulation of 3-phase SPWM Inverter

Computational analysis, circuit designing and programming abilities is the basic requirement for simulating three phase SPWM inverter. Schematic ISIS circuit diagram is shown in the fig-7. Numerical techniques are used by comparing the 12 KHz triangular wave with 50 Hz modulating signal. Each MOSFET is modulated with same triangular carrier waveform but different firing angle of 120 degree [2].

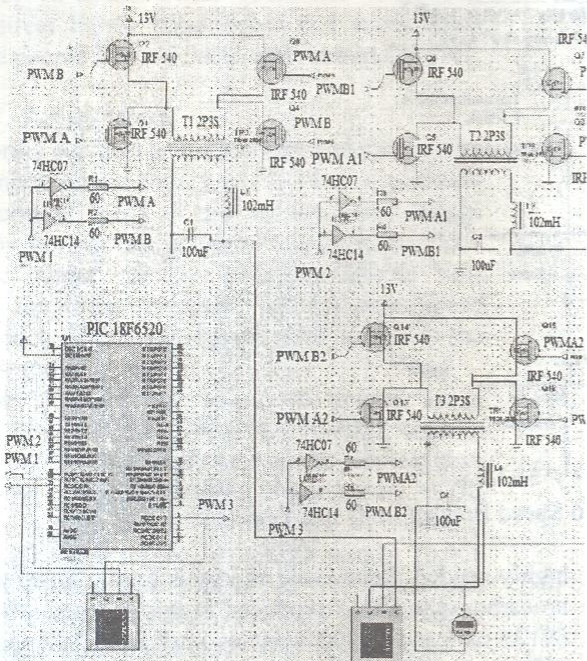


Fig-7 Schematic of 3 phase true sine wave SPWM Inverter by PIC 18F6520 in ISIS

Modulating signal is divided into numerous steps according to the 360 degree angle depends upon the carrier wave frequency. For verification purposes to generate three phase waveform 50 Hz

sine wave is divided into 96 steps and calculated sine table for each value. Sine table calculations provide on-off duty cycle to switching MOSFETs.

Finally real time simulation of 3-phase inverter with 120 phase shift is successfully run between three sine waveforms. It is cleared in the figure shown here with red, blue and yellow colors. However, in this black & white printing only different levels of grey can be seen.

It is recommended that specific values are used for different inverter powers.

16 KHz PWM for 1KW inverter

5 KHz PWM for 100KW inverter

1 KHz PWM for 1MW inverter

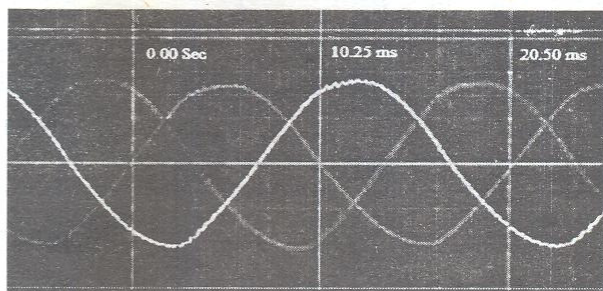


Fig-8 Three phase SPWM inverter output

## XII. SPWM Inverter Advantages

Our grid system can import or export power in three phase 11 KV line so 3-phase SPWM inverter is designed. Pure sine wave output with 50 Hz frequency, 120 phase shift is generated as a result that is shown in simulation with different colors. Pure sine wave is free from severe harmonics, distortion, voltage fluctuation, voltage sag and over voltages. It is the efficient method because it requires very less components and reduces the overall cost. Clean sine wave is generated after using LC filters because high switching frequency produces harmonics. MOSFETs can easily handle high switching frequency.

DSP (Digital Signal Processing) based modules in PIC 18F6520 are used for generating three PWM signals that are different in angle. SPWM inverters have 90 percent efficiency which is very high as compared to old inverters that had 60 percent efficiency. This technique also increases the life of batteries as no overloading current is drawn to the circuit. This modern power inverter technique is system efficient and perfect for feeding sensitive loads [5].

### XIII. Smart Grid Configuration

Smart grid is a digitally controlled real time network to increase the reliability, sustainability and efficiency of the distribution system. In Fig 9, an example is given where 6 generating units feed 11KV smart grid and load flow analysis is calculated in ETAP (Electrical Transient Analysis

Program). 14 speed breaker units generate 337 KWh units in a day and it is transferred to smart grid. A smart grid can also integrate renewable energy resources so electrical output can be connected with the existing distribution network supply of 440V or 11KV supply [11].

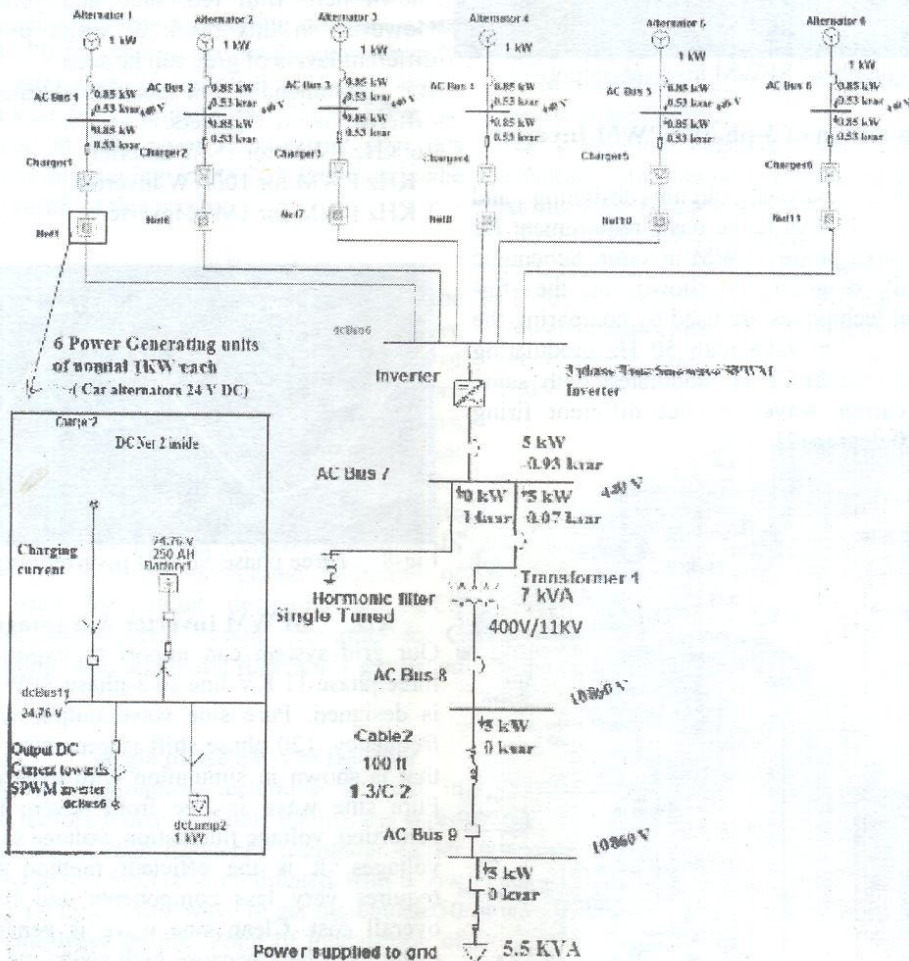


Fig-9 Smart Grid connections of 6 Speed Breaker units in ETAP [1]

Single line diagram in ETAP assure the practical implementation of the proposed load flow solution. DC bus bar, AC bus bar, circuit breaker, transformer, rectifier, inverter and all the appropriate equipment are very important[1], [7].

### XIV. Results and Conclusion

For power deficient countries like Pakistan integration of renewable energy power sources with smart grid is

highly needed. Renewable energy is totally green and no carbon-di-oxide is produced in this process. About 69120 cars and 90000 vehicles pass from Islamabad toll plaza or Niazi Chowk, Lahore every day in 16h. This equates 337 KWh to 400KWh that is wasting daily. Early ideas of electricity generation from speed breaker generate 25-250 W but this advanced model generates maximum 2.692 KW and average 1.508KW depending upon the net weight of the car.

Single speed breaker unit generates 24 KWh units daily for 16h. Similarly 14 units produce 337 KWh daily, 10110 KWh in a month and 123 MWh in the year. This is similar to 21 KW wind turbine on the road providing constant output. Initial capital cost, operational and maintenance cost of a year for 14 units is Rs-1,381,000. Tariff for commercial users is Rs-20 so capital cost can be returned in only 7 months. After this period monthly saving is Rs-202,200 that is the excellent result of this project.

Three dimensional modeling in AutoCAD helps to understand the practical working of all the mechanical parts. SPWM true sine wave three phase inverter is designed in this project to increase the inverter efficiency 60 to 90 percent to carry sensitive loads.

Generated electricity carries toll booth loads like computers, fans, lights, traffic lights and signal lights. This amount of energy can be used for carrying load of 33 homes with 1KW average load for 24 hours of the day. This energy can also light 240 LED lights of 50 Watt for 12 hours. These bulbs can be of road lights or street lights. Road lights and street lights prevent the people from accident and robbery [8] [10].

## XV. Future Work

A clock spring can also be used on the common hub to store the input kinetic energy in the form of potential energy. Constant speed of the AC generator can be achieved by storing vast potential energy in the clock spring. Ac output can be used for definite time depending upon the designing of the new speed breaker model. There will be no need to rectify the AC if clock spring is used.

Capital cost is Rs-65/Watt that is 50 percent lesser than solar system Rs-131/Watt so payback time is very less. Unit has minimal set up and trialing cost. Payback time is only 7 months estimated so AEDB (Alternative energy Development Board of Pakistan) should focus on this project. If AEDB installs 10,000 such speed breaker systems on all toll plazas and different locations of Pakistan, 211 MW can be added on the National grid of Pakistan. This report should be submitted to the research and development department to make a complete feasibility report to practically implement it in our country roads. AEDB, NEPRA and WAPDA should implement this project soon. Multiple stand-alone smart micro grid systems can help to share the load on national grid.

## XVI. References

- [1] *Integration of Distributed Generation in Low Voltage Networks: Power Quality and Economics* By Konstantinos Angelopoulos Glasgow Year 2004.
- [2] Pankaj H Zope1, Pravin G. Bhangale "Design and Implementation of carrier based Sinusoidal PWM Inverter "International Journal of Advanced Research in Electrical, Electronics and Instrumentation Engineering Vol. 1, Issue 4, October 2012.
- [3] *Electric Machinery Fundamentals* (Stephen J. Chapman BAE SYSTEMS Australia).
- [4] ISSN 2090-4304 *Journal of Basic and Applied Scientific Research* "A Novel Speed-Breaker for Electrical Energy Generation Suitable for Elimination of Remote Parts of Power Systems where is Near to Roads" Mohsen Partodezfoli1, Horieh Rezaey1 Islamic Azad University, South Tehran Branch, Iran 2012.
- [5] "A Microturbine generation system for grid connected and islanding operation". A. Bertani, C. Bossi Member IEEE, S. Spelta, F. Tivegna, Accepted for presentation at IEEE PSCE 2004, New York, October 10-13, Year 2004.
- [6] T.T. Madangombe, K. A. Folly, P. Pillay "Standards and Technical Guidelines for the Interconnection of Renewable Energy Sources into the Grid "IEEE PES PowerAfrica 2007 Conference and Exposition Johannesburg, South Africa, 16-20 July 2007.
- [7] C. Potter, A. Archambault, and K. Westrick, "Building a smarter smart grid through better renewable energy information," in Power Systems Conference and Exposition, 2009. PSCE '09 IEEE/PES, March 2009, pp. 1-5.
- [8] Ali Keyhani. "Design of Smart Power Grid Renewable Energy Systems" Singapore: John Wiley & Sons, INC., Publication, 2012.
- [9] Pakistan Electric power consumption kWh per capita is available here in this link [http://www.photius.com/ranking/economy/electricity\\_consumption\\_per\\_capita\\_2012\\_0.html](http://www.photius.com/ranking/economy/electricity_consumption_per_capita_2012_0.html).
- [10] Electricity consumption by worldwide countries [http://en.wikipedia.org/wiki/List\\_of\\_countries\\_by\\_electricity\\_consumption](http://en.wikipedia.org/wiki/List_of_countries_by_electricity_consumption).
- [11] Features of the smart grid [http://en.wikipedia.org/wiki/Smart\\_grid](http://en.wikipedia.org/wiki/Smart_grid).

# Hybrid Renewable Energy Source Implementation in Pakistan

Engr.Hamid Ali, Dr.Naeem Arbab, Engr. Qazi Waqar Ali  
University of Engineering & Technology, Peshawar Pakistan

## Abstract

A solar-wind hybrid power generation system has been presented here. The application based system illustrated in this paper is designed on the basis of the solar and wind data for Pakistan. The power generated by the system is intended for domestic use. The most common source of unconventional power in homes is battery based UPS (Uninterrupted power supply) inverter. The UPS inverter charges the battery with conventional grid power. This system will charge the battery of UPS inverter by using only wind and solar power, which will make the system cost effective and more reliable. The reason for using both solar and wind is that recent studies have proven that combined system can be more productive and consistent and other thing is that neither of them can be used for continuous power generation. In the system illustrated in this paper the solar-wind system provides power periodically which is controlled by electronic methods and a microcontroller is used to monitor the power from both the inputs. The switching action is provided from the microcontroller to the battery charging based on the power received from solar photovoltaic panel and wind generators. In this paper, an efficient system has been presented comprising of solar panel, wind generator, charge controller and charge storage unit (battery). Solar panel is selected as the main input and the wind resource will be used only in the absence of the solar photovoltaic (PV) output.

**Keywords** photovoltaic, hybrid, UPS, grid

## 1. INTRODUCTION

In the recent times the need for energy has increased globally. The electrical energy has now become the base for almost everything. This has made us to increase our energy production which in turn has put extra pressure on our non-renewable resources. The other way is to generate energy by using renewable resources of energy. The renewable resources like hydro power are being utilized to generate power but these projects take years to complete and there are lots of other factors involved which discourages these projects. The more suitable form of renewable energy in the modern era is the solar energy. The solar energy can be utilized in many ways. The two of the most basic uses of sun light to make electrical energy are:

- ✓ Solar Photovoltaic.
- ✓ Solar Thermal.

Solar photovoltaic is a system to convert light energy (photons) into electrical energy. Solar thermal means to use the heat energy of the sun to generate electrical energy thermally. The solar water heaters and steam based solar turbine are the systems where solar thermal technique is used. The paper presented here is based on the solar photovoltaic systems. The solar photovoltaic has given us

the chance to become producer of easy and clean energy. The solar systems can be installed on a small house or a big industry. The solar panel uses the solar irradiance to generate electrical energy. A solar panel uses energy of the incident photons on its surface to generate electrical charge. The solar panel consists of small silicon cells. The cell output voltage for a single cell is of the order of 0.7V (under open circuited conditions) which cannot be utilized for power generation. These cells are placed in series-parallel combinations to get usable voltage. The other renewable energy resource is the wind energy. The wind energy is utilized by converting the kinetic energy of wind in to rotational motion by using a wind turbine. This rotational motion is converted into usable electrical energy. For this purpose a wind generator has been used which contains a wind turbine and an alternator. The systems with only solar or wind generation are productive but there are problems linked with both of them. The solar power is not available for 24 hours and wind is not continuous all the time. So a hybrid system containing solar and wind has been designed to overcome these shortcomings. A system has been designed in this paper which utilises both solar and wind power generation systems. Recent researches in the field of renewable resources shows that the solar and wind hybrid power generation system can work with increased outputs and increased practicality [6]. The block diagram of this system has been shown below

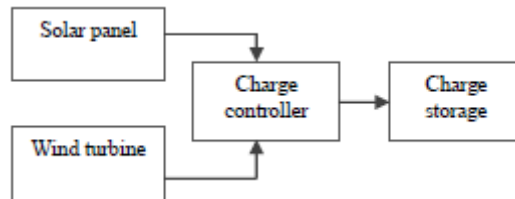


Fig 1: Block diagram of the solar wind hybrid system

## 2. OBJECTIVES

The rising environmental pollution, limited fossil fuels and natural gas reserves and the unfriendliness of their use for electric power production is resulting in growing interests in the utilization of renewable sources of producing electrical energy. The emerging green technologies like photovoltaic and wind turbine generator technologies is creating opportunities for generating electric power in an harmless manner throughout the world.

Estimates by the World Bank claim that as much as 40 percent of the world population still lives in villages and rural areas are not tied to utility grids. A more feasible way of providing electricity to such rural areas is by using the new renewable technologies rather investing in transmission infrastructure to connect them to the main utility power grids. For the villages farther than 3 KM from the nearest

transmission line, it is usually economically more convenient to use a hybrid based stand alone system.

Solar radiation and wind speed are having complementary profiles among the unpredictable and randomly behaving renewable energy sources. Stand alone hybrid system usually take advantages of this particular characteristics combining photo voltaic panel and wind mills in conjunction with a diesel power backup generator. However diesel generator demands fuel supply then their use in isolated as can be troublesome and, in comparison with renewable energy source, uneconomical. In some application they can be avoided by including in the system adequate energy devices like battery bank. Since storage cost in all represent the major economic restraint, usually PV and wind systems are appropriately sized to minimize its requirements. So wind power is lower in cost than PV power approximately by a factor of five, so it often gets the main role in generation.

### **3. Requirement of Alternates of Energy and its Scope in Pakistan**

Due to the advancement in electronics almost every appliance that we use now is running on electrical energy. According to the predictions of the IEA (International Energy Agency) the natural sources (Water, Natural Gas) of electrical energy that are used most commonly for electrical energy production will be able to provide energy till 2030-35. Reacting on these facts provided by IEA many countries are taking steps to get maximum energy from other natural sources for their future use. Realizing this problem Pakistan is also taking steps to provide energy from other sources and the main concentration is on Wind and Solar technologies. Pakistan government has a goal of getting at least 7% of the total energy from these two sources by year 2030. Achieving 9700 MW from wind power is planned by year 2030. With this government will be able to provide 7874 far-flung distant of utility grids villages of Balochistan and Sindh Provinces. Alternative Energy Development Board (AEDB) is looking for the National and International companies which are interested in producing energy from the alternate sources. AEDB has started its first phase of providing electricity to the 400 remote areas of Sindh and Balochistan within few years.

### **4. Hybrid Power System**

A hybrid power system is in which the load is provided by two or more power sources. Renewable energy sources, such as solar and wind are normally combined with each other because they are the most powerful energy sources. Hybrid systems can be designed to fulfil the requirements at lowest acceptable cost, which is the key to getting market.

The energy consumption is gradually increasing and the deregulation of electricity has caused that the amount of production capacity of high power stations cannot fulfil the demand. A method to fill out the space is to make alternative energy sources e.g. wind turbine, solar panels, micro turbines and photovoltaic system. Now a day the

wind turbine and solar technology is one of the most capable alternative energy technologies.

**Table 1 Non Renewable and Renewable**

Non-Renewable	Renewable
• Natural gas	• Hydro
• Ultra supercritical Pulverized coal	• Wind
• Integrated coal Gasification	• Solar
• Nuclear	• Biomass
• Ultra clean coal combined cycle	• Geothermal / hot rocks

### **5. Advantages of Wind Energy**

The most significant advantage of the wind energy is that it is produced by the source which is most unlikely to vanish as compared to other natural sources like coal, natural gas.

Wind energy is safe for the environment because it does not produce chemicals like Carbon dioxide. So it does not pollute air.

The most cost effective source of energy among the renewable energy sources is the wind energy, which costs only 4 to 6 American cents per KWH relating to the environment and location of the installation.

The most suitable place for wind turbines is farms and mostly farms are placed in countryside areas and this will also help in providing electricity in rural areas.

Wind energy is “home-grown” and green (i.e environment friendly)

### **6. Disadvantages**

Wind power is an economical energy source but its initial cost is much greater than the initial investment of other energy sources like coal and natural gas.

Now a day's most of home appliances are dependent on electricity so they require electricity for 24 hours, but wind energy source can not provide energy all the time because wind does not blow all the time.

A wind power source does not produce chemicals as other sources do but they produce noise pollution which is caused by the movement of its rotor blades.

### **7. Advantages of Solar Energy**

Solar cells convert the solar radiation directly into the electricity using photovoltaic effect without going through a thermal process.

Deserts and remote areas are ideal place for the solar power generation because they provide maximum solar power and the space for the solar panels. So this will help in providing the electricity to the rural areas of Pakistan.

Solar cells are reliable, modular, durable and generally maintenance free and therefore, suitable energy in isolated and remote areas.

Solar cell are quite, compatible with almost all environment s respond instantaneously to solar radiation and have an expected lifetime of 20 or more years.

## 8. Disadvantages

Currently, solar energy is only viable for individual household use rather than large-scale production.

In winter, there is a decrease in power generated due to the decrease in sun and there is no generation at night.

Highway Emergency Telephones are being powered using solar energy.

Keeping vaccine and medicine cold by powering refrigerators.

"Empower Consultants of New Zealand is a renewable energy specialist is working on the project in the deserts of Gawadar (Balochistan). The goal of the project is to provide approximately 30 kWh and to facilitate the poor people of that remote area." "The 'prime mover' for the project is centered on a 6 kW solar PV array, with a 10 kW inverter, large capacity (90 kWh) battery bank, 100 Amp 120 VDC solar charge controller and 7 kW backup diesel generator forming the backbone of the system".

Solar energy does not have large scale implementation in Pakistan. Different companies are making, watches, calculators and cellular phones powered by photovoltaic cells, battery chargers, garden lights and low power photovoltaic lamps.

The Siemens Pakistan has installed microwave link repeater stations on the Lahore-Islamabad Motorway, in the Salt Range area and more than 350 emergency call boxes.

## 9. Current solar energy applications in Pakistan

Now in Pakistan different technologies are using Solar and photovoltaic technologies on small scale.

### 9.1. Solar Water Pumping & Home Electrification in a Balochistan, Pakistan

The main purpose of this project was to help women who are working to get water from the well and also to provide the villagers lights in the evening. This will also help villagers to save money.

This project was a low cost because most of the components installed do not require any maintenance. PV panels used have an average life of 30 years. Hand pump is expected to last about 4 years. The lights have also estimated life of about 1 year. Both photovoltaic and solar thermal technologies have great potential and application in Pakistan; however, they are not being utilized on major scale anywhere in Pakistan. On small scales the solar energy has been utilizing for more than 25 years. The following is some of the application areas of solar thermal and photovoltaic technologies.

Most efficient way to utilize solar energy is using photovoltaic cells it converts solar radiations into dc voltage.

## 10. Current Wind energy applications in Pakistan:

AEDB installed a total of a 140 micro Wind Turbines (139 of 500 watt each and one of 10 KW) in remote village of Sindh and Balochistan Provinces to supply power to residents for household utilization. The mechanism was designed such that one turbine was utilized to electrify 5 household. Most of the turbines installed by AEDB were imported from China and a few were manufactured locally. The details in this regard are as follows:

### 10.1 Imported

A total of 124 micro wind turbines of 500 watt capacity were imported from China. The turbines were of (Model No. and detail). These turbines have been installed as per detail given below.

All these turbines have satisfactory results. The functionality of these turbines has been very good. Though, overall system installed in house experienced failure. Almost 60% of the turbines got drained. This happened because the dwellers utilized more power than permitted.

### 10.2 Locally manufactured

A total of 15 micro wind turbines 500 watt capacity were developed through local market. The generators for these turbines were imported from China. Resets of the unit were manufactured within the factory. The developer was Shah Kamal, Karachi. These turbines were installed in following locations.

These turbines have not given successful results due to malfunctioning blade design. Most of these have been dismantled.

## 11. Pakistan Council for Renewable Energy Technologies

PCRET installed a total of 134 micro wind turbines in remote villages of Sindh Province to supply power to residents for household utilization. Most of the turbines installed by PCRET were imported from China and a few were imported from India and a few were manufactured locally. The details in this regard are as follows.

### 11.1 Imported

In year 2002, 14 micro wind turbines (6 of 500 Watts each and 8 of 300 watts each) were imported from China. out of these , 8 were installed in coastal belt of Balochistan ( 3 at Dhoajee, 2 at Phore and 3 at Mata Mandar Hinglaj, Lasbella) and 6 wind turbines were installed in the coastal areas of Sindh (one at super High way Karachi, 3 at Gujjo and 2 at Kharo Chan).

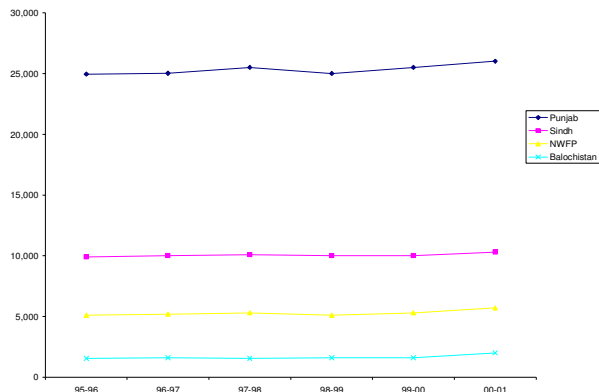
In 2004, PCRET imported 116 micro wind turbines of 500 watts each and installed in remote coastal areas of Sindh and Balochistan. Through this Project, 1,430 household have been given electricity. All these turbines were also china made, PCRET has Installed these turbines through its own expertise.

## 11.2 Local

PCRET also has made efforts to initiate local manufacturing Of 500 watts wind turbines under ToT from China and 5-10 Kw wind turbines under ToT from some European countries. These turbines have passed all the laboratory tests and now are going under field testing phase, the details of private company who have been engaged by PCRET.

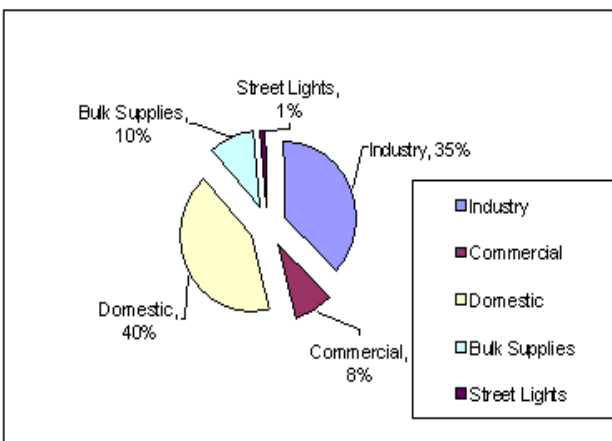
## 12. Current Wind energy applications in Pakistan

Windmills are also used to provide electricity for the street lights. These types of street lights are used at Defense Housing Authority (DHA)



The graph below is showing the percentage use of the electricity for the different sectors of Sindh. This graph shows that maximum consumption is in domestic sector as the electricity costs more when it is produced from the conventional sources, so there should be some concern for the production of electricity from the other natural resources.

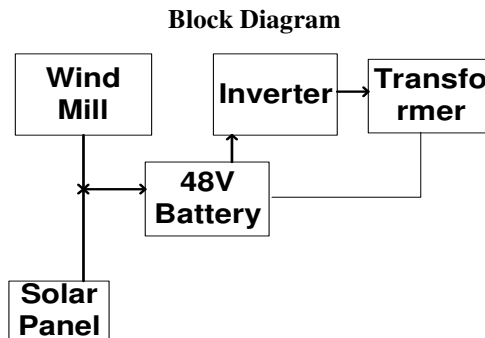
Graph-2: Electricity consumption in province of Sindh



## 13. Proposed Work:

The main objective of the project is that it should be able to run 1 KW load at 50 Hz. We have divided this project into different phases and each phase has a specific goal.

The top level diagram of a hybrid renewable energy source is given below:



## 14. Future Enhancements

### 14.1 Low Cost Wind Turbine Implementation

In future a low cost wind turbine can be constructed that can be connected to our system with some enhancements.

### 14.2 Solar Panels with Tracking System

Developing a tracking system for the solar panels which will ensure maximum energy transfer from sun.

### 14.3 Improving capacity of batteries at low cost

Another aspect that can be improved is the increase in capacity of batteries.

### 14.4 Efficient and Low cost Solar Panels

Someone can work on the solar panels so that to make them cost effective.

## REFERENCES

- [1] "Solar Energy Utilization" chapter 30 ASHRAE Handbook, Applications, .
- [2] Wind hybrid systems technology characterization by Vaughn C Nelson, Ken L Starcher West Texas A&M University,
- [3] P. J Lunde Solar Thermal Engineering: John Wiley & Sons,
- [4] A.W. Culp, Principles of Energy Conversion, 2nd ed., McGraw-Hill,
- [5] Wind Generators and Turbines by A. Binder,
- [6] S. Wei, B.Wu, F.Li, X.Sun, Control Method for Cascaded H-Bridge Multilevel Inverter with Faulty level Cells,
- [7] R. Erickson, S. Angkititrakul, and K. Almazedi , Multilevel Matrix System power converters and control of renewable energy systems University of Colorado Boulder, Colorado,
- [8] Frede Blaabjerg, Zhe Chen, Remus Teodorescu Aalborg University, Institute of Energy Technology, Denmark,

## Authors:

### Prof.Dr.Naeem Arbab

Professor, EED, UET Peshawar, Pakistan

### Engr.Hamid Ali

Student,

MSc Electrsical Power Engg, UET Peshawar, Pakistan

### Engr.Qazi Waqar Ali

Student

MSc Electrical Power Engg, UET Peshawar, Pakistan

# Simulations of Interleaving Two Switched-Inductor Hybrid DC Boost Converters For Fuel Cell Applications

Umar T. Shami<sup>1</sup> and Tabrez A. Shami<sup>2</sup>

<sup>1</sup> University of Engineering and Technology, Lahore, Pakistan.

<sup>2</sup> University of Central Punjab, Lahore, Pakistan.

## Abstract

This research paper introduces the interleaving of two switched-inductor hybrid units for increasing output DC voltage of a DC converter. The benefits of the proposed converter include high DC voltage gain and reduced ripple current. The proposed converter operates in four modes, working of all the four modes are discussed. A conventional method of controlling the proposed converter is adopted. Simulated steady state analysis including waveforms of converter input current, inductor current and voltages, power electronics switching device current and voltages, output load current and voltages are presented. Results show that the proposed converter demonstrates the maximum efficiency of approximately 85% at a duty ratio of 0.4.

## Index Terms

Energy Conversion, Fuel Cells, Energy System Modeling, DC-DC Power Conversion, Interleaved Step-Up Dc Converter, Switched-Inductor Step-Up Dc Converter.

## 1. INTRODUCTION

Wing to the overwhelming applications of fuel cells (FC), electrical engineers and researchers have contributed remarkable research in this area. The major research areas include portable power, transportation, and connection of FCs to distribution-grid (distributed generation). An inherent characteristic of a typical FC is that it generates low DC output load voltage [1], which is usually less than the voltage required for DC-link voltages. Therefore, FCs are used in various applications by means of a DC step-up boost converter. One disadvantage of conventional DC boost converter is that the filter-capacitor is normally large to reduce the ripple current. Another problem is that the output load voltage is sensitive to duty ratio D, especially when this ratio ranges from 0.5 to 1 [2].

Isolated DC boost converters equipped with power transformers are normally bulky in volume. The parasitic inductance of the transformer cause efficiency degrading factors such as unavoidable voltage burden, excessive transient current, conduction losses during the turning on and off the power electronics switching element, and electromagnetic interference (EMI) [3]. Conventional DC converters employing coupled-inductors or flyback transformers, comfortably step up output voltage, nevertheless the leakage inductance of the coupled inductor causes high voltage stress and decreases the efficiency [4]. Techniques have been proposed to resolve the above mentioned problems [5]–[11]. Interleaved DC boost converters include features such as output load current

ripple minimization, inductor size reduction, and uniform heat dissipation [5]–[8].

The switched-inductor hybrid circuit technique as presented by Axelrod et al. [10], provides an excellent high DC voltage gain. In addition, this technique reduces current stresses in the power electronic switching devices that lead to low conduction losses [10]–[11], however, the issue of ripple current may rise as D decreases.

This research paper proposes a circuit topology that

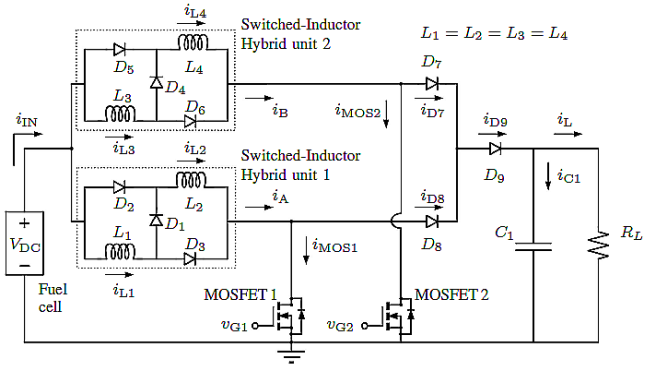


Fig. 1. The proposed interleaved switched-inductor hybrid DC boost circuit.

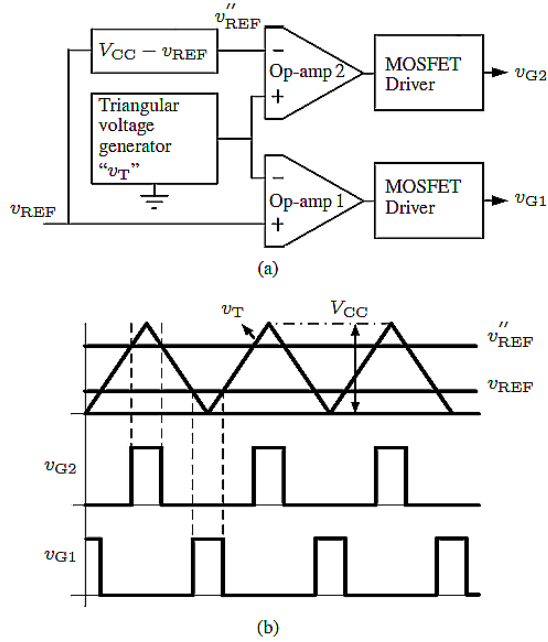


Fig. 2 Generation of the duty cycle signal. (a) control circuit scheme. (b) the timing waveforms.

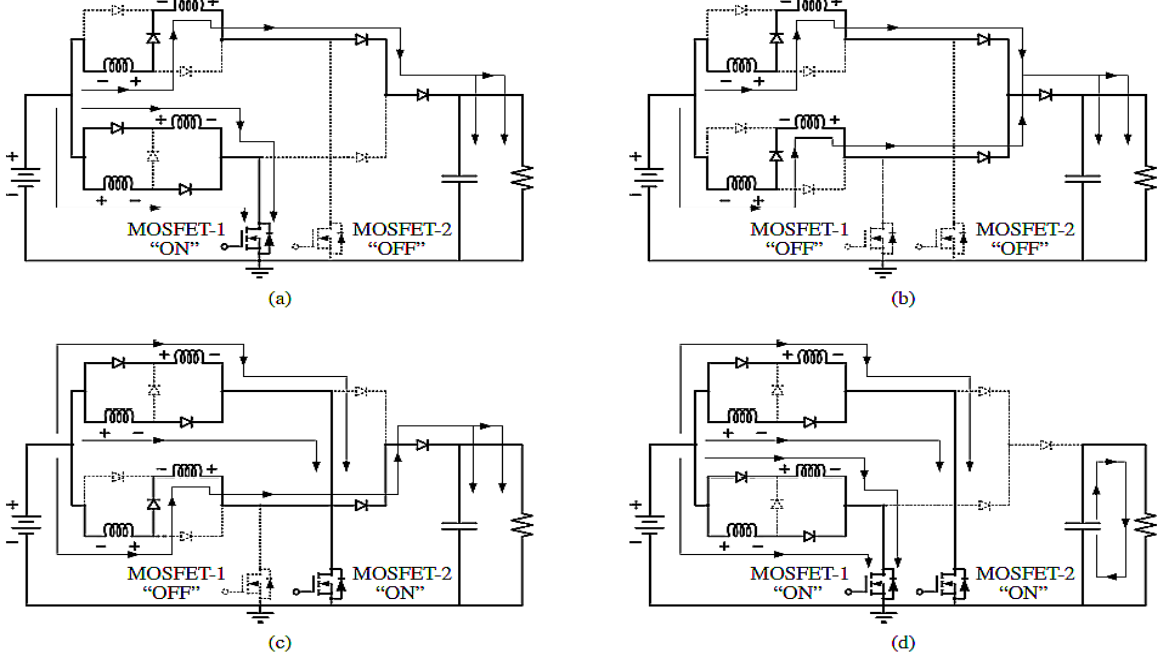


Fig. 2 Various operating modes along with current-flow path, of the of the proposed switch-inductor hybrid DC converter. (a) Mode 1. (b) Mode 2. (c) Mode 3. (d) Mode 4

interleaves two switched-inductor hybrid units. The merit of using the switched-inductor hybrid unit is that it provides a DC voltage gain to the load. Whereas, the merit of interleaving includes ripple current reduction, whereas another merit is that additional switched-inductor hybrid units can be interleaved, and the circuit may be expanded. It is understood that by interleaving additional switched-inductor hybrid units, the ripple current may further decrease. Such a technique may aid in reducing the filter capacitor size. The scope of this research paper is to demonstrate the interleaving of only two switched-inductor hybrid units.

## 2. INTERLEAVED SWITCHED-INDUCTOR HYBRID DC BOOST CONVERTER

Fig. 1 displays the proposed interleaved switched-inductor hybrid DC boost converter circuit. A fuel cell is connected to two switched-inductor hybrid units, where switched-inductor hybrid unit number 1 consists of inductors  $L_1$  and  $L_2$  and fast-switching diodes  $D_1$ ,  $D_2$ , and  $D_3$ . Similarly, switched-inductor hybrid unit number 2 consists of inductors  $L_3$  and  $L_4$  and the fast-switching diodes are  $D_4$ ,  $D_5$ , and  $D_6$ . Switched-inductor hybrid unit number 1 and 2 are interleaved by the help of MOSFET's -1 and -2, respectively. Diodes  $D_7$  and  $D_8$ , and  $D_9$ , are used as reverse current blocking diodes. Whereas  $C_1$  is a filter capacitor and  $R_L$  is the load resistance. It is assumed the inductors  $L_1$ ,  $L_2$ ,  $L_3$ , and  $L_4$ , have identical symmetry and value.

### 2.1 Generation of Control Sequence

Fig. 2(a) displays the control scheme where a function generator generates a triangular voltage waveform,  $v_T$ .

This triangular voltage is fed to the inverting terminal of operational amplifier (op-amp) 1 and to the non-inverting terminal of op-amp 2. Both op-amps are being used as comparators. The non-inverting terminal of op-amp 1 is provided with the reference voltage  $v_{REF}$ . The inverting terminal of op-amp 2 is provided with a modified reference voltage  $v_{REF}'$ , given as

$$v_{REF}' = V_{CC} - v_{REF} \quad (1)$$

Where  $V_{CC}$  is the peak voltage of triangular voltage waveform as shown in Fig. 2(b). The outputs of op-amps -1 and -2 are connected to separate commercial MOSFET drivers such as model IR2110 manufactured by International Rectifier™. The output voltage signals of individual drivers, i.e.,  $v_{G1}$  and  $v_{G2}$ , drive the gate-terminals of MOSFET-1 and -2, respectively.

### 2.2 Working of a Switched-Inductor Hybrid Unit

Depicted in Fig. 1, the working of a switch-inductor hybrid unit will be presented. For example, as MOSFET-1 is switched ON inductor  $L_1$  is energized through  $D_3$ , and  $L_2$  is energized through  $D_2$ . The voltage polarity appearing across inductors  $L_1$  and  $L_2$  are the same as of the fuel cell voltage,  $V_{DC}$ , under such condition the inductors appear in parallel configuration. If  $i_{L1}$  is the current in  $L_1$ , and  $i_{L2}$  is the current in  $L_2$ , since the inductors are in symmetry, then

$$i_{L1} = i_{L2} = \frac{V_{DC}}{L_1} (t_2 - t_1) \quad (2)$$

where  $t_1$  and  $t_2$  represent the starting and ending time of mode-1, respectively.

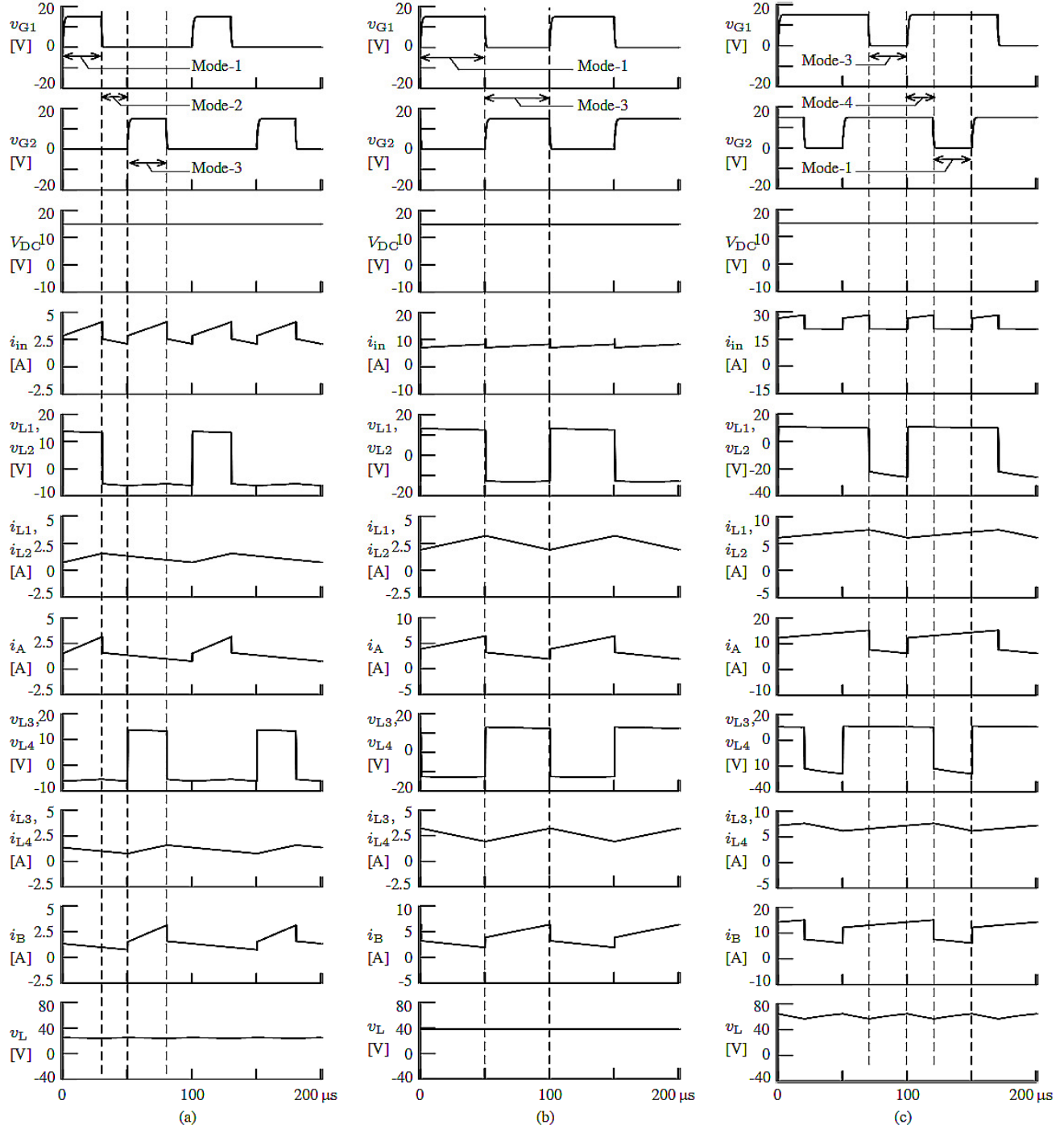


Fig. 3 Simulated response of the proposed switched-inductor hybrid DC converter (a) for  $D=0.3$  (b) for  $D=0.5$  (c) for  $D=0.7$

However, when MOSFET-1 is switched OFF, the voltage polarity of inductors  $L_1$  and  $L_2$  reverses in direction. The reverse polarity across inductors  $L_1$  and  $L_2$  reverse bias diodes  $D_2$  and  $D_3$ , respectively. With  $D_2$  and  $D_3$  reversed biased, the current flowing in  $L_1$  flows through  $D_1$  and then through  $L_2$ . Therefore, inductors  $L_1$  and  $L_2$  become a series circuit. Assuming a zero voltage drop across a conducting diode, the voltage appearing across the load,  $v_L$ , is expressed as,

$$v_L = V_{DC} + v_{L1} + v_{L2} \quad (3)$$

### 2.3 Working of the proposed circuit

With reference to Fig. 1, the steady state analysis of the proposed interleaved switched-inductor hybrid DC converter is described in the following four modes. It should be noted that both MOSFETs have same turn-on and turn-off times.

Mode-1: Fig. 3(a) demonstrates the instant when MOSFET-1 is turned ON and MOSFET-2 is OFF. Inductors  $L_1$  and  $L_2$ , of

switched-inductor hybrid unit 1, appear in parallel configuration and are charged with a constant voltage. For the switched-inductor hybrid unit 2, since MOSFET-2 is turned, the inductors  $L_3$  and  $L_4$  appear in series configuration. The voltage stress observed at source-terminals of MOSFET-2 is essentially equal to the output load voltage.

Mode-2: Fig. 3(b) demonstrates the instant when both MOSFET-1 and -2 are turned off. The inductors of switched-inductor hybrid unit 1 are now in series configuration. Similarly, the inductors of switched-inductor hybrid unit 2 are now also in series configuration. In this mode inductors of both switched-inductor

Parameter	D = 0.3		D = 0.5		D = 0.7		Unit
	Min.	Max.	Min.	Max.	Min.	Max.	
$i_{IN}$	2.1	4.12	7	10.27	20.37	28.13	A
$v_{L1}, v_{L2}, v_{L3}, v_{L4}$	-6.2	13.78	-13	13	-26.12	10.7	V
$i_{L1}, i_{L2}, i_{L3}, i_{L4}$	0.75	1.56	1.93	3.24	6.1	7.54	A
$v_{D2}, v_{D3}, v_{D5}, v_{D6}$	-5.33	0.86	-12.13	0.86	-25.24	0.91	V
$v_{MOS1}, v_{MOS2}$	0.43	26.51	1.1	40	3.38	66.34	V
$i_{MOS1}, i_{MOS2}$	-0.1	3.13	-0.1	6.4	-0.1	15.08	A
$v_L$	23.4	24.8	37.5	38.4	56.44	64.58	V
$i_L$	1.56	1.65	2.5	2.5	3.76	4.3	A
$i_{C1}$	-0.6	1	0.8	2.56	-4.3	3.85	A

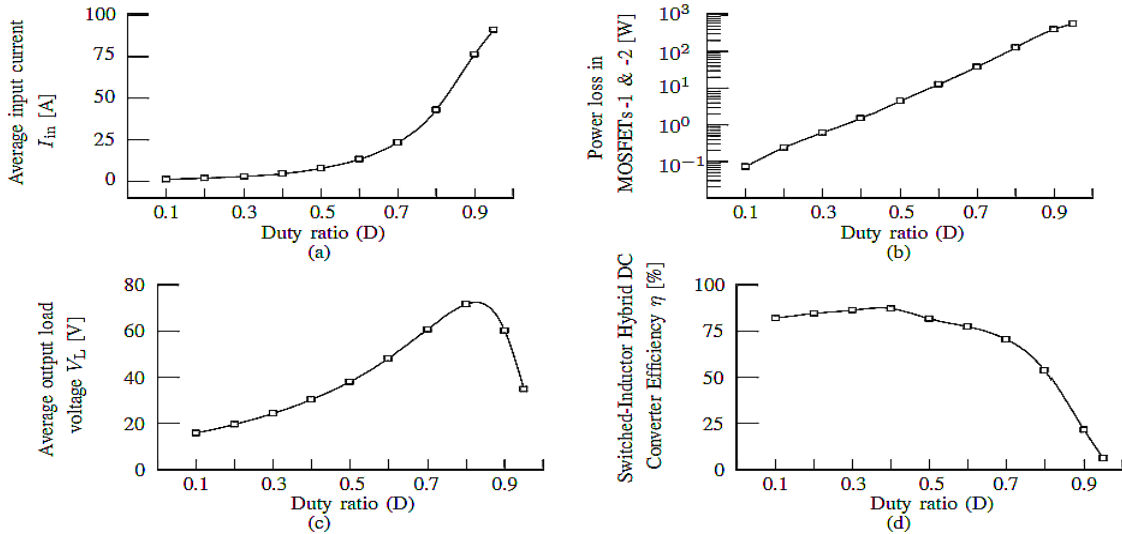


Fig. 4 Simulated performance of various parameters of the proposed switch-inductor hybrid DC converter circuit as  $D$  ranges from 0 to 1 (a) shows the average input current (b) shows the power dissipation in MOSFETs -1 and -2 (c) shows the average output load voltage (d) shows the efficiency

hybrid units are essentially discharging via the load. The voltage stress observed at source-terminals of both MOSFETs is essentially equal to the output load voltage.

Mode-3: Fig. 3(c) demonstrates the instant when MOSFET-1 is turned off and MOSFET-2 is on. For the switched-inductor hybrid unit 1, the inductors  $L_1$  and  $L_2$  appear in series configuration. The voltage stress observed at source-terminal of MOSFET-1 is essentially equal to the output load voltage. Inductors  $L_3$  and  $L_4$ , of switched-inductor hybrid unit 2, appear in parallel configuration and are charged with a constant voltage, i.e.,  $V_{DC}$ .

Mode-4: Fig. 3(d) demonstrates the instant when MOSFETs-1 and -2 are both turned on. In this mode, all inductors of switched-inductor hybrid unit 1 and 2 appear in parallel configuration, and are in charging state. During this mode-4, since the diodes  $D_7$ ,  $D_8$ , and  $D_9$ , are reversed biased, therefore, the capacitor  $C_1$  discharges through the load resistor.

Table 2. Proposed Interleaved Switched-Inductor Hybrid Dc Boost Converter Maximum And Minimum Voltage And Current Values For Various Kept Equal To 0.3, 0.5, And 0.7

### 3. SIMULATED RESULTS

The proposed interleaved switched-inductor hybrid DC converter circuit is simulated using Proteus Virtual System Modeling (VSM)TM software from Labcenter Electronics™. Proteus VSMTM had been selected as it routines mixed mode SPICE1 circuit simulations. SPICE abbreviates for Simulation Program with Integrated Circuit Emphasis.

With reference to Fig. 1, the circuit parameters are set as follows; input voltage  $V_{DC}=15V$ , inductors  $L_1$ ,  $L_2$ ,  $L_3$ , and  $L_4 = 500\mu H$  each, capacitor  $C_1 = 10\mu F$  (polarized capacitor), diodes  $D_1$  to  $D_9$  are fast switching diodes (e.g., model number SUF15J), both MOSFETs -1 and -2 were IRFP460, whereas  $R_L=15\Omega$ . These circuit parameter were so selected that the converter operates in continuous conduction mode (CCM).

The control signals for driving the MOSFETs-1 and -2 as shown in Fig. 2, were generated by setting the frequency of the triangular voltage waveform to 10kHz, and a peak voltage,  $V_{CC} = 10V$ . As indicated in the figure, the duty cycle is variable from 0 to 1. The reference voltage,  $v_{REF}$ , was variable from 0 to 10 V.

**1) Results for  $D = 0.3$  ( $D < 0.5$ ):** Fig. 4(a) displays the voltage and current waveforms of the proposed interleaved switched-inductor hybrid DC boost converter for  $D = 0.3$ . Only mode-1, -2, and -3, are present whereas mode-4 is absent. For an input voltage of 15V, the minimum and maximum voltage and current values of various circuit components are summarized in Table I. Such a summary may also be useful in determining thermal

properties of electronic components in the circuit. The observed average DC output voltage is approximately equal to 24 V.

**2) Results for  $D = 0.5$ :** Fig. 4(b) displays the voltage and current waveforms of the proposed interleaved switched-inductor hybrid DC boost converter for  $D = 0.5$ . Only mode-1 and -3, are present whereas mode-2, and -4 are absent. For an input voltage of 15V, the minimum and maximum voltage and current values of various circuit components are summarized in Table I. The observed average DC output voltage is approximately equal to 38V.

**3) Results for  $D = 0.7$  ( $D > 0.5$ ):** The simulated voltage and current waveforms of the interleaved switched-inductor hybrid DC boost converter for  $D = 0.7$ , are presented in Fig. 4(c). Only mode-1, -3, and -4 are present whereas mode-2 is absent. For an input voltage of 15V, the minimum and maximum voltage and current values of various circuit components are summarized in Table I. The observed average DC output voltage is approximately equal to 60V, whereas the peak-to-peak output ripple voltage is observed to be 8V.

#### 4. DISCUSSION

A careful examination of Fig. 4 indicates that for a given value of D, the proposed interleaved switched-inductor hybrid DC boost converter operates only in three modes of operation. When D is kept less than 0.5, e.g., as in Fig. 4(a) (mode-1, -2, and -3 are present whereas mode-4 is absent), in this condition ( $D < 0.5$ ), the capacitor C1 charges in mode -1 and -3 while it discharges in mode -2. However, the condition  $D = 0.5$  is an exception where the proposed converter operates only in mode-1 and -3. When  $D = 0.5$ , as in Fig. 4(b), the capacitor C1 charges and discharges in the same mode. Whereas, for  $D > 0.5$ , e.g., in Fig. 4(c), only mode-1, -3, and -4 are observed. In this condition ( $D > 0.5$ ), the capacitor C1 charges in mode -1 and -3 while it discharges in mode -4.

Observations of average input current, power-dissipation in MOSFET-1 (also applicable to MOSFET-2), output load voltage, and efficiency of the proposed converter, as a function of D are presented in Fig. 5. Fig. 5(a) displays that the input current increases exponentially as D increases. For a value of D beyond 0.7 the input current becomes excessive large. This can be explained as follows. The input current is consumed only at the time when MOSFETs-1 or -2 are switched on (at their respective time), for values of D less than 0.5, since this the switching time of MOSFETs is small as compared to turn-off time therefore the input current is consumed less. However, as D increase beyond 0.5, the MOSFET turn-on time exceeds the turn off time and thereby, causing more current to be consumed from the source. Fig. 5(b) indicates the consequences of increasing the input current is faced by the MOSFETs in the form of large dissipation loss and large stress voltage (also Table I). Fig. 5(c) suggests that the load voltage of proposed interleaved switched-inductor hybrid DC boost converter may be considered linear for D ranging from 0 to 0.6. An interesting observation is regarding the efficiency of the proposed converter as shown in Fig. 5(d). The simulated results indicate that the proposed converter shows highest efficiency of 85 % for  $D = 0.4$ .

#### 5. CONCLUSION

The main contribution of this research is to put forward a model of the interleaved switched-inductor hybrid DC converter. Results have shown that the proposed interleaved switched-inductor hybrid DC converter shows stability for duty ratio ranging from 0.1 to 0.7 . The proposed converter can operate in

four-modes with the help of interleaved switching technique. The main advantage of the proposed converter is the lower stored energy in the magnetic elements, which leads to less weight, size and cost reduction for the inductors. As more switched-inductor hybrid units are interleaved the filter capacitor size can be reduced. Simulated results of the proposed converter substantiate the performance of the design system.

#### 6. REFERENCES

- [1] W. Li, Y. Zhao, Y. Deng, and X. He, "Interleaved converter with voltage multiplier cell for high step-up and high-efficiency conversion," *IEEE Trans. Power Electron.*, Vol. 25, No. 9, Sept. 2010, pp. 2397–2408.
- [2] Muhammad H. Rashid, "Power Electronics: Circuits, Devices and Applications," *Prentice Hall*, 3ed., Aug. 14, 2003, pp.176–177.
- [3] M. Prudente, L. L. Pfitscher, G. Emmendoerfer, E. F. Romaneli, and R. Gules "Voltage multiplier cells applied to non-isolated DCDC converters," *IEEE Trans. Power Electron.*, Vol. 23, No. 2, March 2008, pp. 871–887.
- [4] Q. Zhao, and F. C. Lee "High-efficiency, high step-up dc-dc converters," *IEEE Trans. Power Electron.*, Vol. 18, No. 1, Jan. 2003, pp. 65–73.
- [5] W. Li, and X. He, "Review of nonisolated high-step-up dc/dc converters in photovoltaic grid-connected applications," *IEEE Trans. Ind. Electron.*, Vol. 58, No. 4, April 2011, pp. 1239–1250.
- [6] P. Lee, Y. Lee, D. Cheng, and X. Liu, "Steady-state analysis of an interleaved boost converter with coupled inductors, *IEEE Trans. Ind. Electron.*, Vol. 47, No. 4, Aug. 2000, pp. 787–795.
- [7] G. Calderon-Lopez, A. J. Forsyth, and D. R. Nuttall, "Design and performance evaluation of a 10-kW interleaved boost converter for a fuel cell electric vehicle," *Proc. IEEE Power Electron. Motion Control Conf.*, Aug. 2006, Vol. 2, pp. 1-5.
- [8] P. Thounthong, and S. Pierfederici "A new control law based on the differential flatness principle for multiphase interleaved DC-DC converter," *IEEE Trans. Circuits Syst-II: Express Briefs*, Vol. 57, No. 11, Nov. 2010. pp. 903–907.
- [9] J. Lee, Y. Jeong, and B.Han "An isolated dc/dc converter using high-frequency unregulated LLC resonant converter for fuel cell applications," *IEEE Trans. Ind. Electron.*, Vol. 58, No. 7, July 2011, pp. 2926–2934.
- [10] B. Axelrod, Y. Berkovich, and A. Ioinovici, "Switched-capacitor/switched-inductor structures for getting transformerless hybrid DC-DC PWM converters," *IEEE Trans. Circuits Syst-I: Reg. Papers*, vol. 55, no. 2, pp. 687–696, Mar. 2008.
- [11] L. S. Yang, T. Liang, and J. Chen, "Transformerless DC-DC converters with High step-up voltage gain," *IEEE Trans. Ind. Electron.*, Vol. 56, no. 8, Aug. 2009. pp. 3144–3152.

\*\*\*\*

# Cellular Communication Using Single band Microstrip Patch Antenna Model

Engr. Omer Iqbal, Engr. Abid Hussain Chohan,  
Engr. Farhan Fareed Khan

Dept. of Electrical & Electronics Engineering  
NFC Institute of Engineering & Technological Training Multan, Pakistan

## Abstract

The cellular industry was brought into being about 25 years from today, presently, producing \$400 billion in annual revenues, intensifying its growth to the highest scale, with superlatively 4.1 billion subscribers from all around the world. Moving back to the 1980's, heavily built cellular handsets that were large and awkward to carry or move, were soon replaced by advancements in VLSI technology which empowered size reduction by using microprocessors chips.

One of the techniques for decreasing the handset size is the usage of compact antennas. A MPA (Microstrip Patch Antenna) made up of a plane called "ground plane" at one side of a patch. The other side of the patch contains dielectric substrate. This type of antenna mostly used in applications like mobile phones, satellite communications and etc. because of its beneficial factors, such as less weight / volume, less construction costs, capability to assimilate with MICs (microwave integrated circuits) and less profile planar configuration. This research study is based on a compact microstrip patch antenna which is radiated at 1.9 GHz for use in cellular phones and established results present a practical antenna model for incorporation in mobile phone.

## I. INTRODUCTION

In its original structure, a MPA is basically made up of dielectric substrate which have the plane called "ground plane" at one side and radiating patch on the other side as presented in Figure 1. Radiating patch is usually made up of gold or copper which is conducting in nature, is capable to pick any desired shape. The feed lines are engraved by using a photomechanical process on the dielectric substrate. To reduce the complexity of exploration and performance prediction, the patch is kept circular, square, rectangle, triangular, and ovate or more collective shapes as presented in Figure 2. The rectangular shape patch length "L" is taken in the range of  $0.333\lambda_0 < L < 0.500\lambda_0$ , where, the  $\lambda_0$  is "free space wavelength". The patch on MPA is chosen to be narrow such that  $t \ll \lambda_0$  where, "t" represents the thickness of patch. Height of dielectric substrate "h" is taken in the range of  $0.0030\lambda_0 \leq h \leq 0.050\lambda_0$ . The  $\epsilon_r$  called "constant of the dielectric substrate" ( $\epsilon_r$ ) is taken to be in the range of  $2.20 \leq \epsilon_r \leq 12.0$  [1].

MPA radiates predominantly due to the marginal area between edge of the patch and ground plane. A dielectric substrate with a greater bandwidth and low dielectric

incessant is advantageous for advanced efficiency but this requires larger antenna size, thus higher dielectric constant for designing the compact antenna must be used [1].

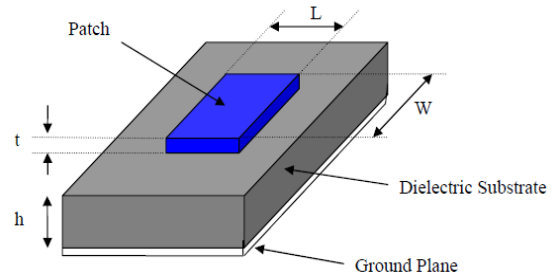


Figure 1 MPA (Microstrip Patch Antenna) structure [1].

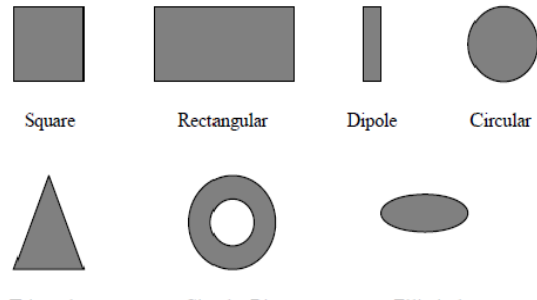


Figure 2 Microstrip patch element shapes [1].

## II. DESIGN SPECIFICATIONS

The most basic elements for design of above said rectangular MPA are as follow:

**Operational Frequency ( $f_o$ ):** It is designed to be functioning in the range of frequency of PCS (1850-1990 MHz) and the resonant frequency of 1.90 GHz [2].

**Dielectric constant of substrate ( $\epsilon_r$ ):** Silicon is dielectric material and is used in this antenna model.  $\epsilon_r$  of 11.90 is selected for this model. The higher  $\epsilon_r$  is selected because of reduction in size [1].

**Dielectric substrate height (h):** The dielectric substrate height chosen in this design is 1.50 mm [1].

## III. DESIGN PROCEDURE

The model used for this antenna design is transmission line [3-10].

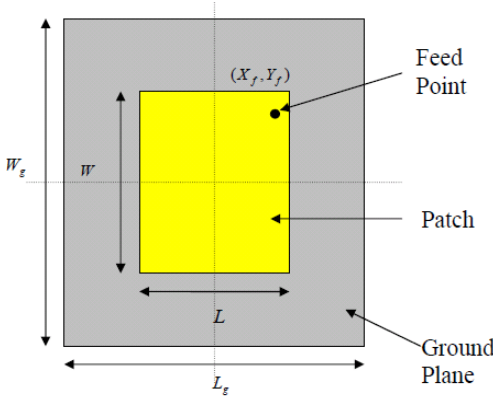


Figure 3 Top view of MPA.

**Width Computation (W):** The relation given below is used to calculate width of MPA.

$$W = \frac{c}{2 f_0 \sqrt{\frac{\epsilon_r + 1}{2}}} \quad \dots \dots \quad (1)$$

Putting the values of constant in the above equation  $c = 3 \times 10^8 \text{ m/s}$ ,  $\epsilon_r = 11.90$  and  $f_0 = 1.90 \times 10^9 \text{ Hz}$ .

$$W = 31.10 \times 10^{-3} \text{ m or } 31.10 \text{ mm.}$$

**Effective dielectric constant computation ( $\epsilon_{r,eff}$ ):** The relation given below is used to calculate the effective dielectric constant as:

$$\epsilon_{r,eff} = \frac{\epsilon_r + 1}{2} + \frac{\epsilon_r - 1}{2} \left[ 1 + 12 \frac{h}{W} \right]^{-1/2} \quad \dots \dots \quad (2)$$

By putting,  $\epsilon_r = 11.90$ ,  $W = 31.10 \times 10^{-3} \text{ m or } 31.10 \text{ mm}$  and  $h = 1.50 \times 10^{-3} \text{ m or } 1.50 \text{ mm}$  we get:

$$\epsilon_{r,eff} = 10.78710.$$

**Effective length computation ( $L_{eff}$ ):**  $L_{eff}$  of the proposed antenna is computed by using the relation given below:

$$L_{eff} = \frac{c}{2 f_0 \sqrt{\epsilon_{r,eff}}} \quad \dots \dots \quad (3)$$

Putting  $\epsilon_{r,eff} = 10.78710$ ,  $c = 3 \times 10^8 \text{ m/s}$  and  $f_0 = 1.90 \times 10^9 \text{ Hz}$ , we get:

$$L_{eff} = 24 \times 10^{-3} \text{ m or } 24 \text{ mm.}$$

**Computation of length extension ( $\Delta L$ ):** Equation used to calculate the extension length is given below:

$$\Delta L = 0.412h \frac{(\epsilon_{r,eff} + 0.3)(\frac{W}{h} + 0.264)}{(\epsilon_{r,eff} - 0.258)(\frac{W}{h} + 0.8)} \quad \dots \dots \quad (4)$$

Substituting  $\epsilon_{r,eff} = 10.78710$ ,  $W = 31.10 \times 10^{-3} \text{ m or } 31.10 \text{ mm}$  and  $h = 1.50 \times 10^{-3} \text{ m or } 1.50 \text{ mm}$  we get:

$$\Delta L = 6.34550 \times 10^{-4} \text{ m or } 6.34550 \text{ mm.}$$

**Actual length of patch computation ( $L$ ):** The  $L$  is obtained by following relation given below:

$$L = L_{eff} + 2\Delta L \quad \dots \dots \quad (5)$$

By putting  $L_{eff} = 24 \times 10^{-3} \text{ m or } 24.0 \text{ mm}$  and  $\Delta L = 6.34550 \times 10^{-4} \text{ m or } 6.34550 \text{ mm}$  we get:

$$L = 22.80 \times 10^{-3} \text{ m or } 22.80 \text{ mm.}$$

**Ground plane dimensions computation ( $L_g$  and  $W_g$ ):**

The TL model is only relevant to infinite ground planes, but in case of practical deliberation, there must be a finite ground plane. It has been proved that, if the ground plane size is larger than six times the patch dimensions, the results are similar for both finite and infinite ground planes. Ground plane size / dimension for this antenna design would be as:

$$L_g = 6h + L \quad \dots \dots \quad (6)$$

$$= 6(1.5) + 22.8 = 31.8 \text{ mm}$$

$$W_g = 6h + W \quad \dots \dots \quad (7)$$

$$= 6(1.5) + 31.1 = 40.1 \text{ mm}$$

**Feed point location determination ( $X_f$ ,  $Y_f$ ):** In this antenna design / model coaxial probe type is used. As presenting in Figure 3, the center of the patch is regarded as derivation and feed spot is specified by coordinates  $(X_f, Y_f)$  from the derivation. The feed point on the patch must be at that spot, where impedance (input impedance) is  $50 \Omega$  at resonant frequency. Therefore, a method called trial and error method is used to determine feed point and feed point is chosen where the R.L (return loss) is proved to be negative. A point is found there beside the patch, where R.L is at the lowest degree. Therefore,  $Y_f$  will be zero in this design, and  $X_f$  will be assorted to search the optimum feed point.

#### IV. SIMULATION SETUP AND RESULT

The software which is put to use to conjure up the microstrip patch antenna is FEKO software. It is complete wave electromagnetic simulator which analyzes different shapes of multilayer structure. It is used to plot and calculate current distributions,  $S_{11}$  parameters, VSWR and radiation patterns also. Putting it to simplicity, width and length of the ground and patch rounded off to the following values as:  $L = 22 \times 10^{-3} \text{ m}$ ,  $W = 31 \times 10^{-3} \text{ m}$ ,  $L_g = 31 \times 10^{-3} \text{ m}$  and  $W_g = 40 \times 10^{-3} \text{ m}$ .

##### A. Calculation of Antenna bandwidth and Return Loss:

For feeding, “co-axial probe type feed” is used. It is designed to a radius of  $0.50 \times 10^{-3} \text{ m}$ .  $1.70 \times 10^9$  to  $2.1 \times 10^9 \text{ Hz}$  frequency range is selected. Approximately 401 points are selected to determine the accurate / precise results.

No.	Feed Location ( $X_f, Y_f$ ) (mm)	Center Frequency (GHz)	Return Loss (RL) (dB)	Bandwidth (RL > -9.5dB) (MHz)
1	(1,0)	1.9153	-1.1384	-
2	(2,0)	1.9147	-4.5967	-
3	(3,0)	1.9127	-10.9602	9.97
4	(3.25,0)	1.9133	-13.3696	15.32
5	(3.5,0)	1.9127	-16.6242	18.84
6	(3.75,0)	1.9127	-21.2769	21.43
7	(4,0)	1.9120	-31.3585	23.28
8	(4.25,0)	1.9127	-28.5068	24.40
9	(4.5,0)	1.9127	-21.2952	25.16
10	(4.75,0)	1.9120	-17.6845	25.23
11	(5,0)	1.9120	-15.0623	24.30
12	(6,0)	1.9087	-10.2221	13.57
13	(7,0)	1.9087	-7.7754	-
14	(8,0)	1.9087	-6.3367	-
15	(9,0)	1.9073	-5.5806	-
16	(10,0)	1.9073	-5.0228	-

Table 1 Center frequency, bandwidth and return loss calculation for different feed location.

Bandwidth will be accessed from RL plot, whereas, center frequency is chosen where the RL is least. The bandwidth is from the category of frequencies above which the Return loss is superior to -9.50 dB (where -9.50 dB corresponds to a VSWR of 2). The optimum feed point according to the table 1 is found at ( $X_f, Y_f$ ) = (4, 0) where RL -31.3585 dB is achieved. The antenna bandwidth at this feed point is calculated (shown in Figure 4) to be around 23.28 MHz and the center frequency 1.9120 GHz is achieved. This frequency is near to the required design frequency (1.9 GHz). It is also noted that the maximum bandwidth is obtained at ( $X_f, Y_f$ ) = (4.75, 0).

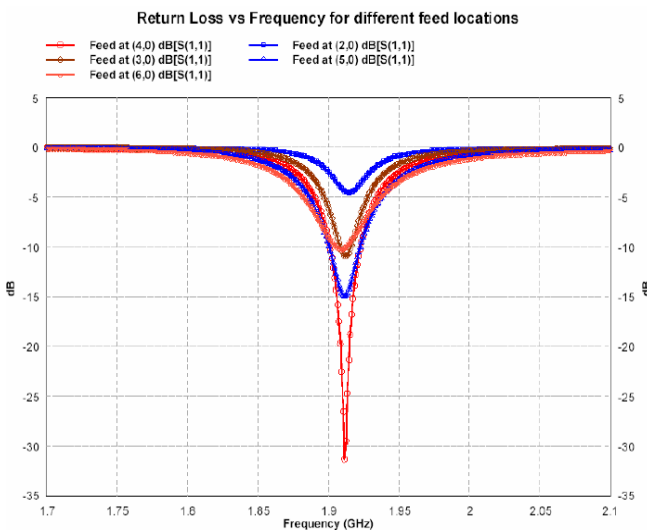


Figure 4 Return losses at different feed locations.

### B. Plots of Radiation Pattern:

Elevation pattern for  $\Phi = 90$ ,  $\Phi = 0$  is important because MPA radiates to its patch. Figure 5 below presents antenna gain at  $1.912 \times 10^9$  Hz for  $\Phi = 90$ ,  $\Phi = 0$  degrees. The antenna's greatest gain is obtained in broadside direction and this gain is measured to be 1.87 dB both for  $\Phi = 90$  and  $\Phi = 0$  degrees. The back lobe radiation is measured to be -5.30 dB for above plot which is very small. It also reduce amount of electromagnetic radiations moving towards user's head and this is an additional benefit of using this antenna in cellular phone. The three-Dimensional plots for this proposed antenna are displayed in Figure 6 at different angles.

### C. Other Calculated Parameters:

Some other calculated parameters, thus named, 3-dB beam width for the antenna at 1.9120 GHz, gain, antenna efficiency, and directivity are (106.85, 110.24), 1.8717 dB, 42.77%, and 5.56 dB respectively.

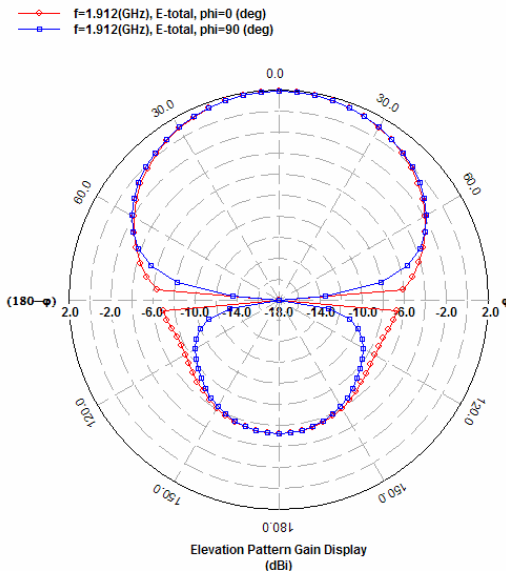


Figure 5 Elevation Pattern of proposed antenna for  $\Phi = 90$ ,  $\Phi = 0$  degree's.

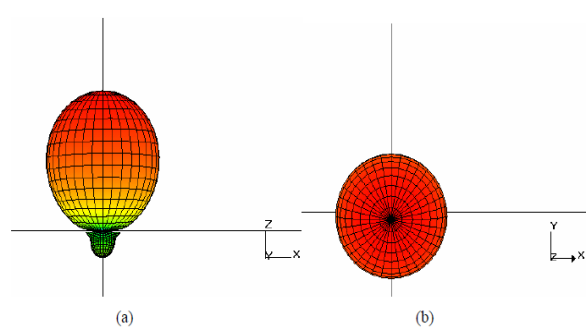


Figure 6 (a) 3-diemnsional radiation pattern in XZ plane along Y-axis.  
(b) 3-diemnsional radiation pattern in XY plane along Z axis.

## V. CONCLUSION

The ground plane measurements for patch antenna is devised to be 31 mm by 40 mm, while the patch measurements stand at 22 mm by 31 mm, precisely, the antenna is shrink well in accordance with the adjustment space in a typical cellular phone, measuring about 14.5 cm by 4.5 cm.

For compulsory antenna orientation, radiation pattern plots are obtained. The decreased back lobe radiation saw its remarkable invention, which helps in diminishing electromagnetic energy amount radiated towards the head of the phone holder. An adequate bandwidth of 23.28 MHz is obtained in this proposed antenna design, which is also beneficial for cellular gadgets in the PCS variety since 30 KHz channels are used by GSM and TDMA systems.

Aims have been set to encompass this concept in future to a multiband design. Engineers have foreseen the advanced future of cellular phones, and one of the features would include a single handset to provide a large number of applications. Indoors, the cell phone / handset would function in identical frequency range of a cordless phone, and attached to local telephone exchange. When outdoor, handset would connect to mobile networks, and from a distance, or far from home; the handset would connect via satellite to arrange signals to the user.

## VI. References

- [1] Balanis, C.A. *Antenna Theory: Analysis and Design*, John Wiley & Sons, Inc, 1997.
- [2] Rappaport, Theodore S., *Wireless Communications: Principles and Practice*, Prentice Hall Communications Engineering and Emerging Technologies Series, 1999.
- [3] Kumar, G. and Ray, K.P., *Broadband Microstrip Antennas*, Artech House, Inc, 2003.
- [4] Garg, R., Bhartia, P., Bahl, I., Ittipiboon, A., *Microstrip Antenna Design Handbook*, Artech House, Inc, 2001.
- [5] Qian, Y., et al., "A Microstrip Patch Antenna using novel photonic bandgap structures", *Microwave J.*, Vol 42, Jan 1999, pp. 66-76.
- [6] Hammerstad, E.O., "Equations for Microstrip Circuit Design," Proc. Fifth European Microwave Conf., pp. 268-272, September 1975.
- [7] James, J.R. and Hall, P.S., *Handbook of Microstrip Antennas*, Vols 1 and 2, Peter Peregrinus, London, UK, 1989.
- [8] Bahl, I.J. and Bhartia, P., *Microstrip Antennas*, Artech House, Dedham, MA, 1980.
- [9] Richards, W.F., *Microstrip Antennas*, Chapter 10 in *Antenna Handbook: Theory Applications and Design* (Y.T. Lo and S.W. Lee, eds.), Van Nostrand Reinhold Co., New York, 1988.
- [10] Newman, E.H. and Tulyathan, P., "Analysis of Microstrip Antennas Using Moment Methods," *IEEE Trans. Antennas Propag.*, Vol. AP-29, No. 1, pp. 47-53, January 1981.
- [11] [www.feko.info](http://www.feko.info).

## Quotations

- Everything that irritates us about others can lead us to an understanding of ourselves. Carl Jung
- The mind is its own place, and is itself, can make a Heaven of Hell, a Hell of Heaven John Milton
- The object of all psychology is to give us a totally different idea of the things we know best. Paul Valey
- Judgment is more than skill. It sets forth on intellectual seas beyond the shores of hard indisputable factual information. Kingman Brester
- I have always thought the actions of men the best interpreters of their thoughts to old age. Friedrich Wilhelm Nietzsche
- Iron rusts from disuse, stagnant water loses its purity, and in cold weather becomes frozen; ever so does inaction sap the vigors of the mind. Leonardo da Vinci
- Everyman who expresses a honest thought is a soldier in the army of intellectual liberty. Robert G. Ingersoll
- Learning without thought is labor lost; thought without learning is perilous. Walter Lippmann
- One must learn to think well before learning to think afterwards it proves too difficult. Anatole France
- When he who hears does not know what he who speaks means, and when he who speaks does not know what he himself means – that is philosophy. Voltaire
- The first test of a truly great man is his humility. John Ruskin
- Prejudice is the child of ignorance. William Hazlitt
- The nobler a man, the harder it is for him to suspect inferiority in others. Cicero

# Performance Analysis of 3-D DWT, 3-D DFT, 3-D DCT, 3-D DHT for Medical Image Compression

Zain Ul Abidin

Department of Electrical Engineering,  
University of Engineering & Technology Taxila – Pakistan

Gulistan Raja

Department of Electrical Engineering,  
University of Engineering & Technology Taxila – Pakistan

Muhammad Haroon Yousaf

Department of Computer Engineering  
University of Engineering & Technology Taxila – Pakistan

## Abstract

Medical images have been widely in use for the diagnosis of different diseases. To deal with the huge storage requirements for these images, medical images compression has been one of the promising areas of research in last decade. This paper aims to analyze the performance of 3-D discrete wavelet transform (DWT), 3-D discrete cosine transform (DCT), 3-D discrete Hartley transform (DHT) and 3-D discrete Fourier transform (DFT) for the compression of medical images. Various MRI images and x-ray angiograms have been used for the implementation of these transforms. Medical images are divided into  $8 \times 8 \times M$  block sizes, where  $M$  is the number of slices. 3-D transformed output coefficients are then quantized and encoded. Proposed research work evaluates the performance of these transforms on parameters like peak signal to noise ratio (PSNR), structural similarity index matrices (SSIM), bit error rate (BER) and Compression ratio (CR). Experimentation results have shown that for MRI images Daubechies wavelets gave highest performance than biorthogonal and Symlet wavelets; for Angiograms biorthogonal wavelets is found to be the most suitable. Experimentation results also indicates that 3-D DHT yields best PSNR values for MRI images and 3-D DCT is most suitable transform for the compression of angiographic images.

**Key Words**—Medical Image Compression, Discrete Cosine transform, Discrete Fourier transform, Discrete Hartley transform, Discrete Wavelet transform.

## I. INTRODUCTION

With the ever growing need of bandwidth and its scarcity, there is always a need to store and transmit information in a manner which requires minimum storage space and fast transmission rate. These days, medical images are one of the important sources of information used to diagnose patient ailment. For the patients residing at far locations these images are transferred to doctors through internet to diagnose and treat patient. Medical image compression has gained much attention as it allows fast transmission of medical images and requires low storage space while maintaining relevant diagnostic information. Different compression techniques are used for this purpose. These compression techniques can be categorized into two types .Lossy compression and lossless compression. Lossless compression techniques are usually used for compression of medical images. As the name indicates no information is lost in case of lossless compression. For medical images lossy compression is tolerable if it does not affect the diagnostic results [1].

3-D medical image compression is very important because most of the diagnosis carried out uses MRI, CT, PET, angiogram and other modalities. These modalities generate multiple slices of a single organ under examination [2]. Progressive variation of object in multiple 2-D slices placed one after another is visualized as 3-D imaging or it is the time sequence of slice images of dynamic object [3].

General block diagrams of compression and decompression are shown in fig. 1 and fig. 2 respectively.

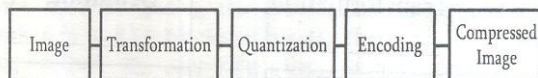


Fig. 1. Compression of an Image [4]

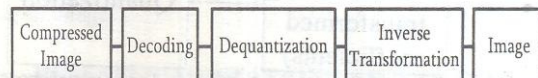


Fig. 2. Decompression of an Image[4]

To achieve compression input image data is first de-correlated by applying transformation. This transformed data is quantized and encoding is performed. Various linear transformation techniques have been developed, each transform has its benefits and draw backs. Human eyes are less sensitive to the higher frequencies hence higher components can be neglected without any apparent loss [5]. Medical image compression is more critical than compression for any other image. To avoid any unwanted situation special attention must be provided in this regard. Suitable choice of transform is very mandatory to achieve the desired goals i.e. High compression ratio and better PSNR maintaining correct diagnostic information.

For image compression in JPEG, DCT is used. Recently for image compression wavelet based transforms are used because even at higher compression rates the image quality is excellent [6]. Fortunately many wavelet filters exists each having different characteristics, for good coding performance selection of correct wavelet filter is very important [7].

This research work targets the implementation of 3-D DCT, 3-D DHT, 3-D DFT, 3-D Daubechies wavelet transform, 3-D Symlet transform and 3-D biorthogonal transform in order to find the most suitable transform and investigate the behavior of different wavelet filters for compression of different medical images. Transforms are applied on different medical images like MRI of abdomen, kidney, cardiac, brain, angiograms of liver and chest for compression purpose. Their performances are

compared on the basis of performance parameters like PSNR, SSIM, Bit rate and compression ratio[8].

## II. PROPOSED METHODOLOGY

The block diagram of the implemented compression method is given in fig.3

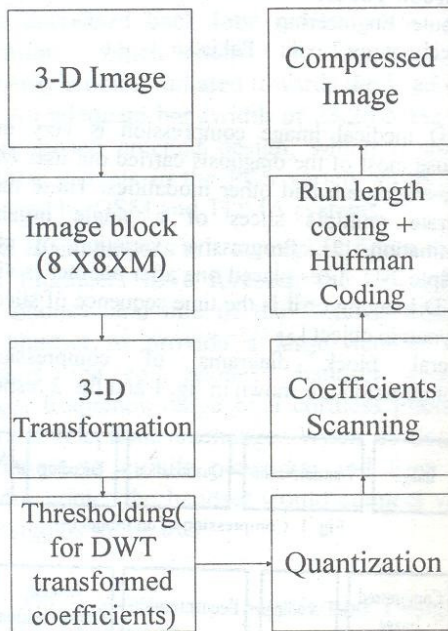


Fig. 3. Block diagram of proposed compression model

In the first step the 3-D medical image is split into 3-D data block of 8X8XM sizes. Number of slices considered are M=2, 4, 8 and 16. 3-D transformation is applied to block data to remove inter slice redundancy. Each 3-D transform is explained in the subsequent sections.

### A. 3-D DHT:

For Hartley transform,3-D DHT and 3-D inverse DHT are defined as given in equation (1) and (2) respectively [9].

$$P(\alpha, \beta, \gamma) =$$

$$\sum_{X=0}^{N_1-1} \sum_{Y=0}^{N_2-1} \sum_{Z=0}^{N_3-1} p(X, Y, Z) \text{cas}\left(\frac{2\pi X\alpha}{N_1} + \frac{2\pi Y\beta}{N_2} + \frac{2\pi Z\gamma}{N_3}\right) \dots (1)$$

$$p(X, Y, Z) =$$

$$\frac{1}{N_1 N_2 N_3} \sum_{\alpha=0}^{N_1-1} \sum_{\beta=0}^{N_2-1} \sum_{\gamma=0}^{N_3-1} P(\alpha, \beta, \gamma) \text{cas}\left(\frac{2\pi X\alpha}{N_1} + \frac{2\pi Y\beta}{N_2} + \frac{2\pi Z\gamma}{N_3}\right) \dots (2)$$

Where  $p(X, Y, Z)$  = original input voxel value.

$$\text{cas}(x) = \cos(x) + \sin(x),$$

$P(\alpha, \beta, \gamma)$  is the transformed voxel value.

In 3-D DHT the frequency harmonics increases towards centre within a slice and towards middle slice among different slices.

### B. 3-D DCT and 3-D DFT:

Similarly 3-D DCT and 3-D DFT are implemented. In case of 3-D DCT only real part of 3-D DFT is considered that is cosine part only,imaginary part of discrete Fourier transform can be cancelled by replicating the real part. Whereas frequency harmonics in case of 3-D DCT and 3-D DFT increases from left to right and top to bottom within a slice and increases from first slice to last slice among different slices [4].

### C. 3-D DWT:

Wavelet transform decomposes the signal into many smooth and detailed signals at multiple resolution level [10]. It can be implemented by using 2 channel filter bank [11]. In filter bank analysis filters and synthesis filters are connected by sampling operators. Wavelet transform is achieved by repetitively applying filter bank.

3-D wavelet transformation creates a number of blocks from the image set which have different level of energy. Among them, one block contains most of the energy and rests have other frequency band energy. One level implementation of 3-D wavelet transform is given in fig.4[12].

Daubechies (DB4), bi-orthogonal and Symletwavelet filters are applied on the image data set[13]. For better coding performance filter order is very important. Filter coefficients are determined empirically. Three level of wavelet decomposition is employed.

In the first step by using low pass and high pass filters rows of an  $N \times N$  are filtered. Convolution of filtered image with filters is applied in the second step results in four decomposed sub-volumes and produced sub image of size  $(N/2) \times (N/2)$ . Along the z-direction these four sub bands are filtered and generate eight sub volumes.

Wavelet transformed data consists of one low resolution component and many high frequency components. High frequency components contain less amount of energy as these components have less amplitude. So these components can be eliminated. A threshold value is chosen and amplitude value less than the threshold value is set to zero.

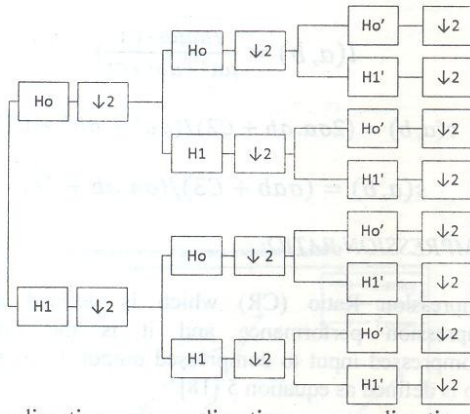


Fig. 4. One level implementation of 3-D wavelet transform[12]

Most of the energy lies in few transformed coefficients and remaining coefficients can be coarsely quantized or even set to zero. Quantization is a non linear process as it is many to few mapping hence it is lossy process. First 2-D quantization matrix is obtained empirically corresponding to first slice of the medical images using different test images so that the PSNR is more than 40 dB with minimum bit rate value. 3-D quantization matrix is obtained by using 2-D matrix as a basis and performing tests on various images keeping the same criteria of PSNR and bit rate value.

In case of 3-D DCT and 3-DFT Zigzag scanning is performed on individual slices sequentially shown in table.I. Whereas in case of 3-D DHT,2-D scanning used for the transformed coefficients is shown below in table II. On 3-D DWT quantized coefficients for all low pass subbands zigzag scanning is performed, for vertical subbands column scanning, for horizontal subbands row scanning and for diagonal subbands zigzag scanning is performed, it is shown in table III. Scanning order is indicated by the number location.

TABLE I.2-D Scanning of DFT and DCT coefficients

1	2	6	7	15	16	28	29
3	5	8	14	17	27	30	43
4	9	13	18	26	31	42	44
10	12	19	25	32	41	45	54
11	20	24	33	40	46	53	55
21	23	34	39	47	52	56	61
22	35	38	48	51	57	60	62
36	37	49	50	58	59	63	64

TABLE II.2-D Scanning of DHT coefficients

1	5	13	25	40	24	12	4
6	14	26	41	52	39	23	11
15	27	42	53	60	51	38	22
28	43	54	61	64	59	50	37
29	44	55	62	63	58	49	36
16	30	45	56	57	48	35	21
7	17	31	46	47	34	20	10
2	8	18	32	33	19	9	3

TABLE III. 2-D Scanning of DWT coefficients

1	2	5	8	17	24	25	32
3	4	6	7	18	23	26	31
9	10	13	14	19	22	27	30
12	11	15	16	20	21	28	29
33	34	35	36	49	50	54	55
40	39	38	37	51	53	56	61
41	42	43	44	52	57	60	62
48	47	46	45	58	59	63	64

Run length coding is applied to the quantized data. RLC reduces the spatial redundancies and achieves compression. In RLC, row by row scanning of image takes place and values of the pixel are replaced by (run lengths, pixel values). After applying RLC, Huffman coding is applied to achieve further compression. In this coding scheme shorter bits are assigned to more probable pixel values and longer bits to less probable pixel values [14].

For decompression purpose decoding process was done by first loading the compressed image and then broken in to 8X8 blocks of pixels. Then each block was dequantized by applying the reverse process of quantization. Then each restored block is filtered through inverse transform and all blocks are combined to get the output image.

### III. EXPERIMENTATION RESULTS AND DISCUSSION

Standard DICOM medical images [15] of six different organs were used for the performance evaluation of the 3D transforms and Wavelets. Different types of images were considered for experimental setup. The experimental data set used can be tabulated as table IV.

TABLE IV. Characteristics of DICOM Sample Images

Type of Image (Modality)	Resolution 3D (X*Y*M) M=No of Slices	Voxel Value Range
Brain MRI	256 X 256 X 16	0 to 255
Cardiac MRI	256 X 256 X 16	0 to 255
Knee MRI	256 X 256 X 16	0 to 255
Chest Angiography	512 X 512 X 16	0 to 255
Liver Angiography	512 X 512 X 16	0 to 255
Abdomen MRI	512 X 512 X 16	0 to 255

To illustrate the performance of each transform and wavelet, the designed code was simulated for different number of frames. For illustration, 16 frames for Brain MRI are shown in Fig. 5.

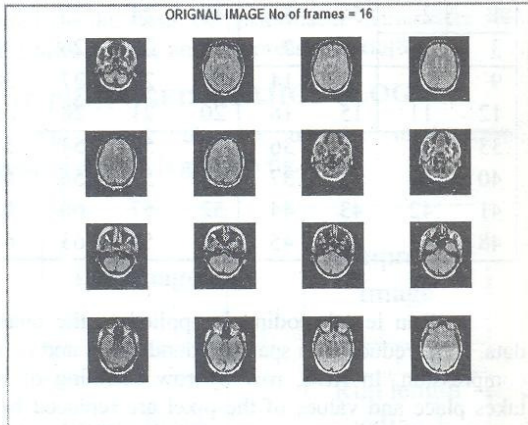


Fig. 5. 16 input frames for Brain MRI

Performance of the implemented compression techniques is evaluated in terms of three performance parameters i.e. PSNR, SSIM and CR. [8,16].

*PSNR:*

PSNR expresses the error between original information and reconstructed image after processing, which is considered as a general parameter for quality assessment and is generally applied in digital image processing. PSNR is calculated using equation 3[17]:

$$PSNR(dB) = \frac{20 \log_{10}(\text{Maximum voxel value})}{\sqrt{\frac{(\sum_i \sum_j \sum_k (f(i,j,k) - F(i,j,k))^2}{N}}} \dots (3)$$

Where voxel value of reconstructed image is  $F(i,j,k)$  at point  $(i, j, k)$ ,  $N$  is the total number of voxel and  $f(i, j, k)$  is the original input value at  $(i, j, k)$

*SSIM:*

SSIM is another important metric of measurement of image quality. SSIM is a method to find the similarity between two images. To improve performance methods like MSE and PSNR, SSIM is designed because these method maybe are inappropriate with the human visual perception. SSIM factor is the average of the combined values of luminance, variance and structure. It measures the change in these three characteristics of two images let suppose "a" and "b". Average pixel intensity is represented as luminance  $l(a,b)$ , variance between the original and compressed image is defined as contrast,  $c(a,b)$  and cross correlation between the original and compressed image by structure  $s(a,b)$ . SSIM between two images can have maximum value of "1" which indicates there is complete similarity between the images. The SSIM is defined in equations 4[17].

$$SSIM(a, b) = l(a, b)c(a, b)s(a, b) \dots (4)$$

Where

$$l(a, b) = \frac{2\mu_a\mu_b + C_1}{\mu_a^2 + \mu_b^2 + C_1}$$

$$c(a, b) = (2\sigma_a \cdot \sigma_b + C_2) / (\sigma_a^2 + \sigma_b^2 + C_2)$$

$$s(a, b) = (\sigma_a \cdot \sigma_b + C_3) / (\sigma_a \cdot \sigma_b + C_3)$$

#### COMPRESSION RATIO:

Compression Ratio (CR) which is defined as the compression performance and it is the ratio of uncompressed input to compressed output. Compression ratio is defined as equation 5 [18].

$$CR = \frac{\text{original bits per voxel}}{\text{Compressed bits per voxel}} \dots (5)$$

Figure 6 shows the original image for Brain MRI for 8 numbers of frames and output for Hartley, Cosine and Fourier transform.

#### A. Brain MRI Results for PSNR vs Bitrate

For M=8, the behavior of different transforms for the Brain MRI images is shown in fig 6.

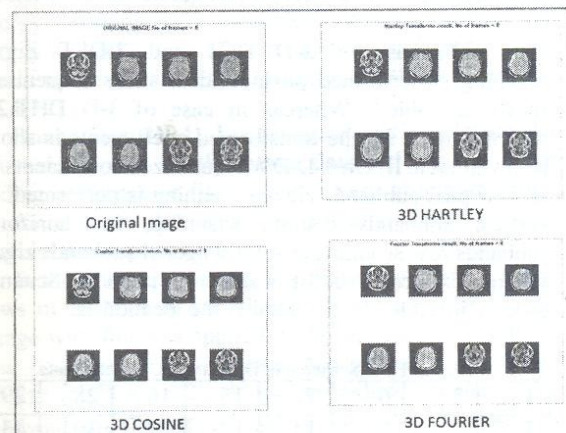


Fig. 6. Original and output images of Brain MRI for Transforms

PSNR graphs for different number of frames i.e 2, 4, 8, 16 for the 3D Hartley, cosine and Fourier transforms are also shown in figure 7(a), figure 7(b), and figure 7(c) and figure 7(d). The Hartley has proven to be more efficient in term of PSNR than other transforms for both low and higher bitrates which is very obvious from the values given in table II and shown in figures 8(a), 8(b) and 8 (c).

Bitrate	2 frames	4 frames	8 frames	16 frames
PSNR	20.00	20.00	20.00	20.00
SSIM	1.00	1.00	1.00	1.00
CRC	100.00	100.00	100.00	100.00
CR	100.00	100.00	100.00	100.00

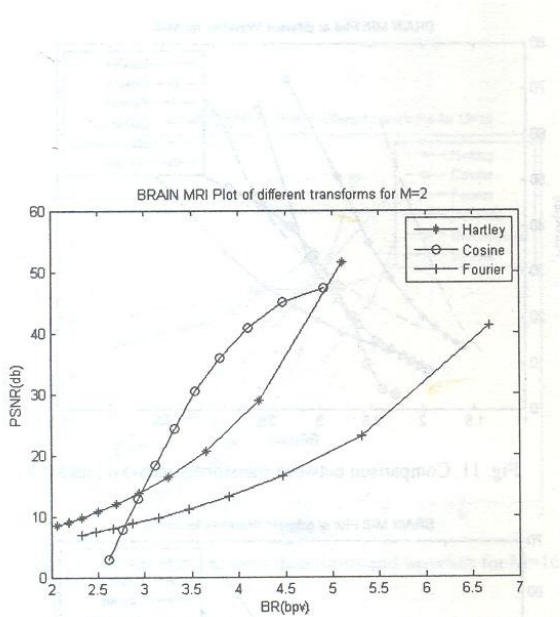


Fig. 7(a). PSNR vsbpv graphs for transforms (M=2)

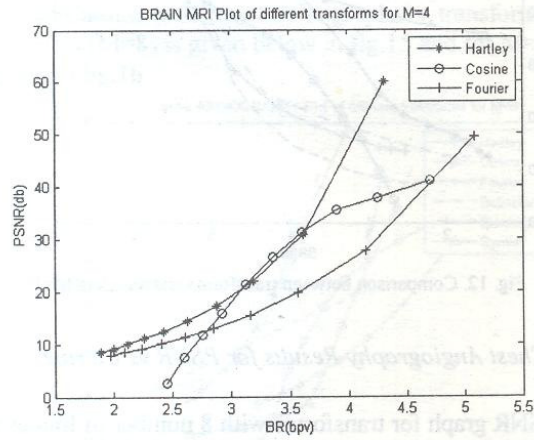


Fig. 7(b). PSNR vsbpv graphs for transforms (M=4)

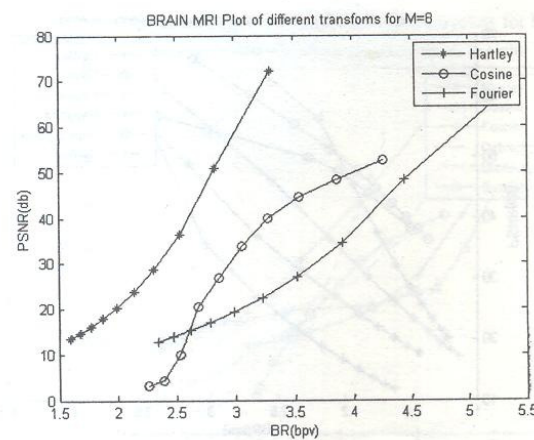


Fig. 7(c). PSNR vsbpv graphs for transforms (M=8)

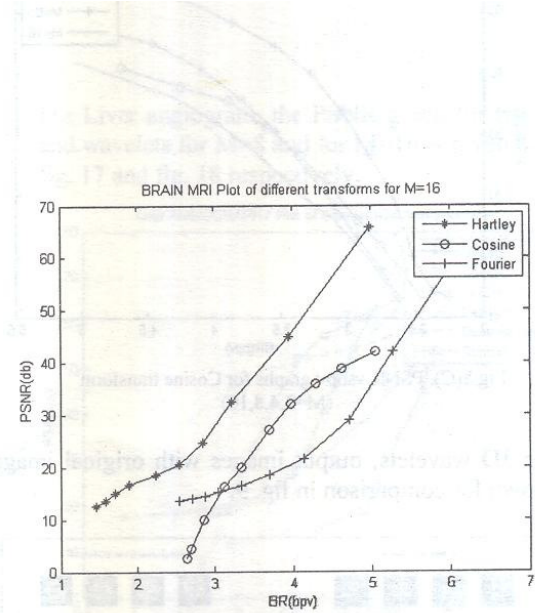


Fig. 7(d). PSNR vsbpv graphs for transforms (M=16)

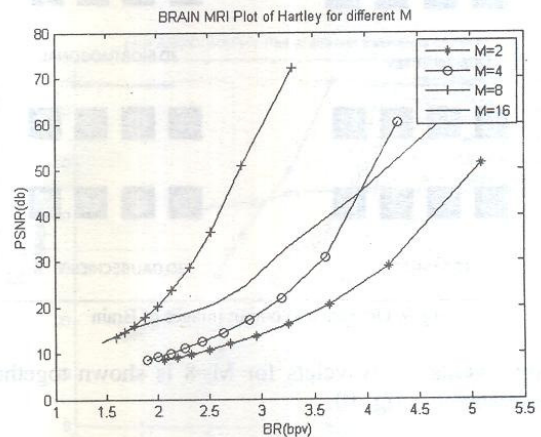


Fig. 8(a). PSNR vsbpv graphs for Hartley transform (M=2,4,8,16)

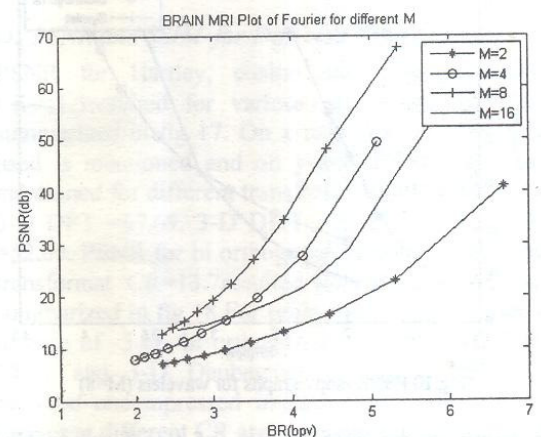


Fig. 8(b). PSNR vsbpv graphs for Fourier transform (M=2,4,8,16)

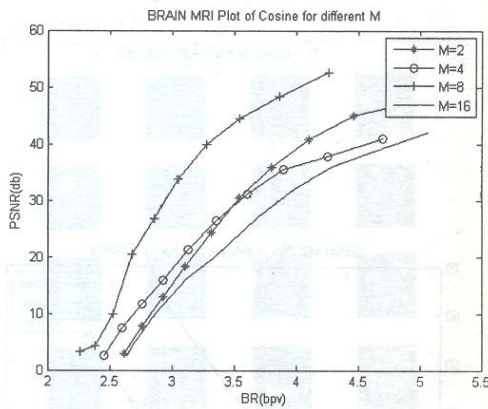


Fig.8(C). PSNR vs bpbv graphs for Cosine transform  
(M=2,4,8,16)

For 3D wavelets, output images with original image are shown for comparison in fig. 9.

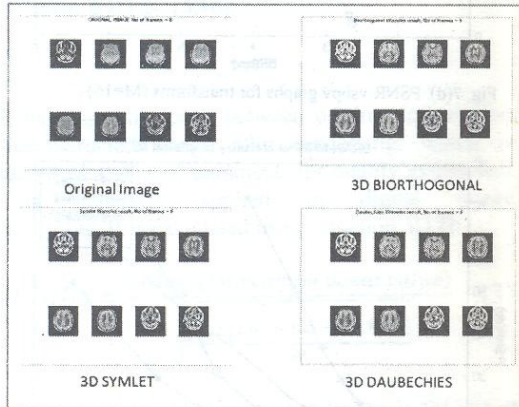


Fig. 9. Original and output images of Brain

Now results for wavelets for M=8 is shown together for assessment in fig. 10.

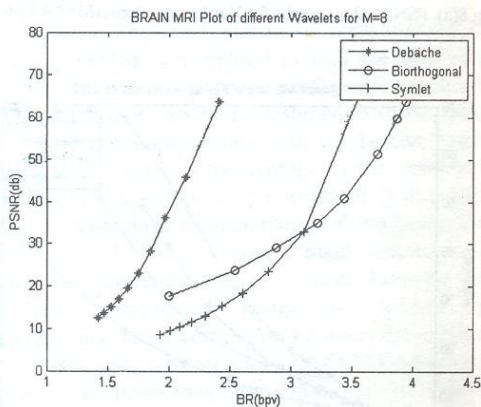


Fig.10 PSNRvsbpv graphs for wavelets (M=8)

To compare the performance of transforms against wavelets, PSNR values for both transforms and wavelets

are plotted together in the fig. 11 and fig. 12 respectively for M=8 and M=16.

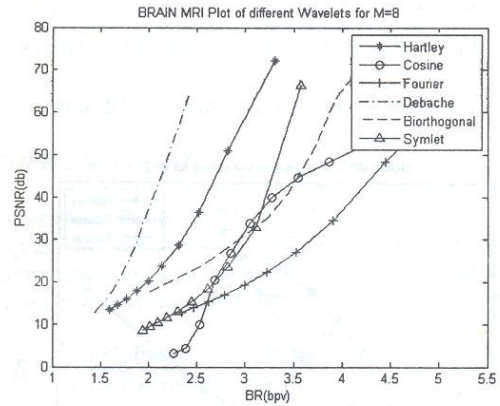


Fig. 11. Comparison between transforms and wavelets(M=8)

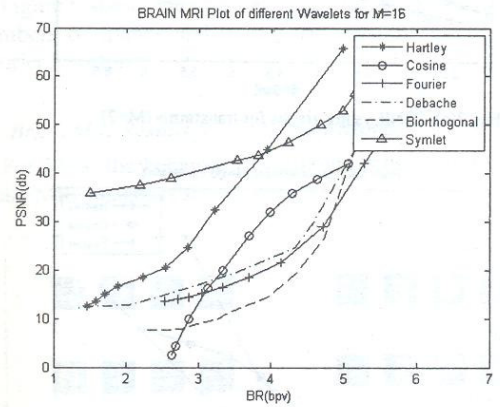


Fig. 12. Comparison between transforms and wavelets(M=16)

## B. Chest Angiography Results for PSNR vs Bit rate

PSNR graph for transforms with 8 number of frames is shown in fig. 13 and PSNR graph with 16 number of frames is shown in fig.14 respectively.

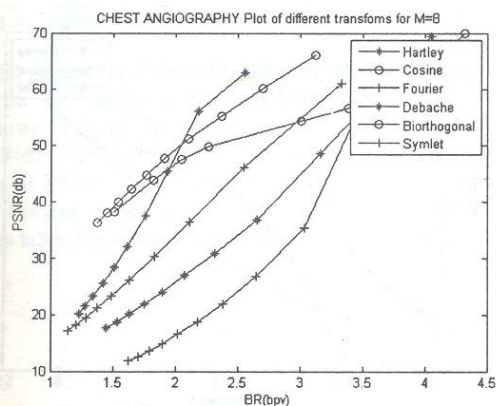


Fig. 13. Comparison between transforms and wavelets for M=8

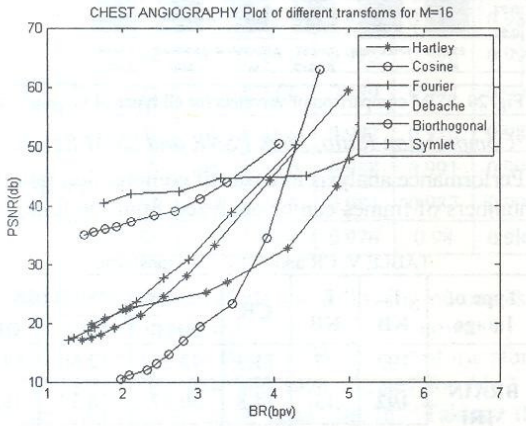


Fig. 14. Comparison between transforms and wavelets for M=16

### C. Cardiac MRI and Liver Angiography Results for PSNR vs Bitrate

For Cardiac MRI, the PSNR graph for transforms and wavelets (M=8) is given below in fig.15 and for M=16 is given in fig.16 .

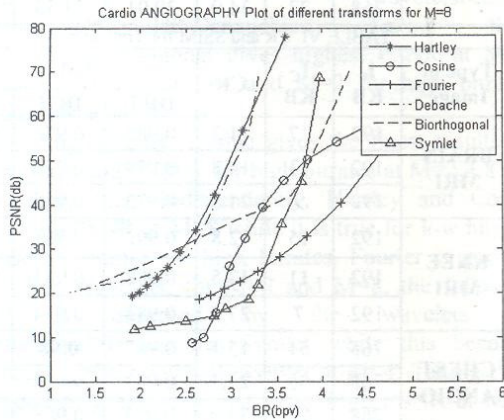


Fig. 15. Comparison between transforms and wavelets for M=8

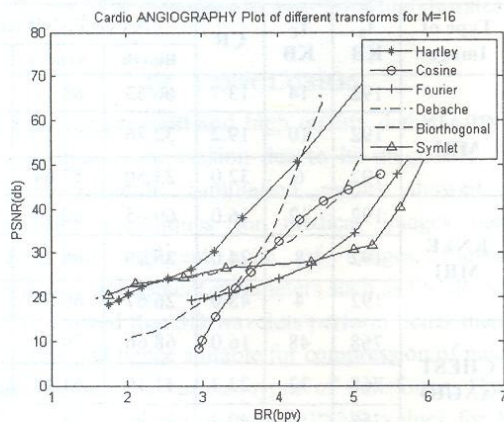


Fig. 16.Comparison between transforms and wavelets for M=16

For Liver angiogram, the PSNR graph for transforms and wavelets for M=8 and for M=16 is given below in fig. 17 and fig. 18 respectively.

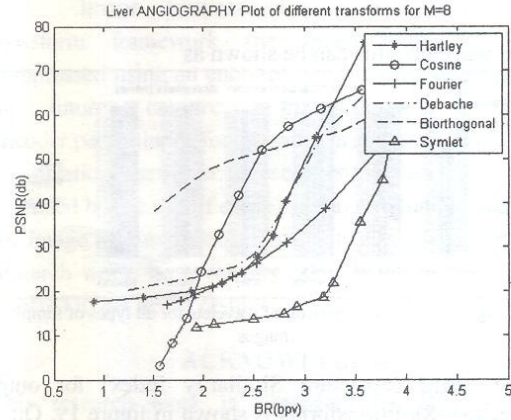


Fig. 17.Comparison between transforms and wavelets for M=8

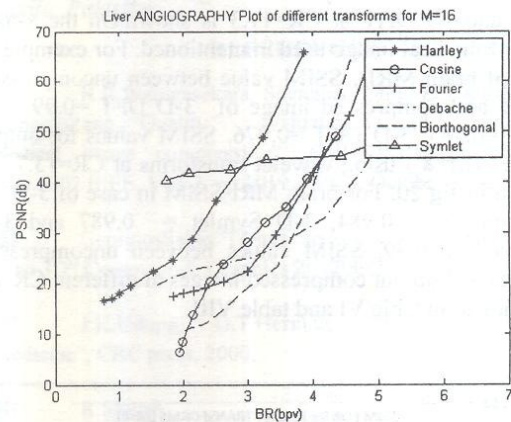


Fig. 18.Comparison between transforms and wavelets for M=16

### D. PSNR and SSIM for Different Type of Images

PSNR for Hartley, cosine and Fourier transformat CR=11.3 resulted for various set of images (M=8) is summarized in fig 17. On x-axis type of medical image used is mentioned and on y-axis PSNR (dB) value is mentioned for different transforms. PSNR value in case of 3-D DFT =67.69, 3-D DHT =72.25 and for 3-D DCT =52.60. PSNR for bi orthogonal, Symlet and Daubechies transformat CR=13.7 resulted for various set of images is summarized in fig 18. For brain MRI image PSNR values in case of 3-D bi orthogonal = 66.43, 3-D Symlet = 65.11 and 3-D Daubachies =71.65 . PSNR values between uncompressed images and output compressed images at different CR are mentioned in table V and table VII.

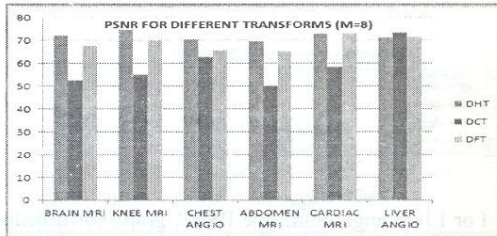


Fig. 17. PSNR comparison of transforms for all types of sample images

For wavelets, this can be shown as

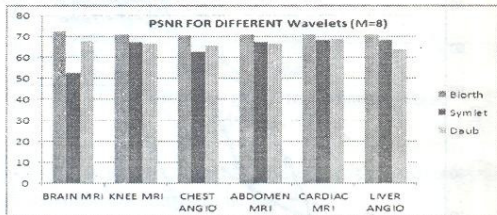


Fig. 18. PSNR comparison of wavelets for all types of sample images

The SSIM (Structure Similarity Index) for output images ( $M=8$ ) of transforms is shown in figure 19. On y-axis SSIM value between the uncompressed original image and output compressed image using 3-D DCT, 3-D DFT and 3-D DHT at CR=11.3 is shown. On the x-axis type of medical image used in mentioned. For example in case of brain MRI, SSIM value between uncompressed image and compressed image of 3-D DFT = 0.99, 3-D DHT = 0.983, 3-D DCT = 0.976. SSIM values for output images ( $M=8$ ) using wavelet transforms at CR=13.7 are shown in fig 20. For brain MRI SSIM in case of 3-D bi orthogonal = 0.984, 3-D Symlet = 0.987 and 3-D Daubachies=0.99. SSIM values between uncompressed images and output compressed images at different CR are mentioned in table VI and table VIII.

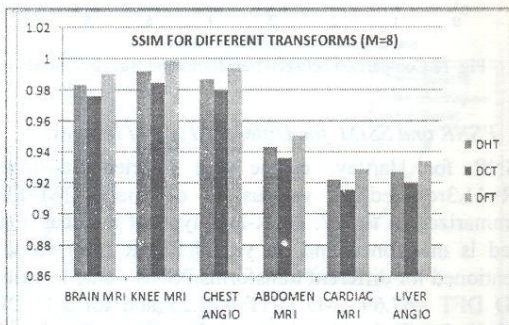


Fig. 19. SSIM comparison of transforms for all types of sample images

For output images from wavelets, SSIM results are

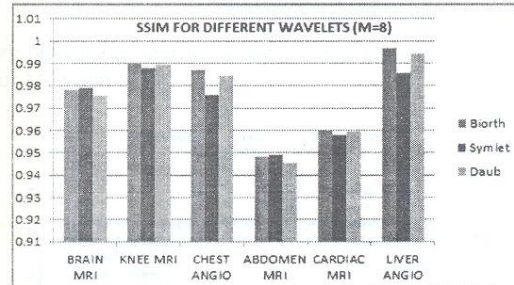


Fig. 20. SSIM comparison of wavelets for all types of sample images

#### E. Compression Ratio, Peak PSNR and SSIM Results

Performance analysis in terms of compression ratio for 8 numbers of frames can be analyzed from the following tables.

TABLE V. CR and PSNR for Transforms

Type of Image	$I_0$ KB	$I_c$ KB	CR	AVG PSNR (dB)		
				DHT	DCT	DFT
BRAIN MRI	192	17	11.3	72.25	52.60	67.69
	192	13	14.8	50.97	48.37	48.22
	192	9	21.3	36.45	44.52	34.59
KNEE MRI	192	15	12.8	69.32	65.96	61.05
	192	11	17.5	48.54	60.05	45.97
	192	7	27.4	36.82	55.14	36.45
CHEST ANGIO	768	51	15.1	70.45	62.85	65.76
	768	36	21.3	54.27	57.71	46.90
	768	22	34.9	39.01	51.33	33.98

TABLE VI. CR and SSIM for Transforms

Type of Image	$I_0$ KB	$I_c$ KB	CR	SSIM		
				DHT	DCT	DFT
BRAIN MRI	192	17	11.3	0.983	0.976	0.990
	192	13	14.8	0.979	0.972	0.986
	192	9	21.3	0.973	0.966	0.980
KNEE MRI	192	15	12.8	0.992	0.985	0.999
	192	11	17.5	0.988	0.981	0.995
	192	7	27.4	0.981	0.974	0.988
CHEST ANGIO	768	51	15.1	0.987	0.98	0.994
	768	36	21.3	0.983	0.976	0.990
	768	22	34.9	0.975	0.968	0.982

TABLE VII. CR and PSNR for Wavelets

Type of Image	$I_0$ KB	$I_c$ KB	CR	AVG PSNR (dB)		
				Biorth	Symlet	DEB
BRAIN MRI	192	14	13.7	66.43	65.11	71.65
	192	10	19.2	32.76	61.30	50.67
	192	6	32.0	23.50	57.64	36.13
KNEE MRI	192	12	16.0	69.65	69.99	68.89
	192	8	24.0	35.29	66.25	56.08
	192	4	48.0	26.67	60.95	45.54
CHEST ANGIO	768	48	16.0	68.66	70.82	74.56
	768	33	23.3	41.10	61.43	55.12
	768	19	40.4	29.96	54.55	41.01

TABLE VIII. CR and SSIM for Wavelets

Type of Image	$I_0$ KB	$I_C$ KB	CR	SSIM		
				Biorth h	Syml et	DEB
BRAIN MRI	192	14	13.7	0.984	0.987	0.990
	192	10	19.2	0.980	0.983	0.986
	192	6	32.0	0.974	0.977	0.980
KNEE MRI	192	12	16.0	0.993	0.996	0.999
	192	8	24.0	0.989	0.993	0.995
	192	4	48.0	0.982	0.986	0.988
CHEST ANGIO	768	48	16.0	0.988	0.991	0.994
	768	33	23.3	0.984	0.987	0.990
	768	19	40.4	0.976	0.98	0.982

Simulation results conclude the following outcomes for the 3D transforms and Wavelets as shown by the simulation results. For Brain MRI, in case of transforms, Cosine is best for low and high bitrates for  $M=2$  and Hartley for  $M=4$ ,  $M=8$  and  $M=16$ . Taking them individually concludes that Cosine and Fourier gives highest PSNR for both low and high bitrates when  $M=8$ , and the same for Hartley for low bitrates. For High bitrates, Hartley performs best at  $M=16$ .

For  $M=2$ , the wavelets follow the high PSNR to low PSNR as biorthogonal>Debauchies>Symlet while this becomes Debauchies>Biorthogonal>Symlet for  $M=4$ . At  $M=8$ , waveletsbehaves Biorthogonal>Symlet>Debauchies. Taking them separately, Biorthogonal gives highest PSNR at  $M=8$ , Symlet at  $M=16$  for low and  $M=2$  for high bitrates, Debauchies at  $M=4$ .

For Angiography, Cosine gives the finest results for low bitrates and Hartley for high bitrates at  $M=2,4,8$  and  $16$ . Taking them independently, Hartley and Cosine gives high PSNR at  $M=8$  while it is true for low bitrates in case of Fourier. At high bitrates, Fourier is good at  $M=4$ . For Wavelets, for  $M=2$  and  $M=8$ , the following order is observed by the wavelets i.e. Biorthogonal>Debauchies>Symlet while this becomes Debauchies>Biorthogonal>Symlet at  $M=4$ . Taking them independently, Biorthogonal gives high PSNR at  $M=8$ , Symlet at  $M=16$  for low and  $M=2$  for high bitrates and Debauchies at  $M=4$  for low and  $M=2$  for high bitrates.

#### IV. CONCLUSION

Low rate compression and high quality demands by the medical image compression due to its diagnostic value are very difficult. Simulation results showed that compression techniques for medical images behave different for different type of images. However, performance assessment parameters such as PSNR, SSIM and CR showed that 3D wavelets perform better than 3D transforms and hence suitable for compression of medical images. Among the various types of transforms, Hartley has been found to result in best PSNR values for MRI

images and results evaluate that Cosine is most suitable candidate for the compression of angiographic images. From different types of wavelets, Debauchies gave highest performance for MRI images than Biorthogonal and Symlet families of wavelets and highest results for PSNR were achieved by Biorthogonal wavelet for Angiography and thus suitable for these types of images.

Image compression is a vast subject. In a transform framework the image can be further compressed using an encoder. So, the next step would be to future compress the image using an encoder, particularly for wavelet transforms with better quantization algorithm. These possibilities can be further extended by the use of complex wavelet functions applied for image decomposition. Huffman was used during this research work, however any other better option may be selected to get better results.

#### ACKNOWLEDGE

This research work is supported by *Directorate of Advance Studies, Research and Technological Development, University of Engineering and Technology Taxila, Pakistan.*

#### REFERENCES

- [1] N.R.Wanigasekara, Shenghao Ding, Zhuangzhi Yan, YongqinZeng, "Quality evaluation for JPEG 2000 based medical image compression", EMBS/BMES Conference, Proc.2002 IEEE, Vol. 2, pp.1019 – 1020, October 2002
- [2] GeorgiosSakas "Trends in medical imaging: from 2D to 3D" Computers& Graphics 26 (2002) 577–587.
- [3] J.K.Udupa, G.T.Herman, "3-D Imaging in Medicine", CRC press, 2000.
- [4] R.Shyam Sunder,C.Eswaran,N.Sriramm, "Performance Evaluation of 3-D Transforms for Medical Image Compression" IEEE International Conference on Electro Information Technology, 2005.
- [5] Stephen.J.Solari, "Digital video and audio compression", McGraw-Hill 1997
- [6] B. Ramakrishnan and N. Sriram, "Internet transmission of DICOM images with effective low bandwidth utilization", Digital Signal Processing, Vol. 16, pp. 825–831, 2006.
- [7] S. Udomhunsakul and K. Hamamoto, "Wavelet filters comparison for ultrasonic image compression," Conf. IEEE TENCON, vol. 1, Nov. 2004, pp. 171-174.

## Quotation

[8] Alain Hore, DjemelZiou. " Image quality metrics: PSNR vs. SSIM " International conference on pattern recognition,2010.

[9] Boussakta.S, Alshibami.O.H, Aziz.M.Y, "Radix- $2 \times 2 \times 2$  algorithm for the 3-D discrete Hartley transform", IEEE Trans. On Signal Processing, Vol. 49, Issue.12, pp3145 –3156, December 2001.

[10] Ruchika, Mooninder Singh, Anant Raj Singh,"Compression of Medical Images Using Wavelet Transforms" , International Journal of Soft Computing and Engineering (IJSCCE) , May 2012.

[11] M. Vetterliand C. Herley, "Wavelets and filter banks: Theory and design" IEEE Trans. Signal Processing, vol. 40, pp. 2207-2232, 1992.

[12] Jun Wang , H. K. Huang,"Medical Image Compression by Using Three-Dimensional Wavelet Transformation"IEEETransactions on medical imaging, vol. 15, no. 4, August 1996.

[13] Bairagi, V.K., "Selection of Wavelets for Medical Image Compression" in IEEE International Conference on Advances in computing, control and telecom technologies, 2009, India, pp 678-680.

[14] Lakhani, G, Lubbock, "Modified JPEG Huffman coding" IEEE Transactions on Image Processing, vol.12, no.2, Feb 2003.

[15] DICOM Test Medical Images available on-line at <ftp://medical.nema.org/medical/dicom/Multiframe/>, accessed June 2012.

[16] V.Bhaskaran, K.Konstantinides, "IMAGE AND VIDEO COMPRESSION STANDARDS Algorithms and Architectures", Kluwer Academic publishers 1996.

[17] Z.Wang, A.C.Bovik, H.R. Sheikh and E.P simoncelli, "Image quality assessment: from error visibility to structural similarity", IEEE transaction on image processing, vol.13.no.4, pp.600-612, 2004.

[18] Tzi-CkerChiueh, Chuan-Kai Yang, Taosong He, H.Pfister, A.Kaufman, "Integrated volume compression and visualization", Visualization '97, Proc. IEEE, pp 329 – 336, October 1997.

➤ Education is helping the child realize his potentialities.

Erich Fromm

➤ Everyman believes that he has a greater possibility.

Ralph Waldo Emerson

➤ Nature is often hidden, sometimes overcome, seldom extinguished.

Francis Bacon

➤ Those who make the worst use of t hei time are the first to complain of its brevity.

Jean de La Bruyere

➤ Revolutions are the locomotives of history.

Nikita S. Khrushchev

➤ Revolution accelerates evolution

Kelly Miller

➤ When reform becomes impossible, revolution becomes imperative.

Kelly Miller

➤ Variety is the mother enjoyment.

Banjhamin Dusraeli

➤ Money is like manure. If you spread it around, it does a lot of good, but if you pile it up in one place, it stinks like hell.

Clint W. Murchison

➤ Science may have found a cure for most evils; but it has found no remedy for the words of them all – the apathy of human beings.

Helen Keller

➤ If you want to life yourself up, lift up someone else.

Booker T. Washington

# A Mathematical Interpretation and Simulations for the 2-D Prime/OOC coding in Long Reach OCDMA Access Network

Abdul Latif<sup>1</sup>, Khuda Bux Amur<sup>2</sup>, Dr. Muhammad Imran Malik<sup>3</sup>

<sup>1</sup>Department of Telecommunication Engineering, Mehran University of Engineering and Technology, Jamshoro.

<sup>2</sup>Department of Mathematics, Quaid-e-Awam University of Engineering, Sciences and Technology, Nawabshah.

<sup>3</sup>Department of Computer Engineering, College of Engineering and Technology, Bahauddin Zakariya University Multan

## Abstract:

In this article, the concept of long reach passive optical network (LR-PON) is discussed in the opening section. A number of access techniques are available but OCDMA technology is proposed for this network. There are many OCDMA coding schemes. Among these, a 2-D Prime/OOC code family is selected for encoding and decoding in the LR-PON on the grounds of its cardinality and good performance. This combination is simulated with two users to prove the feasibility of this scheme. The simulation is done for 100 km without any dispersion compensating arrangements. Results establish that this is a viable setup and can be deployed in the future access networks for cost efficiency and improved performance

**Key Words:** Optical Code Division Multiple Access Network (OCDMA), Long Reach Passive Optical Network (LR-PON), 2-D coding, Optical Orthogonal Codes (OOCs).

## I. INTRODUCTION

Wide scale deployment of fiber to the home (FTTH) at the breakneck speed is the latest phenomenon in the access network and it is developing a new type of passive optical network (PON) that is beyond 20 km, called long-reach (LR) PON [1-2]. This is flourishing due to the large bandwidth demands in access network [3].

There are a number of optical access technologies used in LR-PON from TDM to WDM to hybrid of TDM with other technologies. Among these, OCDMA is considered as a potential candidate for future access network because it has some advantages over other access solutions. It promises to fulfill the rising demands of higher bandwidth and to provide spectrally efficient access networks [4].

By combining OCDMA with long reach access network, a better and cost-effective solution can be developed for last mile section. When both of these are blended, it can produce a viable network solution that will have cost efficiency and enhanced performance.

There are various coding schemes used in OCDMA networks. Since 2-D codes have higher cardinality as compared to 1-D codes, these will be used in the networks having larger number of users. One of these 2-D codes is prime/OOC code. It uses OOC code in the time domain and prime coding is done for wavelength domain.

In this paper, LR-PON along with OCDMA is simulated. Section II gives a brief overview of LR-PON. After that, 2-D OCDMA code Prime/OOC OCDMA is discussed in

section III. Simulation set up is described in section IV. In the last section of this article, results have been analyzed and performance of LR-PON OCDMA network is evaluated.

## II. Long Reach PON (LR-PON)

A general LR-PON architecture consists of an enlarged shared optical fiber linking the central office (CO) and the local user exchange, and optical splitter connecting subscribers to the fiber. The basic idea of LR-PON is to enhance the reach of the network and reduce the switching nodes. This causes a much simpler architecture and produces a hierarchy of telecom networks. A consolidation of access and metro networks [5-6] is achieved in long reach networks as illustrated in fig. 1. LR-PON reduces both network capital expenditure (CapEx) and operating cost (OpEx) [7].

LR-PONs have usually larger split ratios. This results in the reduction of the cost of the equipment because optical components are shared by

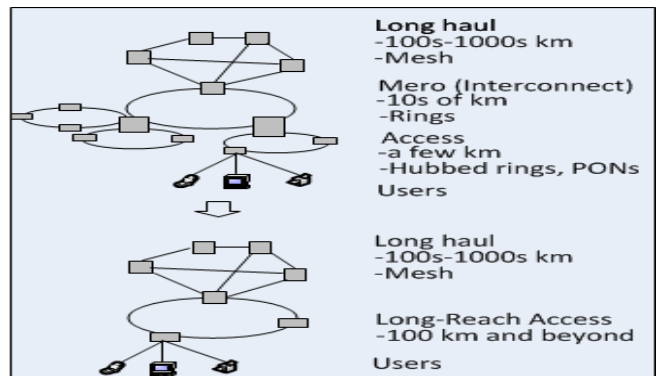


Fig. 1 Simplified Long-Reach PON

each subscriber among customers. Thus the cost of the equipment for each subscriber is reduced.

As per ITU-T standardization, Gigabit PON (GPON) is designed for 60 km distance between Optical Line Terminal (OLT) and farthest Optical Network Unit (ONU) with maximum 1:64 split ratio [8]. To further increase the link reach and coverage of OLT, optical amplifiers are to be used in GPON. Researchers in 1990s were also interested in the idea of extending the reach via intermediate optical amplifiers [9]. However, the maximum reach of Dense-Wavelength-Division-Multiplexed-Passive-Optical-Network (DWDM-PON) is limited due to chromatic dispersion [10-11]. It can be mitigated by using several dispersion compensating measures such as applying optical single

sideband with carrier (OSSB+C) modulation, an optical carrier suppression modulation, Chirped Fiber Bragg Gratings (FBG) [12], and Dispersion Compensation Fiber (DCF) [13]. In recent years Fiber Bragg Gratings (FBGs) [14] and Dispersion Compensation Fiber (DCF) have been identified as effective remedies for minimizing the effects of chromatic dispersion and improving the bit error rates (BER) [15].

In this proposed simulation, no any such dispersion compensation techniques have been applied. Only power boosting component EDFA is used.

Now the 2-D selected for this simulation is briefly described in the following section to give a theoretical understanding.

### III. 2-D Codes in OCDMA

In OCDMA, coding is done on signal by using time domain, frequency domain or combination of both. Besides, space and polarization are also two another dimensions used for OCDMA coding. The later set of dimension is used when 3-D are required to be developed.

In 1-D code, only one aspect is used to encrypt the data. Like time spreading or frequency hopping. Their coding and construction is simple. But 1-D codes have many problems. Their cardinality is low and can sustain only limited number of simultaneous users equivalent to their cardinality. Secondly, if the codes use frequency spreading, then the no. of subscribers is in direct proportion to the length of code or in other words related to the frequency spreading. When the number of subscribers grows, multiuser interference also accumulates. Therefore the bit error rate also increases forcing the system to reduce the number of simultaneously communicating subscribers.

To overcome these shortcomings, many 2-D code families have been developed in the past for time spreading and wavelength hopping dimensions [16], [17]. Other dimensions space and polarization are also used to formulate 2-D and 3-D codes.

A 2-D code is represented by  $(m \times n, w, \lambda_a, \lambda_c)$ .  $m \times n$  is a two dimensional matrix consisting of rows and columns and  $m$  represents the number of wavelengths and  $n$  is number of time chips. It is also equal to the cod length.  $w$  is the weight of the code,  $\lambda_a$  is the autocorrelation and  $\lambda_c$  is the cross-correlation as defined below.

$$\sum_{i=0}^{m-1} \sum_{j=0}^{n-1} x_{i,j} x_{i,j \oplus \tau} = \leq \lambda_a \quad (1)$$

$$\sum_{i=0}^{m-1} \sum_{j=0}^{n-1} x_{i,j} y_{i,j \oplus \tau} = \leq \lambda_c \quad (2)$$

Where  $x \in \{0,1\}$ ,  $\tau$  is the chip duration ( $0 \leq \tau \leq n-1$ ) and  $\oplus$  stands for modulo-n addition.

2-D codes also suffer from the same problem of low cardinality. Therefore there is always a need for new codes and new code families with good properties and having large cardinality in order to cater to a large number of

simultaneous users. The desired codes should have the lowest cross-correlation in order to eliminate MAI.

Now let us discuss a new 2-D code family. This code family, based on wavelength-time was introduced in prime / OOC [18] with particular aim to increase the cardinality of the code. In order to increase the number of codes of a code family, cross-correlation was increased from 1 to 2. For this purpose,  $(n, w, \lambda_a, 2)$  was used. This increased cardinality can be useful in the applications where broadband services are offered with different data rates. Construction details of this code family can be found in the above reference. For time spreading, OOC is applied and in the wavelength domain, prime codes are used.

Cardinality of any OCDMA code can be defined by  $\Phi(n, w, \lambda_a, \lambda_c)$ . For 1-D OOC, cardinality can be optimized as given in equation 3.

$$\Phi_{(n,w,1,2)OOC} = \begin{cases} \frac{n-1}{w}, & \text{for odd } w \\ \frac{n-1}{w-1}, & \text{for even } w \end{cases} \quad (3)$$

For OOC  $(n, w, 2, 1)$ , cardinality can be approximated by the relation (4):

$$\Phi_{(n,w,2,1)OOC} = \begin{cases} \frac{2(n-1)}{w^2-1}, & \text{for odd } w \\ \frac{2(n-1)}{w^2}, & \text{for even } w \end{cases} \quad (4)$$

To complete the comparison, cardinality of OOC  $(n, w, 1, 1)$  is given in eq. 5

$$\Phi_{(n,w,1,1)OOC} = \frac{n-1}{w(w-1)} \quad (5)$$

From these three relations, it can be verified that the cardinality of OOC  $(n, w, 1, 2)$  is the highest.

Now we will discuss prime codes that are widely used in OCDMA.

For prime codes, cardinality is  $p^2$ . The cardinality of the 2-D Prime/OOC code can be defined as  $\phi_{(n, w, 1, 2)} \times p^2$ .

The performance of prime code in terms probability of error at various values of prime number can be determined by the relation (6)

$$P_b = \frac{1}{2} \sum_{i=r}^{N-1} \binom{N-1}{i} \left(\frac{p}{2p^2}\right)^i \left(1 - \frac{p}{2p^2}\right)^{N-1-i} \quad (6)$$

Here  $p$  is the prime number and  $N$  is the number of simultaneous users.  $\Theta$  represents the threshold value. Performance curves for different values of  $p$  are given in figure 2.

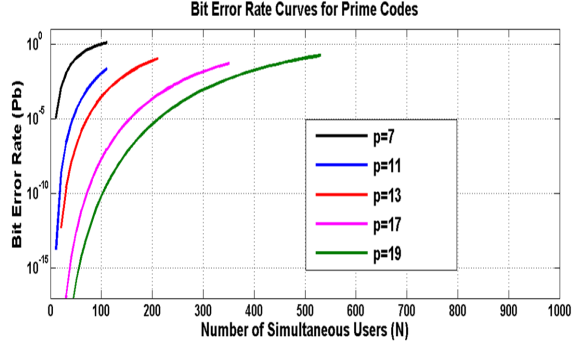


Fig. 2 Performance curves of Prime code

Figure 2 displays the behavior of prime codes. When you increase the prime number, the performance increases and the code can support increased number of simultaneously active users.

If the value of prime number is increased, thereby increasing the length of code, bit error rates falls. It means that with lengthy codes, OCDMA network will provide a better performance. Besides long codes will have lower cross-correlation and therefore are suitable for application where MAI is high and needs to be reduced. However, lengthy codes result in increased complexity for the network.

#### IV. Simulation Setup

In this simulation, 2-D OCDMA encoding and decoding is done. For the encoding in time spreading (13, 4, 1, 2) OOC code is used and for wavelength hopping, prime code having  $p$  equal to 7 is used. It means that no. of wavelengths is seven but code weight is four. Therefore four wavelengths will be used for encoding.

Two codes have been used in this simulation for two users: Code for user one is  $\lambda_1 \lambda_2 0 \lambda_3 0 0 0 0 0 \lambda_4 0 0 0$  and for second user is  $\lambda_3 \lambda_5 0 \lambda_0 0 0 0 0 \lambda_2 0 0 0$ . As it can be seen, there are two common wavelengths between the two codes. Therefore cross-correlation of this coding scheme is 2. The reason for high value of cross-correlation is to enlarge the coding set. Optical orthogonal coding is done in time

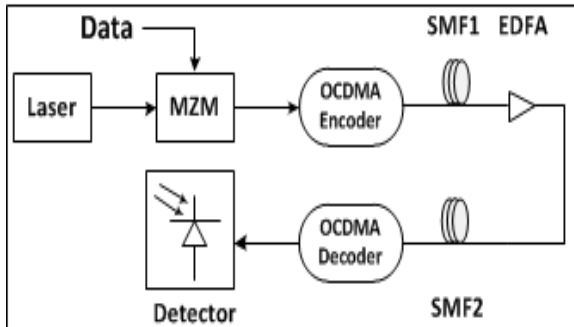


Fig. 3 Simulation setup for OCDMA LR-PON

domain. For the encoding in time domain, optical fiber delay line (FODL) is used. Since FODL can only support high data rates of 1 Gb/s at maximum, therefore data rate is

limited to 1 Gb/s. For wavelength hopping and encoding, FBG filters are utilized with spectral width of 0.8 nm. A series combination of FBG is used to get the desired reflected spectral components constituting the 2-D

Table 1 Parameters used in OCDMA LR-PON simulation

Parameter	Value
SMF Length	100 km
Dispersion of SMF	16.75 ps/nm/km
Attenuation Coefficient of SMF	0.2 dB/km
Non Linear index-coefficient of SMF	$2.6 \times 10^{-20} \text{ m}^2/\text{W}$
Responsivity of Photo detector	1 A/W
Dark current of photo detector	10 nA
Spectral width	0.8 nm
Data Rate	1 Gb/s
Noise Figure (NF) of EDFA	4 dB

code. Since there are 4 marks in the code set, 4 FBGs are added serially in the simulation to encode the signal.

To extend the reach of the OCDMA network from conventional 20 km to very high distance of 100 km, an optical amplifier is used to boost the sagging power in between two sections of the fibers as shown in figure 3.

For the transmitter and receiver side, simple OOK modulation format is employed to keep simulated environment less complicated. The broadband sources for both users have zero powers. At the receiver side, direct detection is done.

Parameters used in this simulation are summarized in table-1.

#### V. Results and Analysis

Results of the simulation are presented here in the form of BER curve against the received power detected by the photodiodes. Both users have same

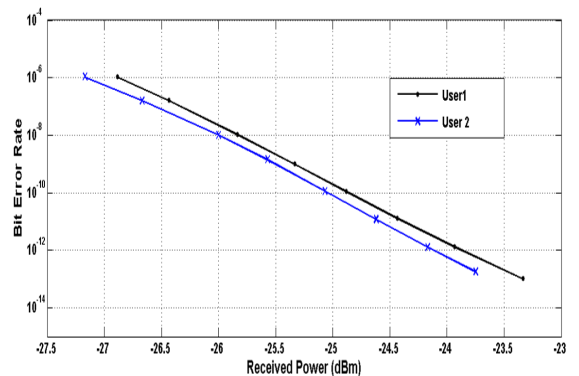


Fig. 4 BER diagram for two users

BER characteristics. At BER  $10^{-9}$ , received optical power is around -25 dBm. Second user

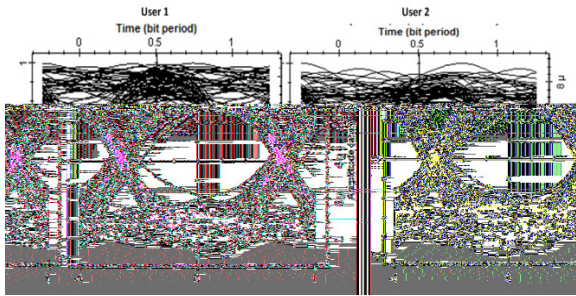


Fig. 5 Eye diagram of two users

exhibits better power sensitivity as compared to first one. In fig. 5 eye diagrams of the two users are given. Eyes are clear and wide open reflecting a fault free transmission. Figure 6 displays the eye diagram of both users when codes mapped on these are reversed. It proves that the codes can interchangeably be applied without degrading the system performance.

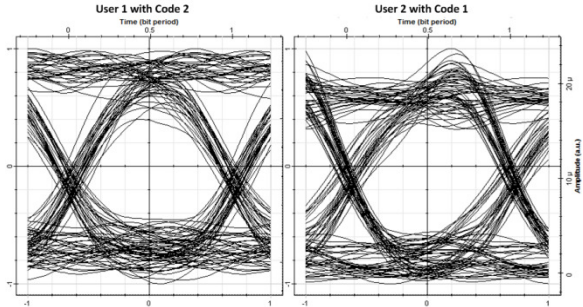


Fig. 6 Eye diagram of users with Codes reversed

These diagrams establish that upto 100 km OCDMA network can be extended without deteriorating transmission.

It is therefore concluded here that an OCDMA network can be applied in the last mile section for longer distances to extend the telecom services in the far flung areas in the cost efficient and spectrally efficient schemes. This simulation affirms the viability of this combination of OCDMA with LR-PON.

## VI. Conclusion

In this paper, the concept of long reach passive optical network (LR-PON) is discussed in the opening section. A number of access techniques is available but OCDMA technology is proposed for this network. There are many OCDMA coding schemes. Among these, a 2-D Prime/OOC code family is selected for encoding and decoding in the LR-PON on the grounds of its cardinality and good performance. This combination was simulated with two users to prove the feasibility of this scheme. The simulation was done for 100 km without any dispersion compensating arrangements. Results assert that this is a viable setup and can be deployed in the future access networks for cost efficiency and improved performance.

## VII. References

- [1] Chow, C., Yeh, C., "Advances in access networks-from long-reach (LR) to short reach (SR), and from TDM/WDM to OFDM", in proceedings of IEEE 21st Annual Optical Communications Conference Wireless (WOCC), pp. 22-24, 2012.
- [2] Wong, E., "Next-generation broadband access networks and technologies", Journal of Lightwave Technology, vol. 30, no. 4, pp. 597–608, 2012.
- [3] Hong, U., Cho, K., Takushima, Y., Chung, Y., "Maximum reach of long-reach RSOA-based WDM PON employing remote EDFA", in proceedings of Optical Fiber Communication Conference, Optical Society of America, 2011.
- [4] Kitayama, K.i., Wang, X., Wada, N., "OCDMA over WDM PON-Solution path to Gigabit-Symmetric FTTH", Journal of Lightwave Technology, vol. 24, no. 4, pp. 1654-1661, 2006.
- [5] Kazovsky, L., Wong, S., Gudla, V., Afshar, P., Yen, S., Yamashita, S., Yan, Y., "Challenges in next-generation optical access networks: addressing reach extension and security weaknesses", Optoelectronics, IET, vol. 5, no. 4, pp. 133–143, 2011.
- [6] Song, H., Kim, B., Mukherjee, B., "Long-reach optical access networks: a survey of research challenges, demonstrations, and research challenges, demonstrations, and bandwidth assignment mechanisms", IEEE Communications Surveys & Tutorials, vol. 12, no. 1, pp. 112–23, 2010.
- [7] Cvijetic, N., Cvijetic, M., Huang, M., Ip, E., Huang, Y., Wang, T., "Terabit optical access networks based on WDM-OFDMA-PON", Journal of Lightwave Technology, vol. 30, no. 4, pp. 493–503, 2012.
- [8] Lin, C., Wong, E., Jiang, W., Shin, P., Chen, J., Chi, S., "28-Gb/s 16-QAM OFDM radio-over-fiber system within 7-GHz license-free band at 60 GHz employing all-optical up-conversion", in proceedings of IEEE conference on Lasers and Electro-Optics, and Conference on Quantum electronics and Laser Science, CLEO/QELS, pp. 1–2, 2009.
- [9] de Paiva, G., Freire, M., Duarte, U., Sassi, A., Bizetti, A., Pozzuto, J., Rosolem, J., Romero, M., "80 km extended gigabit passive optical network", in proceedings of SBMO/IEEE MTT-S International, IEEE Microwave & Optoelectronics Conference (IMOC), pp. 35–39, 2011.
- [10] Davey, R., Grossman, B., Rasztovits-Wiech, M., Payne, D., Nesset, D., Kelly, A., Rafel, A., Appathurai, S., Yang, S., "Long-reach passive optical networks", IEEE Journal of Lightwave Technology, vol. 27, no. 3, pp. 273-291, 2009.
- [11] Lim, C., Nirmalathas, A., Bakaul, M., Lee, K., Novak, D., Waterhouse, R., "Mitigation strategy for

- transmission impairments in millimeter-wave radio-over fiber networks [invited]”, Journal of Optical Networking, vol. 8, no. 2, pp. 201–214, 2009.
- [12] Pan, Z., Song, Y., Yu, C., Wang, Y., Yu, Q., Popelek, J., Li, H., Li, Y., Willner, A.E., “Tunable chromatic dispersion compensation in 40-Gb/s systems using nonlinearly chirped fiber Bragg gratings”, Journal of lightwave technology, vol. 20, no. 12, pp. 2239, 2002.
- [13] Susskind, S., Antonio, E., “Transmission limits analysis of a 40 channels DWDM system at 10 Gb/s without amplification”, Latin America Transactions, IEEE (Revista IEEE America Latina), vol. 9, no. 3, pp. 284–287, 2011.
- [14] Litchinitser, N.M., Eggleton, B.J., Patterson, D.B., “Fiber Bragg gratings for dispersion compensation in transmission: theoretical model and design criteria for nearly ideal pulse recompression”, Journal of Lightwave Technology, vol. 15, no. 8, pp. 1303–1313, 1997.
- [15] Spolitis, S., Ivanovs, G., “Extending the reach of DWDM-PON access network using chromatic dispersion compensation”, in proceedings of IEEE Swedish workshop of Communication Technologies (Swe-CTW), pp. 29–33, 2011.
- [16] Tancevski, L., Andonovic, I., “Hybrid wavelength hopping/time spreading schemes for use in massive optical networks with increased security”, Journal of Lightwave Technology, vol. 14, no. 12, pp. 2636–2647, 1996.
- [17] Yang, G.C., Kwong, W.C., “Performance comparison of multiwavelength CDMA and WDMA+CDMA for fiber-optic networks”, IEEE Transactions on communications, vol. 45, no. 11, pp. 1426–1434, 1997.
- [18] Wang, T.C., Yang, G.C., Chang, C.Y., Kwong, W.C., “A new family of 2-D codes for fiber-optic CDMA systems with and without the chip-synchronous assumption”, Journal of Lightwave Technology, vol. 27, no. 14, pp. 2612–2620, 2009.

\*\*\*\*\*

- Memory is the mother of all wisdom  
Aeschylus
- Memory is a net; one finds it full of fish when he takes it from the brook, but a dozen miles of water have run through it without sticking.  
Oliver Wendell Holmes, Sr.
- Better by far that you should forget and smile than that you should remember and be sad.  
Christina Rossetti
- Obstinacy is the result of the will forcing itself into the place of the intellect.  
Arthur Schopenhauer
- Smallness of mind is the cause of stubbornness, and we do not credit readily what is beyond our view.  
Francois de La Rochefoucauld
- Opinion is ultimately determined by the feelings, and not by the intellect.  
Herbert Spencer
- Prejudice is an opinion without judgment.  
Voltaire
- Give every man thine ear, but few thy voice.  
William Shakespeare
- Prejudice is the chains forged by ignorance to keep men apart.  
Marguerite, Countess of Blesington
- The ignorant are always prejudiced and the prejudiced are always ignorant.  
Charles Victor Roman
- Minds are like, parachutes: they only function when open.  
Thomas R. Dewar
- Prejudice is the child of ignorance.  
William Hazlitt
- Knowing your own darkness is the best method for dealing with the darkness of other people.  
CarlJung
- Work and love – these are the basics. Without them, there is neurosis.  
Theodore Reik

## Quotations

# System Design for Prevention of Electricity Theft

Dr. Khawaja Riffat Hassan\*,  
Saleem Rashid\*, MazharRaza\*\*

National Transmission and Despatch Company Limited (NTDCL),  
Pakistan\*, Pakistan Atomic Energy Commission (PAEC)\*\*

## Abstract

This paper describes the effective system developed for the prevention of Electric Power theft caused by direct rigging. The approach used is to make the electricity useless at distribution transformers and to restore the electricity to useful form by passing it through modified Energy Meter which is exclusively responsible for providing useful electricity to genuine consumers. This can be achieved by stepping up voltage by a factor 'k' (where  $k=2, 3, 4$ ) on low tension side of distribution transformer for short duration in each periodic interval with the help of circuit developed at transformer side. This rough form of voltage if used by direct rigging on electric power conductor, would cause the damage to the appliances. While the genuine consumer gets this supply through modified Energy Meter, which has the ability to detect this rough voltage waveform and convert it back to normal voltage. In this way one of the major causes of electricity theft can be controlled by very economical, simple and technical approach. This circuit has much flexibility in the design so it is less probable to develop a remedy to bypass this design for pilfering.

**Index Terms** — Direct rigging, distribution transformer, energy meter, electric power conductor.

## I. INTRODUCTION

The theft of electric service is an issue that continues to infect utilities across the world. Theft appears in many forms, ranging from sophisticated electronic deception to simply never paying a reasonable bill. As technologies develop to accelerate and improve efficiency of metering and billing, new methods arise to attempt to defraud utilities. Besides the fact that electricity theft is a crime, it also creates an unjustified burden for ratepayers, to whom the cost associated directly with stolen energy and associated revenue protection programs is often distributed. Several reports indicate the prevalence of electricity theft in developing countries range from 20 to 30% losses in the distribution network [1], whereas [2] reported a wider range of 10 - 40% losses. Malaysia In 2004, recorded revenue losses as high as USD229 million and in 2010-11 RM150 to 500 million a year [3-4]. Pakistan has also suffered a mammoth Rs.150 billion loss on account of power theft and line losses in 2012-13[5]. Moreover the developed countries like USA and Canada have also not been spared by this peril and have documented huge revenue loss, that amounts to \$6 billion and \$100 million, respectively, in 2010 [6-7]. Similarly South Africa documented the revenue loss due to theft of electric power ranging from R2.5 to R3.6 billion per year on average, which in the year 2009 even increased to R4.0 billion [8-9].

A lot of methods have been developed so far to prevent the theft of electricity [10-11]. One good approach is given by [12] which involves measuring the total energy units provided by the distribution transformer and then comparing it with the sum of energy units consumed by each meter, the difference tells about the units lost which may be due to theft or line losses. Another method at [13] uses the power line impedance technique, which involves disconnection of subscribers and then a low voltage signal of 2V at 150Hz is transmitted to the network to detect impedance of the network. This impedance is then compared with the installed impedance values and the difference indicates the theft location with respect to the location of genuine consumer. On the other hand [14] proposes application of smart resistance, incorporated in Smart Meter as a mode of detecting illegal electricity usage. But very less work is available for development of a system which is independent to eradicate the theft of electric power mainly by direct rigging.

It is therefore vital to develop a durable system for prevention of electricity theft. Keeping in view the excessive losses and autonomy requirement, this system has been developed which is self-sufficient to protect against theft of electricity caused by direct rigging.

## A.

### Schematic Diagram of System

The schematic diagram for the implementation of this system is shown in figure 1 below:

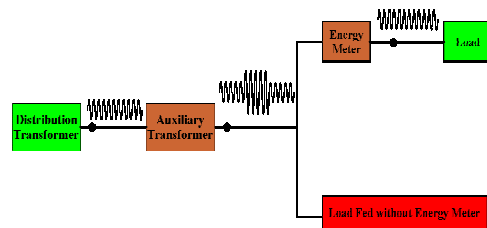


Fig. 1. Schematic Diagram of Design Circuit

It can be seen in the figure 1 that normal voltage supply provided by distribution transformer is disturbed by the auxiliary transformer intermittently, which if fed directly to the equipment, causes damage to its insulation and thus the equipment itself. The over voltage appears for short duration which is customizable e.g. 3 to 5 seconds during 10 minutes interval. Moreover the magnitude of overvoltage is configurable by varying the factor 'k'. This much customization enables to avoid any potential remedy by the thieves of electric power to bypass electricity theft protection system. Therefore the possibility of using this form of power by direct rigging is ruled out. While the same form of power after passing through Energy Meter becomes useful for consumers. As

the circuit designed for detecting the disturbed waveform and converting it back to its normal form is implemented in Energy Meter.

This method of disturbing electricity is very clean, flexible and free from any considerable harmonics thus, has no prominent effect on the reliability of power system. Also the components used for designing the circuits are elementary, ensure longer lifespan, and are economical.

## II. DESIGN OF CIRCUITS

The design mainly consists of two sections

- Transformer Side Circuit
- Energy Meter Side Circuit

### A. Design of Transformer Side Circuit

1) *Simulation Diagram:* Simulation diagram of the circuit which will be explained ahead is shown below:

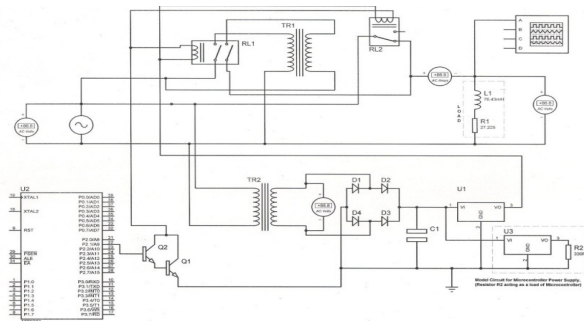


Fig. 2. Circuit Diagram of Distribution Transformer side Section

2) *Working Principle:* The circuit on transformer side produces the over voltage by switching the primary winding of auxiliary transformer in parallel with a phase of distribution transformer and its secondary in series with load as shown in the figure 3.

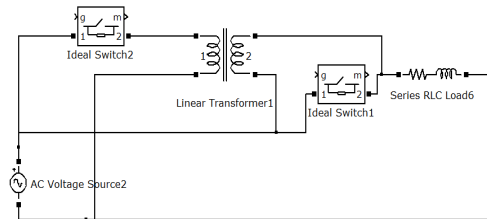


Fig. 3. Simulation for Producing Over Voltages

The circuit on the transformer side consists of only one unit and works for each of the three phases periodically by switching alternatively between the phases and hence minimizing the cost of equipment required.

3) *Explanation:* The block diagram of transformer side circuit as shown below will be explained ahead. The block diagram comprises of following components:

- Control circuitry
- Switching circuit
- Auxiliary transformer
- AC/DC converter
- Voltage regulators

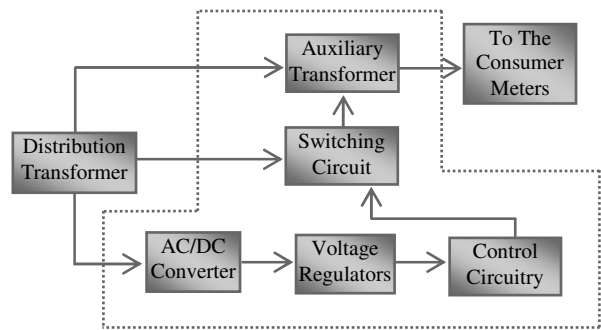


Fig. 4. Block Diagram of Transformer Side Circuit

a) *Control Circuitry:* This circuitry consists of two main components of which one is microcontroller and second one is Darlington pair. Microcontroller is used here to control the duration of high voltage (440 Volts) pulses. Whereas the Darlington pair is used to amplify the output current from microcontroller in order to feed the appropriate current to switching circuit. Both these circuits are explained below.

(b) *Microcontroller:* A microcontroller produces periodic pulses to control the over voltage and normal voltage in different intervals of time. This microcontroller gives signal to Darlington pair which in turn makes the relays RL1 and RL2 active or inactive. The relays are fed through voltage regulator U1 as shown in the figure 2.

As the current during the active condition of relays flows through the Darlington pair, which itself draws very small current i.e.  $\mu\text{A}$  from microcontroller. Therefor micro-controller is protected against the overloading.

(c) *Darlington Pair:* Darlington pair draws very small current from microcontroller to drive relays when high input signal is given by microcontroller.

As the current gain of Darlington pair is given as

$$Gain_{DP} = Gain_{Q1} \times Gain_{Q2} \quad \dots(1)$$

$$G_{DP} = G_{Q1} \times G_{Q2} \quad \dots(2)$$

If Q1 and Q2 are identical, then

$$G_{DP} = G_Q^2 \quad \dots(3)$$

We know that the current gain is

$$G_{DP} = \frac{I_{op}}{I_{in}} \quad \dots(4)$$

$$\frac{I_{op}}{I_{in}} = G_Q^2 \quad \dots(5)$$

$$I_{op} = G_Q^2 \times I_{in} \quad \dots(6)$$

For desired output current, input current can be found. In order to limit the input Current to avoid the loading of microcontroller, transistors of high gain should be selected.

(d) *Switching Circuit*: This circuit consists of relays which control the switching of auxiliary transformer and load. The detail of relays is as under:

(a) *Relays*: When the normal voltage is supplied to load, all the relays are de-energized and the connection of main supply and load is made through normally closed (NC) contact of RL2. When microcontroller gives high signal, both relays are set active. Direct connection of main supply to the load is terminated. At the same time, voltage having value equal to sum of main supply voltage and secondary winding of auxiliary transformer is supplied to the load.

(b) *Auxiliary Transformer*: Auxiliary transformer increases the magnitude of supply voltage by a factor of 'k' depending upon its turn ratio. It is switched in the main circuit intermittently to make the electricity unusable. In the figure 2 this transformer is named as TR1.

(c) *AC/DC converter*: AC/DC converter is used here to supply the 12/5 volts DC. 12 volts are supplied to switching circuit and 5 volts to the control circuitry. It consists of following components:

- Potential Transformer TR2: Potential transformer steps down the supply voltage to value required by sensing circuit.
- Diode Bridge Rectifier: Diode Bridge Rectifier converts ac supply to dc for power supply requirements.
- Capacitor: Capacitor removes ripples from rectified dc supply to make it smooth and supplies power to voltage regulators.
- Voltage Regulator: Voltage regulators provide fix dc voltage to the relays for their proper operation. Two voltage regulators (LM7805, LM7812) are used to provide DC voltage to relays and microcontroller.

## B. Design of Energy Meter Side Circuit

1) *Simulation Diagram*: Actual simulation diagram of meter side circuit for single phase is shown in figure 5.

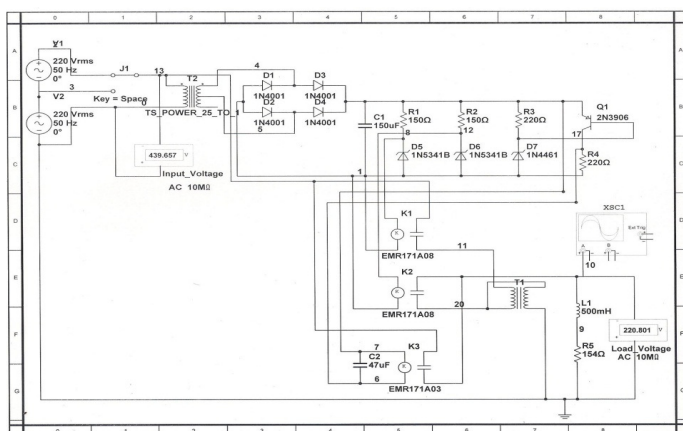


Fig. 5. Simulation Diagram of Meter Side Circuit

2) *Working Principle*: The circuit on energy meter side works by switching in a step down autotransformer during the period when there is overvoltage detected from transformer side to keep the voltage supplied to the load equal to its nominal value.

The purpose of this circuit is to

- Sense the voltage level of main supply.
- Switch the auto transformer in the circuit in order to provide nominal voltage to the load during over voltage period.
- Switch the auto transformer out of circuit at the end of over voltage period.

3) *Explanation*: The block diagram of energy meter side circuit as shown in figure 6 will be explained ahead.

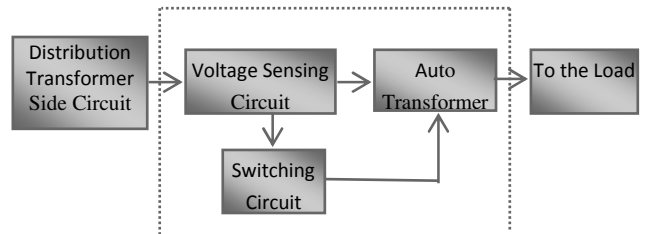


Fig. 6. Block Diagram of Energy Meter Side Circuit

The block diagram comprises of following components:

- Voltage sensing circuit
- Switching circuit
- Autotransformer

a) *Voltage Sensing Circuit*: This circuit is designed such that it gives dc volts analogous to the ac volts at its input side. A transformer, bridge rectifier and capacitor gives DC voltage proportional to AC voltage value of main supply.

This voltage is sensed by Zener regulators. For over voltage, D5 and D6 have greater value of voltage across them, which is enough to turn the relays K1 and K2 ON as shown in the figure 5. These two relays are connected in such a way that the load has nominal value of voltage across it due to step down action of auto transformer.

At the same time, D7 has enough value of voltage to take transistor Q1 in saturation state. As coil of relay K3 is connected to collector and emitter terminals, the only voltage that appears across it will be VEC (sat). This voltage is not enough to operate Relay contact K3. Thus during the over voltage period, K3 is kept de-energized.

In order to ensure proper operation of voltage sensing circuit, first it would be evaluated at over voltage and normal voltage conditions:

(a) *Over Voltage Calculation*: Let L1 be the coil of relay connected in parallel with D1 Zener diode, as shown in the figure 7, and  $V_{PULL}$  be the voltage required to operate relay then,

$$V_{in} = I_{in}R_{in} + V_{out} \quad \dots(7)$$

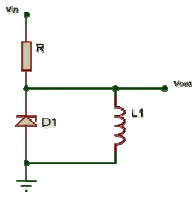


Fig. 7. Zener Voltage Regulator

Current  $I_K$  through relay coil will be

$$I_K = \frac{V_{\text{full}}}{R_K} \quad \dots(8)$$

Here  $R_K$  is the resistance of the coil.

Now the current  $I_{in}$  through the resistor R will be

$$I_{in} = I_{z(\min)} + I_K \quad \dots(9)$$

Here  $I_{z(\min)}$  is current through Zener diode determined practically.

During over voltage condition the voltage across the resistance and zener diode in figure 7 will be

$$V_{in(\min)} = I_{in} R_{in} + V_{out} \quad \dots(10)$$

Substituting value of  $I_{in}$  from equation 9 to equation 10, we have

$$V_{in(\min)} = [(I_{z(\min)} + I_K) R_{in} + V_{out}] \quad \dots(11)$$

If the ripple factor is  $r$ , then the ripple voltage  $V_r$  will be

$$V_r = V_{in(\min)} \times r \quad \dots(12)$$

And the peak value of ripple voltage  $V_{rp}$  will be

$$V_{rp} = \sqrt{2} \times V_{in(\min)} \times r \quad \dots(13)$$

The peak value of input voltage will be

$$V_{in(\overline{\text{over}})} = V_{in(\min)} + V_{rp} \quad \dots(14)$$

The current through  $R_3$ , in figure 5, will be

$$I_{R3} = \frac{8.4 - V_{z(D7)}}{R_3} \quad \dots(15)$$

The current passing through transistor Q1 will be

$$I_{Q1} = \frac{8.4 - V_{EC(SAT)}}{R_4} \quad \dots(16)$$

Here  $V_{in(\min)} = 8.4V$ . During the over voltage, the maximum current  $I_{ov}$  drawn from supply will be

$$I_{ov} = I_{R1} + I_{R2} + I_{R3} + I_{Q1} \quad \dots(17)$$

Here  $I_{in} = I_{R1} = I_{R2}$ .

(a) Normal Voltage Calculation: Let the over voltage  
 $= y \times V_p$

Where y is the factor by which over voltage will be generated and depends upon the ratio of auto transformer.

If auto transformer ratio is 1:1, then  $y=2$ . If it is 1:2, then  $y=3$  and so on.

At normal voltage supply, voltage across capacitor will be reduced by a factor of  $z$  i.e.

$$V_c = \frac{V_{in(\overline{\text{over}})}}{z} \quad \dots(18)$$

If  $z=2$ , then

$$V_{in(\text{normal})} = \frac{V_{in(\overline{\text{over}})}}{2} \quad \dots(19)$$

Let under normal condition of supply voltage, the voltages across Zener diodes and transistor are  $V_{zD5(\text{normal})}$ ,  $V_{zD6(\text{normal})}$ ,  $V_{zD7(\text{normal})}$  and  $V_{EC(\text{normal})}$ .

Now currents through  $R_1$ ,  $R_2$ ,  $R_3$  and  $Q_1$  will be determined by the following equations

$$I_{R1} = \frac{V_{in(\text{normal})} - V_{zD5(\text{normal})}}{R_1} \quad \dots(20)$$

$$I_{R2} = \frac{V_{in(\text{normal})} - V_{zD6(\text{normal})}}{R_2} \quad \dots(21)$$

$$I_{R3} = \frac{V_{in(\text{normal})} - V_{zD7(\text{normal})}}{R_3} \quad \dots(22)$$

$$I_{Q1} = \frac{V_{in(\text{normal})} - V_{EC(\text{normal})}}{R_4} \quad \dots(23)$$

During the normal voltage, the maximum current drawn  $I_{ov}$  will be

$$I_t = I_{R1} + I_{R2} + I_{R3} + I_{Q1} \quad \dots(24)$$

When transition occurs from over voltage to normal voltage, voltage across capacitor varies from  $V_{in(\text{normal})}$  to  $V_{in(\min)}$ . For a continuous supply to load, time of this transition must be short enough to avoid low voltage to load. During this transition, current is provided by the capacitor only (due to reverse biased diodes).

Current supplied to the rest of the circuit by the capacitor also varies as the voltage across capacitor drops from  $V_{in(\text{normal})}$  to  $V_{in(\min)}$ , and the variation of current will be from  $I_{ov}$  to  $I_t$ .

As we know that

$$I = C \frac{dv}{dt} \quad \dots(25)$$

Here for the sake of simplicity, we take the average value of currents  $I_{ov}$  and  $I_t$ .

$$I_{avg} = \frac{I_{ov} + I_t}{2} \quad \dots(26)$$

And

$$C = I_{avg} \frac{dt}{dv} \quad \dots(27)$$

If the transient time is limited to 15 milliseconds, and the change in voltage is 5V, then approximate value of Capacitor will be

$$C = I_{avg} \frac{15m}{5} \quad \dots(28)$$

$$C = 3I_{avg} \times 10^{-3} F \quad \dots(29)$$

This sensing circuit has following components:

- AC/DC Converter
- Zener Diodes

(b) *AC/DC Converter*: AC/DC converter is used in meter side circuit to provide appropriate dc voltage to Zener diode, so that Zener could detect the voltage level. It has following components:

(i) *Potential Transformer*: The potential transformer steps down the nominal ac voltage to permissible lower voltage, so that this lower voltage can further be used for conversion into DC by using bridge rectifier.

Now, as maximum current drawn by the sensing circuit is during the overvoltage condition i.e.  $I_{ov}$

So load Resistance for capacitor will be

$$R_L = \frac{V_{in(\min)}}{I_{ov}} \Omega \quad \dots(30)$$

To find the value of ripple factor  $r$  we use the following relationship for 50 Hz

$$r = \frac{28.7}{R_L C} \quad \dots(31)$$

For excellent power supply ripple voltage must be less than the 5% [15].

So,

$$r = 5\% = 0.05$$

$$V_r = V_{in(over)} \times r \quad \dots(32)$$

And the peak value of ripple voltage

$$V_{rp} = \sqrt{2} \times V_{in(over)} \times r \quad \dots(33)$$

The peak value of input voltage will be

$$V_{ac(peak)} = V_{in(over)} + V_{rp} + 2V_D \quad \dots(34)$$

Here  $V_D$  is voltage drop across single diode.

The RMS value of ac voltage can be found by

$$V_{ac(rms)} = \frac{V_{ac(peak)}}{\sqrt{2}} \quad \dots(35)$$

And the current rating of transformer will be

Hence

$$I_{ac(rms)} = \frac{I_{avg}}{\sqrt{2}} \quad \dots(36)$$

Due to use of bridge diode rectifier, the transformer utilization factor becomes 81% [16].

So VA rating of potential transformer will be

$$\begin{aligned} & \text{VA rating of potential transformer} \\ & = \frac{(I_{ac(rms)} \times V_{ac(rms)})}{0} \cdot 81 \end{aligned} \quad \dots(37)$$

$$\begin{aligned} & \text{VA rating of potential transformer} \\ & = 1.23 (I_{ac(rms)} \times V_{ac(rms)}) \end{aligned} \quad \dots(38)$$

(ii) *Diode Bridge Rectifier*: Diode Bridge Rectifier converts ac voltage to dc for power supply requirements.

(iii) *Capacitor*: Capacitor removes ripples from rectified dc supply to make it smooth. The value of capacitor  $C_1$  as shown in figure 5 should be large enough so that it can provide DC voltage to the Zener regulator. But at the same time it should not be very large to cause unnecessary time delay during the transition of voltages.

(c) *Zener Diodes*: Zener diodes are used here for sensing purpose. They have specific DC voltage across them during the normal and overvoltage AC conditions, which help them to energize or de-energize the coils of relays as required.

b) *Switching Circuit*: it consists of three relays K1, K2 and K3 as shown in figure 5. Its operation depends upon the dc voltage supplied by the sensing circuit to the relay coils.

During normal voltage level of main supply the voltage across D5, D6 and D7 will not be able to operate the relays K1 and K2. So the relays K1 and K2 will remain de-energized and the auto transformer is out of the circuit. At the same time, the transistor Q1 gets out of saturation state and  $V_{EC}$  will become large enough to operate K3. As a result K3 makes the direct connection of the load with the main supply.

The calculation of overvoltage and under voltage for relays K1 and K2 have already been discussed under the section of voltage sensing circuit.

c) *Autotransformer*: The purpose of autotransformer is to step down the voltage during over voltage condition to provide nominal voltage to the load (domestic consumer) uninterruptedly. Auto transformer must have turn ratio of (1/y) in order to provide nominal voltage to the load. As KVA for each Domestic connection is selected as 6 KVA, so required KVA rating of auto transformer will be (6KVA/y) [17].

As the auto transformer will be used for short period of time so the required KVA for auto transformer will be reduced by a factor specified by the manufacturer.

If reduction factor is 'L', then

$$\text{VA rating required for auto transformer} = L(6\text{KVA}/y)$$

Where L is less than or equal to unity.

### III. MODIFICATION IN DESIGN

The voltage sensing circuit on meter side has been designed for voltage variation of 200V to 320V. In Pakistan sometimes voltage drops up to 160V in some areas due to long length of feeders. In order for the circuit to work in this condition, there are two solutions.

4) *Redesign the Circuit*: Redesign the complete circuit for minimum voltage level of 160V. In this method all parameters of the circuit will have to be designed according to the requirement.

5) *Change the Turn Ratio of Potential Transformer*: Increase the sensing voltage by increasing the turn ratio of potential transformer in order to step up the voltage to a value required by the sensing circuit. The ratio of transformer selected for minimum voltage i.e. 200V of design is 50:1

For 200V secondary voltage will be

$$V_{sec} = \frac{200}{50} = 4V$$

For 160V secondary voltage must also be 4V for proper working of sensing circuit. Turn ratio can be calculated as

$$V_{sec} = 4V$$

$$V_{sec} = \frac{160}{n}$$

$$n = \frac{160}{V_{sec}}$$

$$n = \frac{160}{4} = 40 \text{ turns}$$

So the turn ratio should be 40:1 for 160V input.

### IV. FINAL FABRICATED PROTOTYPE CIRCUITS

The proposed system was not only simulated using MATLAB, NI Multisim 10, Keil µVision 3 and Proteus 7.6 Professional, but also fabricated. The final outlook of the circuits is shown in the pictures below:



Fig. 8. Exterior View of Fabricated Circuits

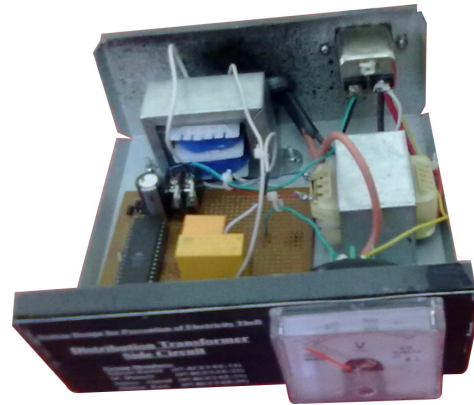


Fig. 9. Interior View of Transformer side Circuit

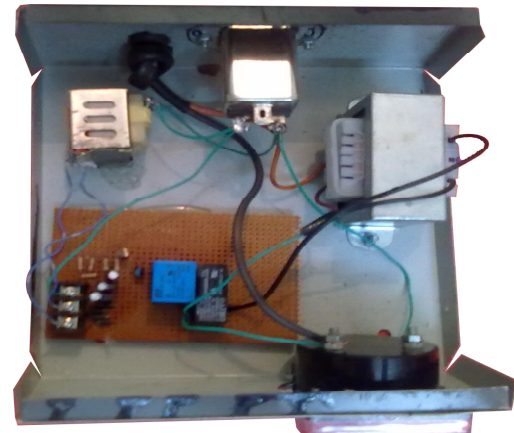


Fig. 10. Interior View of Meter side Circuit

### V. CONCLUSION

#### a. Cost/Benefit Ratio

Cost to benefit ratio is calculated in order to estimate the value of practical implementation of the project. In this report, cost to benefit ratio has been calculated for Peshawar Electric Supply Company (PESCO) in order to indicate the importance of project.

I) PESCO Cost to Benefit Ratio Analysis:

The cost to benefit ratio has been calculated for domestic, commercial and agricultural customers as follows.

From [18] the sum of the above mentioned consumers is given as

$$\text{Total number of consumers} = 2564498$$

a) Energy Meter Circuit Cost

TABLE I. ENERGY METER CIRCUIT COST

Sr. No.	Components	Cost (Rs.)
1.	Potential Transformer (PT)	50
2.	Diodes	8
3.	Capacitor	6
4.	Resistor	2
5.	Zener Diode	12
6.	Transistor	2
7.	Relays	$140 \times 3 = 420$
8.	Autotransformer	375
9.	Circuit Manufacturing Cost	50
<b>Total cost</b>		<b>925</b>

Cost of single meter circuit with 20% margin

$$= 925 + \left( \frac{20}{100} \times 925 \right)$$

$$= \text{Rs. } 1110$$

b) Transformer Circuit Cost

TABLE II. TRANSFORMER CIRCUIT COST

Sr. No.	Components	Cost (Rs.)
1.	Relays	500
2.	Potential Transformer (PT)	150
3.	Diodes	8
4.	Capacitor	10
5.	Transistor	4
6.	Voltage Regulators	10
7.	Microcontroller	70
8.	Auxiliary Transformer	4900
9.	Manufacturing Cost	400
10.	Installation Cost	5000
<b>Total cost</b>		<b>11052</b>

$$\begin{aligned} \text{Total cost of Transformer circuit with} \\ 20\% \text{ safety margin} &= 11052 + ((0.2)(11052)) \\ &= \text{Rs. } 13263 \end{aligned}$$

$$\begin{aligned} \text{Total cost for considered consumers (Meters)} &= \left( \frac{\text{Total number of consumers}}{\text{Number of consumers per transformer}} \right) \left( \frac{\text{Cost of single meter circuit}}{\text{Transformer circuit}} \right) \\ &= (2564498)(1110) \\ &= \text{Rs. } 2846592780 \end{aligned}$$

Similarly, the cost for the total transformer circuits installed can be calculated as

$$\text{Total cost for Transformer circuits} = \left( \frac{\text{Total number of transformer circuits}}{\text{Number of consumers per transformer}} \right) \left( \frac{\text{Cost of single Transformer circuit}}{\text{Transformer circuit}} \right)$$

Where

$$\begin{aligned} \text{Total number of transformer circuits} &= \frac{\text{Total number of consumers}}{\text{Number of consumers per transformer}} \\ &= \frac{2564498}{20} \\ &= 128225 \end{aligned}$$

Hence

$$\begin{aligned} \text{Cost for total Transformer Circuits} \\ &= (128225)(13263) \\ &= \text{Rs. } 1700648175 \end{aligned}$$

Now the Grand total of cost is given as

$$\begin{aligned} &= (\text{Total cost for Transformer circuits}) + (\text{Total cost for considered consumers (meters)}) \\ &\quad \text{Grand Total} = \text{Rs. } 4547240955 \end{aligned}$$

The following data for losses is collected for ten months.

Now the total losses will be calculated as follows,

$$\text{Total units generated in PESCO} = 9483.06 \text{ GWh}$$

$$\text{Units billed} = 6307.31 \text{ GWh}$$

$$\text{Total units lost} = 3175.75 \text{ GWh}$$

$$\text{So, the losses in percentage are} = 33.5\%$$

Now, the actual losses of 3.5% will be subtracted from total losses to get the theft losses. [18]

$$\begin{aligned} \text{Total theft losses} &= (3175.75)(1 - 0.035) \\ &= 3064.6 \text{ GWh} \\ &= 3.0646 \times 10^9 \text{ KWh} \end{aligned}$$

If the cost per unit (KWh) is Rs. 10 then

$$\begin{aligned} \text{Total revenue lost due to theft} &= (3.0646 \times 10^9 \text{ KWh})(10) \\ &= \text{Rs. } 3.0646 \times 10^{10} \end{aligned}$$

This is loss for ten months, and then loss for a year will be calculated as,

$$\begin{aligned} \text{Total revenue lost due to theft per year} &= \left( \frac{3.0646 \times 10^{10}}{10} \right) (12) \\ &= \text{Rs. } 3.67752 \times 10^{10} \end{aligned}$$

Since the component having minimum life used in the circuit is relay that has life span of  $10^6$  number of operations (available in the market). The relay operates ones a ten minutes, it will operate 144 times a day. So the number of relay operations in a year will be,

$$144 \times 30 \times 12 = 51840$$

Hence the total life of a relay and the circuit will be,

$$\frac{10^6}{51840} = 19 \text{ years}$$

Considering safety margin, it is assumed that relay has a life span of 15 years for this project.

Now,

Total revenue loss due to theft for 15 years  
 $= \text{Total revenue lost per year} \times 15$

$$\begin{aligned} &= (3.67752 \times 10^{10})(15) \\ &= \text{Rs. } 5.51628 \times 10^{11} \end{aligned}$$

This revenue loss can be recovered as a benefit if the designed circuit is implemented.

Hence,

$$\text{Cost to benefit ratio} = \left( \frac{4547240955}{5.51628 \times 10^{11}} \right)$$

$$\text{Cost to benefit ratio} = 0.00824$$

6) Calculation for the Recovery Period of Initial Cost:  
 This calculation gives the time period in which this project will recover its initial cost after its implementation. First of all monthly loss will be calculated then total cost will be divided by this monthly loss to get the recovery period in months.

$$\text{Monthly loss} = \frac{\text{Total revenue lost due to theft in 15 years}}{15 \times 12}$$

$$\text{Monthly loss} = \frac{5.51628 \times 10^{11}}{15 \times 12}$$

$$\text{Monthly loss} = \text{Rs. } 3.0646 \times 10^9$$

$$\text{Recovery Period} = \frac{\text{Grand Total of initial cost}}{\text{Monthly loss}}$$

$$\text{Recovery Period} = \frac{4547240955}{3.0646 \times 10^9}$$

$$\text{Recovery Period} = 1.48 \text{ months} \approx 1.5 \text{ months}$$

So the circuit's initial cost will be recovered in almost 45 days.

## B. Results

In this Project the goal was to make the distribution system efficient enough to prevent theft of electricity. Distribution Loss due to theft is one of the major reasons

of developing the gap between supply and demand of electrical energy in Pakistan. This project addresses precisely the same problem with appropriate solution.

Following are the actual results for the waveforms at the output of the energy meter side circuit when the output of distribution transformer side circuit changes from normal to overvoltage and overvoltage to normal. These waveforms are obtained by the simulation performed in NI Multisim 10.0 and Proteus 7.6 Professional.

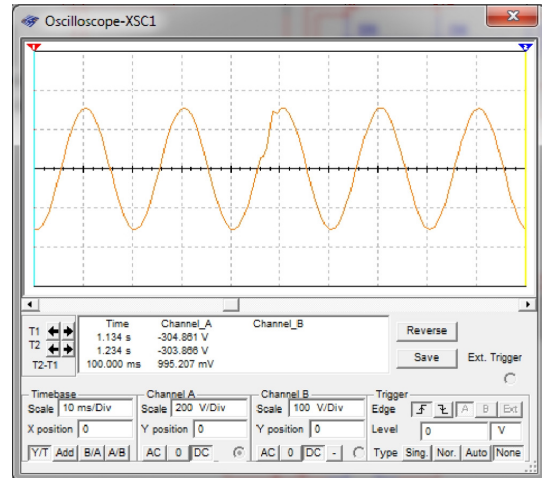


Fig. 11. Output of Energy Meter Side Circuit during Normal Voltage to Overvoltage Transition at the Output of Transformer Side Circuit.

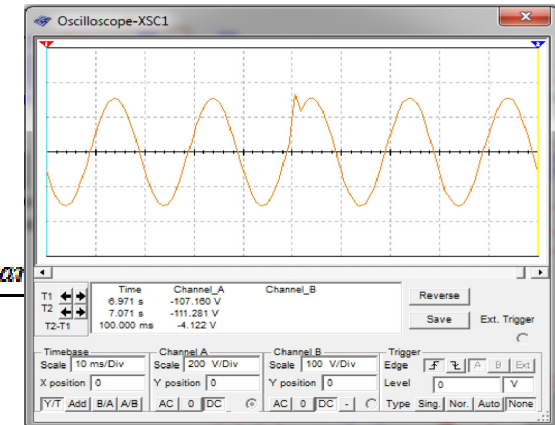


Fig. 12. Output of Energy Meter Side Circuit during Overvoltage Transition at the Output of Distribution Transformer Side Circuit.

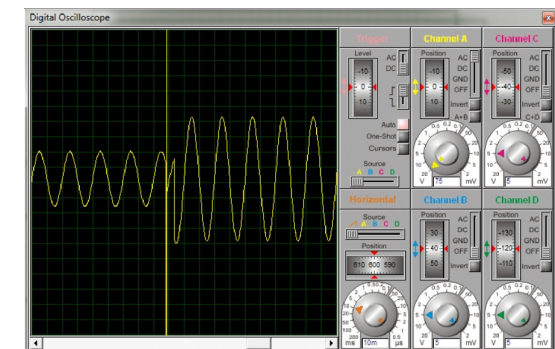


Fig. 13. Normal Voltage to Overvoltage Transition at the Output of Distribution Transformer Side Circuit.

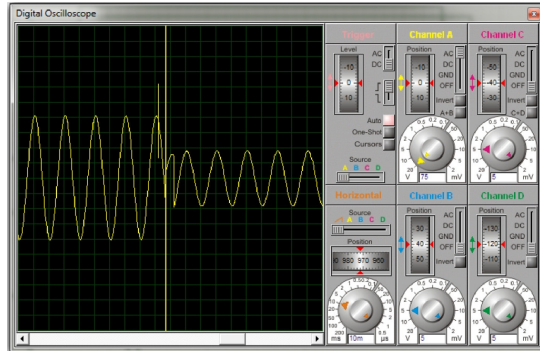


Fig. 14. Overvoltage to Normal Voltage Transition at the Output of Distribution Transformer Side Circuit.

This project has the following major Benefits in it:

- Flexible Solution
  - Cost Effective
  - No Human Intervention
- i) *Flexible Solution*: The solution is not only unique but also flexible in the manner that switching intervals and pulse voltage magnitude are customizable, which provides protection against design theft.
- ii) *Cost Effective*: The design is also cost effective as depicted by the cost to benefit ratio (cost recovers in almost 45 days) results.
- iii) *No Human Intervention*: The circuit makes the distribution system self-efficient to avoid theft of electricity. Hence the human intervention (Line-men, meter reader) is no more encountered.

## VI. REFERENCES

- [1] A.H. Nizar, Z.Y. Dong, "Identification and detection of electricity customer behaviour irregularities", in *Proc. of IEEE Power Systems Conference and Exposition*, Mar. 2009, pp. 1-10.
- [2] L. Wang, V. Devabhaktuni, N. Gudi, "Measures and setbacks for controlling electricity theft", in *Proc. North American Power Symposium*, 2010, pp. 1-8.
- [3] J. Nagi, K.S. Yap, S.K. Tiong, and S.K. Ahmed, "Detection of Abnormalities and Electricity Theft using Genetic Support Vector Machines", in *Proc. of the IEEE Region 10 Conference (TENCON)*, 18-21, Nov. 2008, Hyderabad, India, pp. 1-6.
- [4] Bernama, "SESB reduces its Electricity Theft loss to 13.68 percent", *Bernama*, October 05, 2010. [Online]. Available: <http://www.bernama.com.my>. [Accessed March 23, 2014].
- [5] Khalid Mustafa, "Power theft, line losses cause Rs150b revenue loss", *The News*, pp. 15-17, August 13, 2013. [Online]. Available: <http://thenews.com.pk>. [Accessed March 23, 2014].
- [6] Jeff McShan, "Electricity theft: Dangerous trend that's costing honest Houstonians money", *KHOU*, April 29, 2010. [Online]. Available: <http://www.khou.com>. [Accessed March 23, 2014].
- [7] CBC News, "Electricity theft by B.C. grow-ops costs \$100M a year", *CBC*, October 08, 2010. [Online]. Available: <http://www.cbc.ca>. [Accessed March 23, 2014].
- [8] Fin24, "R4bn lost to electricity theft", *Fin24*, March 23, 2010. [Online]. Available: <http://www.fin24.com>. [Accessed March 23, 2014].
- [9] Environment, "Gauteng has highest rate of electricity theft – Eskom", *Environment*, October 26, 2010. [Online]. Available: <http://www.environment.co.za>. [Accessed March 23, 2014].
- [10] N. Solomon, C. Joseph, "A methodology for the design of an electricity theft monitoring system", *Theoretical and applied information tech. J.*, vol. 26, 2011, pp. 112-117.
- [11] A. Rahul, D. Sapatrashi, and A. Naveen, "Design and development of vigilant energy metering system and its application", *Proc. Student conf. on research and development*. Putrajaya, 2003, pp. 15-18.
- [12] Sriram Rengarajan & Shumuganathan Loganathan. "Power Theft Prevention and Power Quality Improvement using Fuzzy Logic", *International Journal of Electrical and Electronics Engineering*, ISSN: 2231-5284, vol. I, Iss-3, 2012, pp. 106-110.
- [13] Pasdar and Mirzakuchaki S, "2nd Inter. Workshop on Soft Comp. Appl. (Tehran)", 2007, pp. 163-167.
- [14] Kadurek P, Blom J, Cobben J and Kling W, "Innov. Smart Grid Tech. Conf. (Europe)", 2010, pp. 1-6.
- [15] Manzar Saeed, "Electronic devices and circuits", A-One Publishers, vol. I, 1991, pp. 148-50
- [16] Muhammad H. Rashid, "Power Electronics Hand book", *Academic Press*, 2001, pp. 143.
- [17] Stephen J. Chapman, "Electric machinery Fundamentals", 4th Edition, chapter No. 2, pp. 112-113
- [18] "Pakistan Electric Power Company (PEPCO) Consumer Detail and Losses Report", 2010-2011.

\*\*\*\*

# A PWM-Based Technique to Measure Phase Angle Between AC Voltage and Current

Umar T. Shami<sup>1</sup>, and Tabrez A. Shami<sup>2</sup>

<sup>1</sup>University of Engineering and Technology, Lahore, Pakistan

<sup>2</sup>University of Central Punjab, Lahore, Pakistan

## Abstract

This research paper presents a simple and cost-efficient circuit to measure the phase difference between two sinusoidal signals. We have proposed a method that converts the phase-difference into a DC voltage. A mathematical relationship between the phase difference and the DC voltage is also developed. Simulations of the proposed circuit at various phase-angles are presented, the simulation results agrees with the theoretical analysis.

**Index Terms**—Power factor, Phase meter, AC load, PWM technique.

## 1. INTRODUCTION

The phase difference between two sinusoidal signals can be measured by a number of methods [1-9]. M.Salamon and B. Jarc [1] have discussed the simulation results of a signal-phase meter. The authors have claimed a precise signal-phase meter with accuracy more than 0.02%. In addition, the authors have listed a few limitations of the proposed signal-phase meter including prior frequency information, and that the signal factors such; amplitude, phase, frequency, and offset voltage, should have a small rate of change and the change ought be modest. N. M. Vucijak and L. V. Saranovac [2] have proposed two algorithms named as, the simple algorithm (SAL) and a modified SAL (MSAL), for computing phase difference between two sinusoidal signals. B. Djokic and E. So have reported a nonsynchronous multirate digital filtering [3] algorithm that determines that phase angle of deformed periodic signals. The authors proposed a method that functions for a broad bandwidth while maintaining its accuracy. Earlier, S.-J. Lee et al [4] had evaluated a phase detecting technique for PWM rectifiers. While using rectifiers the voltage signal for the supply source is deformed, therefore, the true phase angle between source voltage and current becomes critical. The distortion of the source signal had been approached by applying active filters. M. A. Elela and M. Alturaigi [5] proposed a frequency-insensitive phase meter, where the phase to be measured was converted into a frequency. The frequency was measured to find the phase. R. Micheletti showed the digitizing of two sinusoidal signals and proposed an algorithm that measures the phase angle by least-square method [6].

Two interesting independent research papers, the first by S. M. Mahmud et al [7] and the second produced by K. M. Ibrahim and M. A. H. Abdul-karim [8], demonstrates the application of the dual-slop method for determining the phase angle between two periodic signals however. A classical method to measure the phase difference is to count the number of pulses in the time interval between zero-crossing of the voltage and current signal [9]. We tend to

avoid this method as it has limitations of clock frequency resolution especially at low phase differences. Our proposed circuit is simple and robust and such a circuit, to the best of our knowledge, has not been presented before.

## 2. METHOD:WORKING OF THE PROPOSED CIRCUIT

Fig. 1 presents the proposed circuit where the main power-circuit consist of an ac voltage source,  $v_{in}$ , a current-sensing resistor  $R_{sen}$ , and an ac load comprising of load inductance  $L_L$  and load resistance  $R_L$ . As the main power-circuit input current,  $i_{in}$ , flows through the circuit, it is the phase difference between  $v_{in}$  and  $i_{in}$  that is required to measured. The remaining parts of the proposed circuit will be presented as follows.

### 2.1 Zero-crossing detection

One component that is used in most phase angle detection circuits is the zero-crossing detector (ZCD). The ZCD may be used as a reference or as an agent to detect the instant any electric signal crosses zero volts or amperes. The zero-crossing component in itself is a circuit and many researchers have proposed various circuit schemes and algorithms for detecting the time at which a signal experiences a zero-crossing [10]-[13]. In this research paper a conventional ZCD as presented in [13] is utilized. To detect the zero crossing of the signals,  $v_{in}$  and  $i_{in}$ , two independent ZCDs are connected. Reference to Fig. 1, the first ZCD is labeled as circuit-A and it is connected between  $v_{in}$  and ground. Circuit-A is used to detect the zero-crossing of the  $v_{in}$  signal. The second ZCD is labeled as circuit-B, it is used to detect the zero crossing of the current signal  $i_{in}$ . The voltage appearing across the input terminal of circuit-B is given as,  $v_{Rsen} = i_{in} \times R_{sen}$ . The resistor  $R_{sen}$  should have an insignificant value compared to the ac load. As a consequence, the voltage  $v_{Rsen}$  is trivial and has to be amplified before zero-crossing of the current  $i_{in}$  can be detected.

Fig. 2 depicts the detail schematics of circuit-A and -B, in both figures conventional ZCD as suggested in [13] has been utilized. Fig. 2(a) displays the details of circuit-A which circuit produces a pulse of short duration every time the input signal i.e.,  $v_{in}$  crosses zero-volts. The output signal of circuit-A is labeled as  $v_{v-zcd}$ . Fig. 2(b) shows the internal circuitry of circuit-B that consists of a voltage follower, voltage amplifier, and a ZCD. The input voltage  $v_{Rsen}$  is applied to an operational amplifier based voltage follower. The voltage follower will serve to isolate the low resistance,  $R_{sen}$ , from the non-inverting amplifier and ZCD. Essentially, only the voltage across  $R_{sen}$  is transferred to the amplifier. The non-inverting amplifier is applied to amplify the trivial voltage of  $v_{Rsen}$ . Succeeding the non-inverting amplifier is a

conventional ZCD. The output of the ZCD of circuit-B is labeled as  $v_{i\text{-zcd}}$ .

Fig. 3 displays an exemplary timing waveforms of the proposed circuit, where the traces  $v_{in}$ , and  $i_{in}$  represent the input voltage and current signal, respectively. The time period of input voltage  $v_{in}$  is represented as  $T$ . The phase difference between  $v_{in}$ , and  $i_{in}$  is presented by  $\theta$ . The traces  $v_{v\text{-zcd}}$  and  $v_{i\text{-zcd}}$  are the output signal of circuit-A and -B, respectively. Signals  $v_{v\text{-zcd}}$  and  $v_{i\text{-zcd}}$  both exhibit a pulse of amplitude  $V_{DD}$  volts every-time signals  $v_{in}$ , and  $i_{in}$  experience a zero-crossing, respectively. The remaining

volts. Since  $v_{i\text{-zcd}}$  is connected to the R-pin of the R-S flip flop, the short duration pulse on  $v_{i\text{-zcd}}$  resets the  $v_{pwm}$  to logic zero. From time  $t_1$  to  $T/2$  the  $v_{pwm}$  remains at logic zero. In fig. 3, the trace  $v_{pwm}$  represents the output-Q of the R-S flip flop. It is observed that that on state (logic one) of  $v_{pwm}$  varies directly proportionally with the phase difference between  $v_{in}$  and  $i_{in}$ . From  $t = 0$  to  $t_1$  the amplitude of  $v_{pwm}$  is  $V_p$  volts.

### 2.3 PWM to DC voltage converter

The PWM to DC voltage converter stage shown in Fig. 1

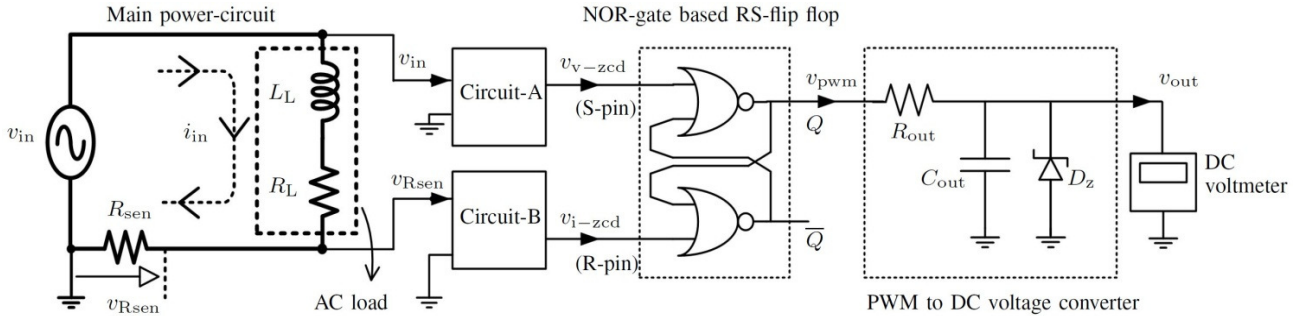


Fig. 5 The proposed circuit to measure phase difference between  $v_{in}$  and  $i_{in}$ .

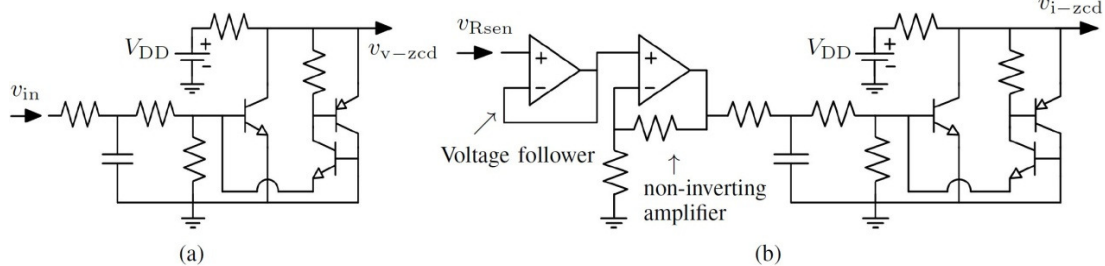


Fig. 6 Conventional ZCD circuitry [13], where (a) shows details of circuit-A, and (b) shows details of circuit-B.

traces  $v_{pwm}$ , and  $v_{out}$  will be discussed in the following sub-sections.

### 2.2 PWM Generation Using R-S Flip Flop

The R-S flip flop circuit shown in Fig. 1, is a sequential circuit created with the help of two NOR gates. Table I exhibits the truth-table for a R-S flip flop [14]. Briefly, the R-S flip flop output-Q with be logic one when input terminals S and R are logic one and zero, respectively. Likewise, the output-Q will be logic zero when S and R are logic zero and one, respectively. As shown in Fig. 1, the signal  $v_{v\text{-zcd}}$  is connected to the set-pin (S-pin) and signal  $v_{i\text{-zcd}}$  is connected to the reset-pin (R-pin), of the R-S flip flop. The output of the R-S flip flop i.e., output-Q is labeled as  $v_{pwm}$ . Reference to fig. 3, at time  $t = 0$ , the input voltage  $v_{in}$  crosses a zero volt, the signal  $v_{v\text{-zcd}}$  produces a voltage pulse of  $V_{DD}$  volts for a short duration (approximately 200 $\mu$ s). Since  $v_{v\text{-zcd}}$  is connected to the S-pin of the R-S flip flop, the short duration pulse on  $v_{v\text{-zcd}}$  sets the  $v_{pwm}$  to logic one. At time  $t_1$ , the signal  $i_{in}$  crosses a zero, the signal  $v_{i\text{-zcd}}$  produces a voltage pulse of  $V_{DD}$

consists of a resistor  $R_{out}$  and capacitor  $C_{out}$  circuit. The Zener diode is used for over-voltage protection. The input of the PWM to DC voltage converter stage is the signal  $v_{pwm}$ , whereas, the output of the PWM to DC voltage converter stage is  $v_{out}$ . As shown in fig. 3, the time period of the signal  $v_{pwm}$  is  $T/2$ . From circuit theory it is known that for a RC circuit, as in the PWM to DC voltage converter stage, if  $5 \times R_{out} \times C_{out} \gg T/2$ , then the voltage  $v_{out}$  appearing across the capacitor  $C_{out}$  can be expressed as,

$$v_{out} = \frac{1}{R_{out} C_{out}} \int_0^{T/2} v_{pwm} dt \quad (4)$$

With reference to fig. 3,  $v_{pwm}$  can be expressed as,

$$v_{pwm} = \begin{cases} V_p & \text{for } 0 < t < t_1 \\ 0 & \text{for } t_1 < t < T/2 \end{cases} \quad (5)$$

Therefore, (1) can be rewritten as,

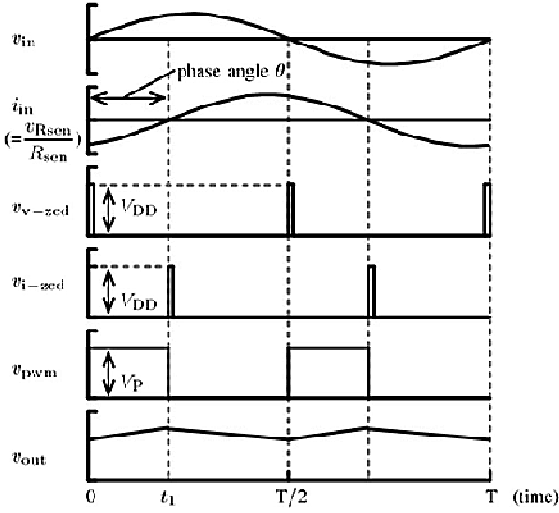


Fig. 7 The proposed circuit exemplary timing waveforms of  $v_{in}$ ,  $i_{in}$ ,  $v_{v-zcd}$ ,  $v_{i-zcd}$ ,  $v_{pwm}$ , and  $v_{out}$ .

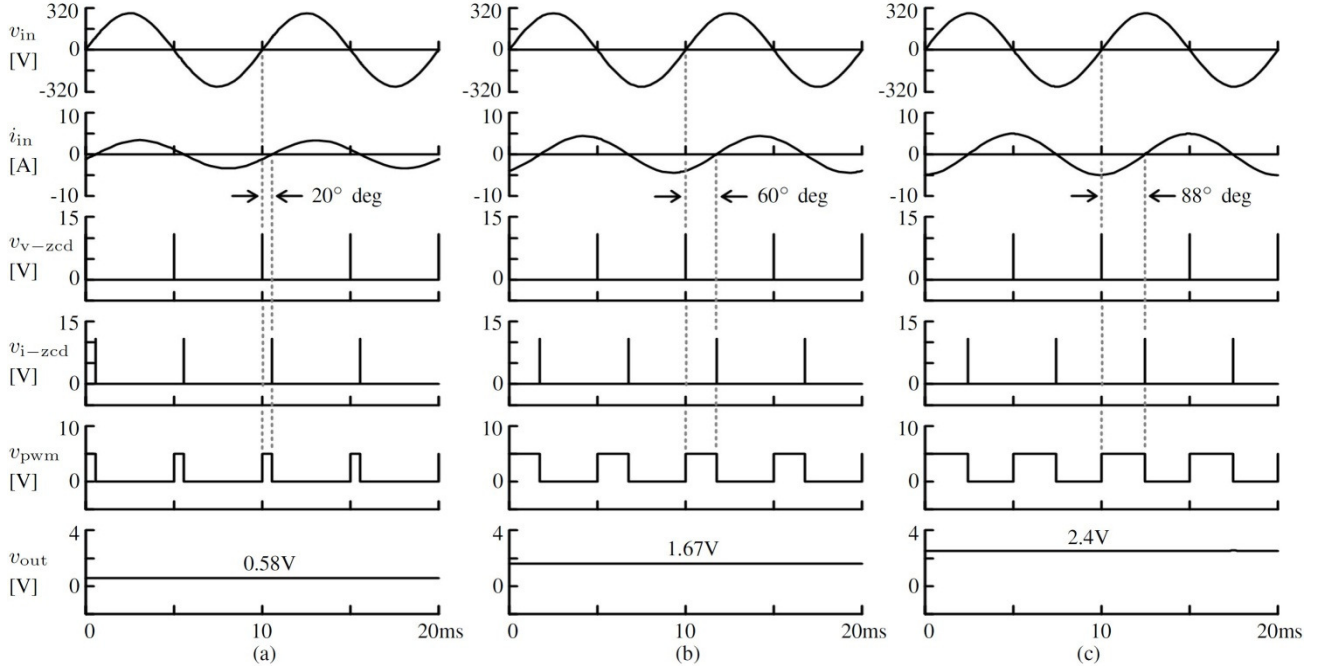


Fig. 8 Waveforms of  $v_{in}$ ,  $i_{in}$ ,  $v_{v-zcd}$ ,  $v_{i-zcd}$ ,  $v_{pwm}$ , and  $v_{out}$ . The value of  $v_{out}$  changes as the phase difference changes. (a) when phase difference is 20°deg (b) when phase difference is 60°deg (c) when phase difference is 88°deg.

Therefore, (5) can be rewritten as,

$$v_{out} = \frac{V_p \theta}{R_{out} C_{out} \omega} \quad (10)$$

That is, the phase angle  $\theta$  can be expressed in terms of  $v_{out}$  can be expressed as, by rearranging (7),

$$\theta = \frac{\omega R_{out} C_{out} v_{out}}{V_p} = \frac{2\pi f R_{out} C_{out} v_{out}}{V_p} \quad (11)$$

$$v_{out} = \frac{1}{R_{out} C_{out}} \left( \int_0^{t_1} V_p dt + \int_{t_1}^{T/2} 0 dt \right) \quad (6)$$

$$= \frac{1}{R_{out} C_{out}} \int_0^{t_1} V_p dt \quad (7)$$

$$= \frac{V_p}{R_{out} C_{out}} (t_1) \quad (8)$$

Since  $\theta = \omega t$ , therefore,

$$t_1 = \frac{\theta}{\omega} \quad (9)$$

**3. SIMULATION RESULTS AND DISCUSSION**

The proposed circuit presented in Fig. 1 was built and simulated in Proteus Virtual System Modeling (VSM)TM software from Labcenter Electronics™. Proteus VSM™ had been selected as it routines mixed mode SPICE circuit simulations. The circuit parameters are set as follows;  $V_{in} = 220V$ (rms), time period of  $V_{in}$  i.e.,  $T = 20ms$ ,  $R_{sen} = 1\Omega$ ,  $L_L = 100mH$ ,  $R_L$  is variable from zero to  $2600\Omega$ . To apply (1), the condition  $5 \times R_{out} \times C_{out} \gg T/2$ , has to be maintained, therefore  $R_{out}$  is selected as  $1k\Omega$  and  $C_{out}$  as  $570\mu F$ . The voltage  $V_p$  is set to  $5V$ . The output voltage  $v_{out}$  is measured using a DC voltage meter. The phase angle is

evaluated by placing the measured value of  $v_{out}$  in (8) and solving for  $\theta$ . Fig. 4 demonstrates the response of the proposed circuit for four different values of phase angle. The phase angle had been varied by varying the value of  $R_L$ . The figures presents the waveforms of  $v_{in}$ ,  $i_{in}$ ,  $v_{v-zcd}$ ,  $v_{i-zcd}$ ,  $v_{pwm}$ , and  $v_{out}$  for different values of  $R_L$ . For Fig. 4(a),  $R_L = 86\Omega$ , as seen  $v_{out} = 0.581V$ , placing this value of  $v_{out}$  in (8) reveals  $\theta = 20^\circ$ deg. At the same time, the phase angle can be calculated from the formula,

$$\theta_{calc} = \tan^{-1}\left(\frac{\omega L_L}{R_L}\right) \quad (12)$$

Placing  $L_L=100mH$  and  $R_L=85\Omega$  in (9) gives  $\theta_{calc} = 20.2^\circ$ deg. Similarly, keeping  $L_L$  same as before and changing  $R_L$  to  $18\Omega$ , the

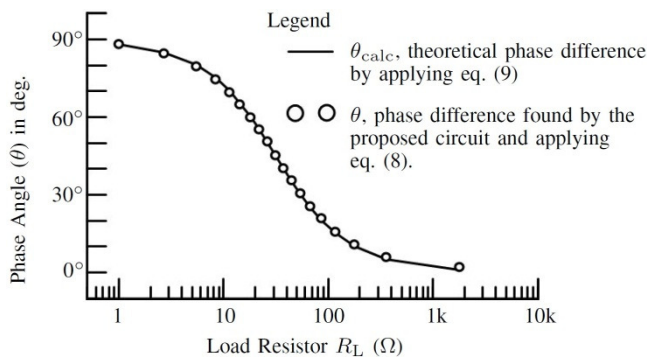


Fig. 9 Comparison of the phase-difference obtained theoretically i.e.,  $\theta_{calc}$  verses  $\theta$ , found with the help proposed circuit.

DC voltage of  $v_{out}=1.67V$  and the evaluated phase angle  $\theta$  from (8)  $59.8^\circ$ deg, whereas the calculated phase angle  $\theta_{calc}=60^\circ$ deg. Again reference to fig. 1, if  $R_L=1\Omega$  then the  $v_{out}=2.46V$  and phase angle  $\theta=88^\circ$ deg, whereas the calculated phase angle  $\theta_{calc}=88.1^\circ$ deg.

To further test the proposed circuit, the load resistor  $R_L$  was varied from zero to  $2600\Omega$  whereas the load inductance was kept constant of  $100mH$  and the capacitor  $C_{out}$  voltage i.e.,  $v_{out}$  was observed. The phase angle  $\theta$  was found from the value of  $v_{out}$  and compared with the phase angle  $\theta_{calc}$ . Fig. 5 present the comparison, the agreement between  $\theta$  and  $\theta_{calc}$  substantiate the proposed circuit. However, the observed difference between  $\theta$  and  $\theta_{calc}$  is due to the insertion of current sensing resistor  $R_{sen}$ . For example when  $R_L$  had been set to zero-ohms the total resistance of the circuit was 1 due the  $R_{sen}$ .

#### 4. CONCLUSION

The objective of this paper was to present a model of a PWM based measurement of phase angle. The proposed circuit was simulated and results were compared with the theoretical results. The simulated results agreed with theoretical results. The proposed model is simple to build and low-cost. Since the proposed circuit produces a DC voltage that is proportional to the phase angle, this DC voltage can be easily converter to a digital signal for applications to microcontrollers, personal computers, or DSP cards.

#### 5. REFERENCES

- [1] M. Salamon, and B. Jarc, "Macromodel of Precise Signal-Phase Meter," Modeling and Simulation in Engineering, vol. 2012, Sep. 2012.
- [2] N. M. Vucjak and L. V. Saranovac, "A Simple Algorithm for the Estimation of Phase Difference Between Two Sinusoidal Voltages," IEEE Trans. Instrum. Meas., vol. 59, no. 12, 2010, pp. 3152-3158.
- [3] B. Djokic and E. So, "Phase measurement of distorted periodic signals based on nonsynchronous digital filtering," IEEE Trans. Instrum. Meas., vol. 50, no. 4, 2001, pp. 864-867.
- [4] S.-J. Lee, J.-K. Kang, and S.-K. Sul, "A new phase detecting method for power conversion systems considering distorted conditions in power system," Conf. Record of the 1999 IEEE Indust. Appl. Conf., Thirty-Fourth IAS Annual Meeting, vol. 4, 1999, pp. 2167-2172.
- [5] M. A. Elela and M. Alturaigi, "Switched capacitor digital phase meter," IEEE Instrum. Meas. Technology Conf., IMTC/95. Proceedings. Integrating Intelligent Instrumentation and Control, April, 1995.
- [6] R. Micheletti, "Phase angle measurement between two sinusoidal signals," IEEE Trans. Instrum. Meas., vol. 40, no. 1, 1991, pp. 4042.
- [7] S. M. Mahmud, A. Rusek, and S. Ganesan, "A microprocessor-based dual slope phase meter," IEEE Trans. Instrum. Meas., vol. 37, no. 3, 1988, pp. 374-378.
- [8] K. M. Ibrahim and M. A. H. Abdul-karim, "A novel digital phase meter," IEEE Trans. Instrum. Meas., vol. IM36, no. 3, 1987, pp. 711-716.
- A. Nemat, "A digital frequency independent phase meter," IEEE Trans. Instrum. Meas., vol. 39, no. 4, 1990, pp. 665-667.
- B. Basu and M. Basu, "Predictive zero-crossing detection algorithm by time localised iterative least-square technique," in Proceedings of the 2011-14<sup>th</sup> European Conference on Power Electronics and Applications (EPE 2011), pp. 1-7, 2011.
- [9] R. W. Wall, "Simple methods for detecting zero crossing," 29th Annual Conf. of the IEEE Indust. Elect. Society IECON, vol. 3, 2003, pp. 2477-2481.
- [10] S. Valivita, "Zero-crossing detection of distorted line voltages using 1-b measurements," IEEE Trans. Ind. Elect., vol. 46, no. 5, 1999, pp. 917-922.
- [11] R. W. Hilsher, "A unique discrete zero-crossing detector," Electronic Design, Vol. 47 Issue 7, April 1999, pp 102. Available: <http://electronicdesign.com/components/unique-discrete-zero-crossing-detector>
- [12] M. M. Mano, "Digital Design," 3rd ed. Prentice Hall, 2001, pp 205-206.

## CALL FOR RESEARCH PAPERS FOR JOURNAL "NEW HORIZONS"

Research Papers from engineers in the Disciplines of Electrical, Electronics (Including Information Technology and Telecommunications), Controls, Mechatronics, Avionics, Computers and Medical Engineering are invited for publication in "New Horizons", **HEC recognized Y-Category**, quarterly research journal of the Institution of Electrical & Electronics Engineers Pakistan. A soft copy of the paper may please be sent to [ieeep1969@gmail.com](mailto:ieeep1969@gmail.com) or [info@ieeep.org.pk](mailto:info@ieeep.org.pk) in the following format:-

- The research paper should be prepared in MS Word Software in Two-Column Format.
- Select A-4 size, 1 inch margins on all four sides, 1.0 line spacing, Times New Roman Font with size 12 and justification on both sides.
- All headings should be in capital bold letters.
- All figures and diagrams must be properly numbered and labeled.
- All diagrams, tables, graphs and photographs must be in Black & White.
- All text within diagrams must be bold enough for readable clarity.
- The papers must not contain more than 6 pages.
- Complete references must be provided at the end of the paper.
- The format to be followed for all references is given below:  
N.E. Nilsson and J. Mercurio "Synchronous generator capability curve testing and evaluation" IEEE. Trans. Power. Del., Vol: 9, no: 1, pp 414. 424, Jan 1994.

### **NOTE:**

You are requested to provide a brief Resume of yourself and of the co-authors (if any) alongwith the paper(s). Also please provide contact numbers and email addresses of all authors.

### **Most Important:**

Kindly note that papers/material as PDF Files will not be accepted.

**Postal Address:** The Institution of Electrical & Electronics Engineers Pakistan  
4 Lawrence Road, Lahore - 54000, Pakistan.  
Ph: (042) 36305289 Fax: (042) 36360287  
Email:[info@ieeep.org.pk](mailto:info@ieeep.org.pk) Website:[www.ieeep.org.pk](http://www.ieeep.org.pk)